



Terms and Conditions of Use of Digitised Theses from Trinity College Library Dublin

Copyright statement

All material supplied by Trinity College Library is protected by copyright (under the Copyright and Related Rights Act, 2000 as amended) and other relevant Intellectual Property Rights. By accessing and using a Digitised Thesis from Trinity College Library you acknowledge that all Intellectual Property Rights in any Works supplied are the sole and exclusive property of the copyright and/or other IPR holder. Specific copyright holders may not be explicitly identified. Use of materials from other sources within a thesis should not be construed as a claim over them.

A non-exclusive, non-transferable licence is hereby granted to those using or reproducing, in whole or in part, the material for valid purposes, providing the copyright owners are acknowledged using the normal conventions. Where specific permission to use material is required, this is identified and such permission must be sought from the copyright holder or agency cited.

Liability statement

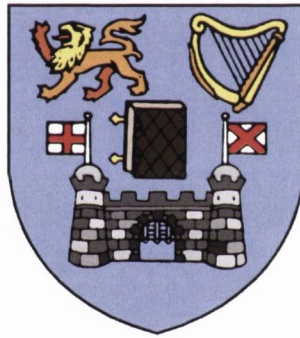
By using a Digitised Thesis, I accept that Trinity College Dublin bears no legal responsibility for the accuracy, legality or comprehensiveness of materials contained within the thesis, and that Trinity College Dublin accepts no liability for indirect, consequential, or incidental, damages or losses arising from use of the thesis for whatever reason. Information located in a thesis may be subject to specific use constraints, details of which may not be explicitly described. It is the responsibility of potential and actual users to be aware of such constraints and to abide by them. By making use of material from a digitised thesis, you accept these copyright and disclaimer provisions. Where it is brought to the attention of Trinity College Library that there may be a breach of copyright or other restraint, it is the policy to withdraw or take down access to a thesis while the issue is being resolved.

Access Agreement

By using a Digitised Thesis from Trinity College Library you are bound by the following Terms & Conditions. Please read them carefully.

I have read and I understand the following statement: All material supplied via a Digitised Thesis from Trinity College Library is protected by copyright and other intellectual property rights, and duplication or sale of all or part of any of a thesis is not permitted, except that material may be duplicated by you for your research use or for educational purposes in electronic or print form providing the copyright owners are acknowledged using the normal conventions. You must obtain permission for any other use. Electronic or print copies may not be offered, whether for sale or otherwise to anyone. This copy has been supplied on the understanding that it is copyright material and that no quotation from the thesis may be published without proper acknowledgement.

The complex dynamics of flowing foam



Michael B. Sexton
School of Physics
Trinity College Dublin

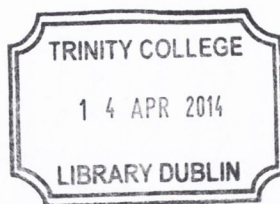
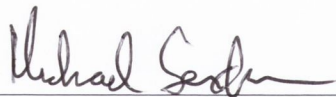
A thesis submitted for the degree of
Doctor of Philosophy
March 4, 2014

Declaration

I declare that this thesis has not been submitted as an exercise for a degree at this or any other university and it is entirely my own work.

I agree to deposit this thesis in the University's open access institutional repository or allow the library to do so on my behalf, subject to Irish Copyright Legislation and Trinity College Library conditions of use and acknowledgement.

Michael Sexton



Thesis 10340

Acknowledgements

I believe that, at its heart, a PhD is a collaborative effort. It is also not a vocation that one simply drops at five o'clock and walks away from. It becomes ingrained in the fabric of your life, and changes how you view the world, and how you think. Consequently, the list of individuals and organisations I'd like to thank is quite long, as the number of people who have been important to me, and by extension to it, is significant.

Firstly, I would like to thank my supervisor, Prof. Stefan Hutzler. Engaging and enthusiastic, insightful and precise, his guidance and support has been invaluable to me. In addition, I would sincerely like to thank Prof. Matthias Möbius, with whom much of the work in this thesis was performed, for always pushing me for “just a few runs” over “one more decade”. I have been most fortunate, too, to benefit from the advice and insight of Prof. Denis Weaire, whose breadth of knowledge and understanding is a source of constant amazement to me. For introducing me to a brave new world of mathematics and economics, I would also like to thank Prof. Peter Richmond, a source of many interesting discussions.

One of the most enjoyable aspects of working towards my PhD has been the great people I have had an opportunity to work alongside, group members past and present: Joe, Steve, Aaron, Ho-Kei, Ruggero, Not-Other-Steve, Cathal, Rob, David and Gav. Special thanks must go to Steve Hardiman, whose patience, helpfulness and unstoppable interest has made working closely with him a highlight of my postgraduate research, and to #CSAS, as a support group for the shared joys (some), pains (most) and procrastination (constant) of research.

I would like to acknowledge the funding and support of the Irish Research Council, formerly IRCSET, and COST action MP0801. This work was made possible by the resources of the Trinity Centre for High Performance Computing, to whom I owe a debt of gratitude.

Not often acknowledged, I feel, but something which has defined my college experience, I would like to thank the Foundation Scholarship fund of Trinity College Dublin. Its mission statement, to encourage and support the best Trinity has to offer, I have seen at work firsthand in the fantastic and diverse people I have met through it, from Commons dinners with the Shadow Council, to the best Pearse Street flatmates ever, through to the Movie Night (movie optional) era. Due in no small part to Schols, Trinity has been more than a university to me: it has been my community, and my home. I sincerely hope that the institution remains strong and vibrant long into the future.

To the fine, (be) upstanding gentlemen of my hockey clubs, Dublin University HC and Rathgar HC, thank you! Thank you for dragging me out in the rain more Saturday mornings than I can count, with 10 men and a panicked last minute search for an umpire and the goalie that ended up somewhere in Ranelagh after last night. Hockey has been a huge outlet for me, and one of my passions, tied very much to the people involved.

To the Lads (you know who you are), and the Girls (you know who you are): a man could not ask for better friends.

To my parents, I dedicate this thesis. You have always been so supportive and encouraging, and have presented me with every possible opportunity and advantage before I could even have known to ask for them. I would not be here today were it not for you.

Finally, I would like to thank Lorraine, for being more to me than is easily described in words. Every day is better with you. I love you.

Summary

We investigate the link between the non-linear macroscopic rheology of wet foams and the microscopic interactions at the bubble-scale, within the general framework of foams as a complex system. This rheology has been found to be well described in simulation by the soft disk model, which represents the bubbles in a two-dimensional foam as a series of overlapping disks, interacting via an elastic repulsion and a viscous dissipation. We simulate linearly sheared systems over a large range of strain rates, showing, for the first time in simulation, the transition between two regimes well-known from experiment: a low-strain regime with swirling, strongly non-affine motion, and a high strain rate regime comprising of laminar flow.

For the low strain rate regime, we find the scaling of shear stress with strain rate to be well described by a Herschel-Bulkley equation with fit parameters dependent on packing fraction, prior to the onset of lane motion. We show, for the first time, that a constitutive law, originally developed for dense granular flows and modified for foams, accurately describes the rheology of foams in two-dimensional simulations, for all strain rates independent of packing fraction. From an empirical fit to this model, we find a scaling exponent for the coefficient of viscous friction comparable to that found in experiment for three-dimensional foams. We also extrapolate a static angle of repose for linearly sheared foam, which we compare with values found from experiment and simulation for foams in different geometries.

We find the change in bubble dynamics at the onset of laminar flow to have a large impact on the foam rheology. For the high strain rate regime, we find the foam flow to no longer be well characterised by the Herschel-Bulkley equation, instead finding the shear stress to scale with the strain rate con-

sistent with viscous drag between bubble layers sliding past one another, in agreement with theoretical models for laminar flow, with no free parameters.

We probe the dynamics at the bubble scale further by considering the non-affine fluctuations of bubble displacements over time. We observe the bubbles to undergo shear-induced diffusion, and extract diffusion constants from the mean square displacements as a function of strain rate. For the low strain rate regime, we find the bubble motion to be well-described by a deformation-relaxation model, relating bubble displacements to the bulk rheology.

We perform the first soft disk model simulations aimed at investigating the rheology of foams in narrow channels. We identify a channel width beyond which the rheology well approximates bulk behaviour. We find the shear and normal stresses to depend on channel width, and propose an explanation for their scaling based on a simple geometric model. We find a constitutive law to continue to describe data well for all packing fractions and strain rates for a fixed channel width, but find that it fails to collapse the data for all channel widths.

Finally, we investigate the statistical properties of fluctuations and fat-tailed distributions of shear stress changes and disk velocities. We show, for the first time, that the shear stress fluctuations in the soft disk model exhibit volatility clustering and long-range memory, familiar in the study of economic markets and complex systems. We apply two modes of analysis, inspired by the similarities between fluctuations in our model and fluctuations in financial returns. The first is a rescaling argument used to compare time-dependent properties as a function of relative position within a trend, first applied in the analysis of S&P 500 stock market data, which we use to quantitatively link topological changes in the foam to fluctuations in the shear stress. The second is a theoretical framework relating generalised diffusion coefficients to the autocorrelation function, using the Fokker-Planck equation, which we apply successfully to asset price fluctuations from the Dow Jones Index, and preliminarily to bubble displacement fluctuations in the soft disk model.

List of publications

1. M.B. Sexton, M.E. Möbius, S Hutzler. “Bubble dynamics and rheology in sheared two-dimensional foams,” *Soft Matter* vol. 7, no. 23, pp. 11252-11258, 2011.
2. M.B. Sexton, S.J. Hardiman, M.E. Möbius, S Hutzler. “Sheared disk packings as a model system for complex dynamics,” (accepted, *Physica A: Statistical Mechanics and its Applications*, 2013).
3. P. Richmond, M.B. Sexton, S.J. Hardiman, S Hutzler. “Modelling of asset price fluctuations,” (submitted).
4. M.B. Sexton, M.E. Möbius, S Hutzler. “The rheology of foams in narrow channels,” (in preparation).

Contents

Contents	ix
List of Tables	xiii
List of Figures	xv
Preface	xix
1 Introduction	1
1.1 A general introduction to foams	1
1.1.1 What is a foam?	2
1.1.2 Wet and dry foams	3
1.1.3 The study of foams	5
1.2 Rheology of Foams	6
1.2.1 Stress and strain in linear shear	7
1.2.2 The Herschel-Bulkley equation	10
1.2.3 Foams in two and three dimensions	12
1.2.4 Experimental geometries	13
1.2.5 Summary	15
1.3 An overview of foam rheology experiments	15
1.3.1 Classification of wet foam rheology by Princen <i>et al.</i>	16
1.3.2 Deformation of droplets by Lacasse <i>et al.</i>	18
1.3.3 Experiments of Denkov <i>et al.</i>	19
1.3.4 Experiments of Dennin <i>et al.</i>	21

1.3.5	Bubble fluctuation experiments of Katgert <i>et al.</i> and Möbius <i>et al.</i>	22
1.3.6	Experiments of Pouliquen <i>et al.</i> and Lespiat <i>et al.</i>	23
1.3.7	The non-local continuum model of Goyon <i>et al.</i>	25
1.4	An overview of foam rheology simulations	27
1.4.1	Durian, Langlois <i>et al.</i> , and the Soft Disk Model	27
1.4.2	Simulations of Ono <i>et al.</i>	31
1.4.3	Jamming in the soft disk model: Olsson and Teitel, and O’Hern <i>et al.</i>	32
1.4.4	The Leiden model, in simulations by Tighe <i>et al.</i>	35
1.5	Foam as a complex system	37
1.6	Conclusions and Outlook	40
2	Macroscopic Rheology in Soft Disk Simulations	41
2.1	The soft disk model	42
2.1.1	Interaction forces	42
2.1.2	System geometry	44
2.1.3	Strain rate, characteristic timescales and Deborah number	46
2.1.4	Stress and the elastic modulus	48
2.2	The Herschel-Bulkley relation for packings of different densities	51
2.3	A constitutive model of foam rheology	56
2.3.1	Origin of the model for granular media	56
2.3.2	Adapting the model for foams	56
2.3.3	The angle of repose	59
2.4	Conclusions and Outlook	60
3	Microscopic Dynamics, Relaxation and Flow	63
3.1	Origin of non-linear rheology	64
3.2	Non-affine motion of disks under shear	65
3.2.1	Mean Square Displacements	66
3.2.2	Shear-induced diffusion in foams	69
3.3	A deformation-relaxation model for foam flow at low strain rate	73

3.3.1	The relaxation time	73
3.3.2	Relating local relaxation to the bulk deformation	76
3.4	Rheology at high strain rate	79
3.4.1	The transition between non-affine motion and laminar flow	79
3.4.2	Viscous scaling via the local drag law	82
3.5	Conclusions and Outlook	83
4	The Effect of Finite System Size	85
4.1	Simulations of narrow channels	87
4.1.1	Finite system size and “bulk” behaviour	88
4.1.2	A model for the dependence of stress on system size	89
4.2	Constitutive model for narrow channels	92
4.2.1	The angle of repose	93
4.2.2	The power law scaling exponent	96
4.3	Conclusions and Outlook	97
5	Stress Fluctuations	99
5.1	Simulation details and definitions	100
5.1.1	Soft disk model parameters	101
5.1.2	Contact changes	101
5.2	Distribution of stress changes	103
5.3	Power-law correlations in the soft disk model	106
5.3.1	Volatility clustering and long-range memory	107
5.3.2	Comparison with a different complex system: the Dow Jones Index	109
5.4	Stress fluctuations and topological changes	111
5.4.1	Preis and Stanley rescaling method	113
5.4.2	Application to stress fluctuations	115
5.5	Conclusions and Outlook	116
6	Generalised Diffusion and the Fokker-Planck Equation	119
6.1	Generalised diffusion model	120
6.1.1	The Fokker-Planck equation	121

6.1.2	The choice of probability distribution function	122
6.2	Application to Dow Jones financial data	123
6.2.1	Inserting D_1 and D_2 for log-returns.	124
6.2.2	Results	125
6.3	Application to soft disk model simulations	132
6.3.1	Choosing an analogy to log returns	133
6.3.2	Mean square displacement distributions	134
6.3.3	Volatility clustering and long-range memory in displace- ments	137
6.4	Conclusions and Outlook	140
7	Outlook	143
7.1	Vorticity in the soft disk model	144
7.2	Towards a soft sphere model	146
7.3	The rheology of foams containing fibres	148
A	Parallel Processing Using CUDA	151
B	Effective Packing Fraction	159
C	Verlet Integration	165
D	Time Resolutions and Limits of the Soft Disk Model	167
D.1	Choosing an appropriate time resolution	167
D.2	Model behaviour at very high strain rate	168
E	Long Memory Processes	171
E.1	Autocorrelation	171
E.2	Volatility clustering and long memory	172
E.3	The Hurst exponent	173
E.3.1	From Nile flooding to fractal geometry	174
E.3.2	Rescaled range (R/S) analysis	174
	References	177

List of Tables

4.1	List of system dimensions	87
6.1	Hurst exponents for stress changes, log-price returns and average transverse displacement	140
D.1	Simulation time resolutions	168

List of Figures

1.1	Dry and wet foams	4
1.2	Simple schematic of linear shear	6
1.3	The stress tensor	8
1.4	Stress versus strain for a viscoelastic medium	11
1.5	Three types of 2D foam	13
1.6	Linear and circular Couette geometries	14
1.7	A T1 transition	17
1.8	Excess energy per facet of a compressed bubble in 2D	18
1.9	Viscous drag between bubble layers	19
1.10	Comparison of viscous drag law theory with experiment, for emulsions and foams.	20
1.11	Distribution of stress drops in a sheared foam	21
1.12	Experimental setup of linear shear	22
1.13	Evolution of mean square bubble displacements in time	24
1.14	Inclined plane linear shear for grains and foams	25
1.15	Velocity profiles predicted by the non-local model, for varying channel width	26
1.16	Stress and strain rate in the simulations of Durian and Langlois <i>et al.</i>	28
1.17	Elastic energy fall distributions	29
1.18	Shear induced diffusion and the Stokes-Einstein relation	31
1.19	Elastic modulus and contact number close to jamming	33
1.20	Inverse viscosity versus shear stress in systems near jamming	34
1.21	The Leiden model	36

2.1	Schematic of bubble-bubble interaction	42
2.2	Bubble trajectories of a linearly sheared foam, for a low strain rate	45
2.3	A typical velocity profile for the steady state flow in a soft disk model simulation	47
2.4	The elastic modulus, G_0	49
2.5	Shear stress versus strain	50
2.6	Shear stress versus Deborah number	51
2.7	Shear and normal stress as a function of packing fraction	53
2.8	Yield stress and Herschel-Bulkley exponent versus packing fraction.	54
2.9	Constitutive model collapse for different packing fractions	57
2.10	Comparison of coefficient of viscous friction in simulation and experiment	58
2.11	The angle of repose	60
3.1	Non-affine velocity vector field for low strain rate	66
3.2	Non-affine displacements at low strain rate	68
3.3	Mean square displacement versus strain interval	70
3.4	Diffusion constants versus Deborah number	72
3.5	Schematic representation of the relaxation time model for Newtonian fluids	74
3.6	Mean square displacements rescaled by diffusion constants	76
3.7	Comparison of deformation-relaxation ansatz with stress versus Deborah number	78
3.8	Laminar flow	80
3.9	Mean square displacements for high strain rate lane motion	81
4.1	Schematic illustration of Lees-Edwards boundary conditions	86
4.2	Visualisations of two narrow-channel simulations	88
4.3	Stress versus Deborah number, for varying channel width	89
4.4	Schematic illustration of simple model with imposed lane motion	90
4.5	Constitutive scaling for narrow channels	92
4.6	Constitutive model collapses for different channel widths	94

4.7	Angle of repose and exponent a versus channel width	95
5.1	The contact matrix	102
5.2	Stress versus strain	104
5.3	Probability distribution of stress changes	105
5.4	Volatility clustering in stress changes	106
5.5	Autocorrelation of stress change	107
5.6	Long memory in the autocorrelation of stress change volatility	108
5.7	Long memory scaling in shear stress and log price returns . . .	110
5.8	Structural changes versus shear stress, in simulation and ex- periment	112
5.9	Rescaling stress microtrends	114
5.10	Contact changes versus rescaled time	116
6.1	Probability density distribution for log price returns for time lags 1, 10, 100 and 400 minutes.	126
6.2	Variation of β versus time lag, for log-price returns.	127
6.3	Generalized diffusion coefficients D_1 and D_2 , computed from minute by minute Dow Jones data over the period 1993-2012.	129
6.4	Fit parameters for D_1 and D_2 versus time.	130
6.5	Autocorrelation of the magnitude (volatility) of minute-by- minute DJIA log returns, 1993-2012	132
6.6	Normalized autocorrelation function for minute-by-minute Dow Jones data over the period 1993-2012.	133
6.7	Probability density distribution for mean square displacements for time lags 2.5, 125, 5000 τ_v	135
6.8	Variation of β as a function of the time lag for mean square displacements.	136
6.9	Volatility clustering in the average transverse displacement versus time	137
6.10	Autocorrelations of the average transverse displacement and magnitude (volatility) of the average transverse displacement .	138
7.1	Vortices in soft disk model flow	145

7.2	Schematic illustration of a hypothetical model for fibres in foam	148
A.1	CUDA simulation	152
B.1	Schematic of overlapping disks of different radii	160
B.2	The variation of average overlap with strain rate and packing fraction	161
B.3	Average contact number versus packing fraction	161
B.4	Effective packing fraction	163
D.1	Voids in the soft disk model	169

Preface

The first time I encountered the study of complex dynamics was as an undergraduate student, during my final year research project in Universität Potsdam. Specifically, I was to examine climate data for the last one hundred or so years, modelling the weather data points as a spatially correlated network and utilising rudimentary complex network theory.

As an undergraduate, the seeming power and scope of this approach instantly seized my attention. Meteorological systems are notoriously complex [1], in the true sense of *complexity* - that is, the property of a system composed of many units where certain global traits encompassing the system as a whole cannot be reduced to a simple averaging of the properties of its constituents [2]. This may be summarised succinctly, by describing the system as more than the sum of its parts.

In such systems, order and disorder are found to coexist, with large scale systemic regularities intertwined with seemingly erratic evolutionary events [2]. Climate systems provide a classical example, where satisfactory weather forecasts are limited to horizons of only a few days. Put simply, although in theory a complex system might be fully determinable, in practice small, unexpected variances can have huge aggregate effects that become difficult or impossible to predict analytically.

It is within precisely these properties that I believe there to exist a natural synergy between foams and complex systems. The flow of foam involves a complex interplay between local interactions, and their propagative effects ultimately determine the bulk properties of the system. An entire research field is devoted to understanding the macroscopic response of foam to applied forces. It is clear that this response is intrinsically connected to the

microscopic dynamics of the system, and yet no widely-accepted theory has emerged on how these two areas are linked. In this thesis we aim to investigate how microscopic dynamics can be linked to macroscopic properties, using novel methods.

Chapter 1

Introduction

In this chapter, we will give a brief, general introduction to foams. We will then introduce foam rheology, and give an overview of experiments and simulations in the field that we feel will be strongly relevant to the discussions put forth in this thesis. Finally, we will introduce complexity and complex dynamics, and discuss foams as a complex system rich in emergent behaviour.

1.1 A general introduction to foams

In physics, the first question asked is often a battle between *how?* and *why?*. As the majority of this thesis shall be dedicated to the former, we shall begin with the latter, and ask: why study foams?

Foams are ubiquitous in everyday life. From washing the dishes, lathering shampoo and spreading shaving foam, through to carbonated drinks and the head on a pint of stout, liquid foams surround us. Their role and use can be as lighthearted as bubblebath, or as sombre as fire extinguishers. Solid foams too, such as polystyrene packaging, foam mattresses and housing insulation to list just a few examples, are encountered on a daily basis.

In industry, the role of foams cannot be overstated. Foams play a crucial role in mineral flotation (the process by which minerals are extracted from ore) and enhanced oil recovery, both multi-billion dollar industries [3]. Mineral flotation, for instance, is estimated to consume approximately 6%

of the world's annual energy resources [4]. As a rough estimation, if the energy industry is worth 10% of a global economy valued at \$70 trillion dollars annually [5], mineral extraction therefore costs approximately \$420 billion dollars a year. This is roughly the same size as the entire semi-conductor industry [6].

In addition to these practical reasons, from a theoretical standpoint foams have long been studied as a model structure for how space is filled. Single layers of bubbles floating on liquid were used by Bragg as a model system for atomic crystal structures in metals [7]. In the natural world, the first uni-cell organisms are thought to have started as bubbles on the ocean floor [8]. Charles Darwin remarked on the foam-like hexagonal structure of bees' honeycomb [9], a comparison which has also been made for geological structures such as the Giant's Causeway in Ireland [10]. Indeed, at the far end of the scale from the atoms whence we started, initial theories on outer space and the "aether" proposed that space was partitioned in Kelvin cells, familiar from foam froth [11,12].

For all its widespread industrial and commercial uses, the material properties of foam are relatively poorly understood. Particularly, in this thesis, we wish to investigate how its flow properties relate to the structure that theorists find so appealing. First, we must define what we mean by a foam.

1.1.1 What is a foam?

Formally, a liquid foam is a two-phase material consisting of a continuous liquid phase enclosing a dispersed gaseous phase [13]. The typical liquid foam studied is *aqueous foam*, consisting of air dissolved in a mixture of water and a surfactant.

Liquid foams are a specific example of a broader classification of materials called *colloids*. Colloids in general are two-phase materials, with one phase dispersed in another [14]. Examples can include solid foams (gas in solid), emulsions (liquid in liquid) and suspensions (solid in liquid). Colloids can share similar properties when it comes to flow behaviour. Many of these properties ultimately arise from interactions at the microscopic level between

elements of the dispersed phase. Foams may also be considered as frictionless granular media, and their structure and packing can resemble that of other granular media [15].

1.1.2 Wet and dry foams

Foams are typically described in terms of their *liquid fraction*, ϕ_l , defined as the ratio of the volume of the liquid phase to the volume of the foam. Depending on ϕ_l , foams may be referred to as either *wet* or *dry*. Examples of dry and wet foams are shown in Figure 1.1.

Dry foams have a liquid fraction, in general, of $\phi_l \lesssim 10\%$. In dry foams, bubbles are separated by thin films of liquid. These films meet along curved lines known as *Plateau borders*, named after the blind Belgian physicist Joseph Plateau. Plateau's life work, "*Statique Expérimentale et Théorique des Liquides soumis aux seules Forces Moléculaires*", published in 1873, lays out a set of rules developed from experimental observation, which govern the structure of dry foams in equilibrium [16]. These are, for three dimensions:

1. Films can intersect only three at a time, and must meet at an angle of $2\pi/3$ radians. These intersections are known as Plateau borders.
2. Vertices in the foam consist of the intersection of exactly four Plateau borders, forming a symmetrical tetrahedron whose angles all equal $\phi = \cos^{-1}(-1/3)$.
3. The films (and Plateau borders) obey the Young-Laplace law, which relates the pressure difference between two bubbles to the surface tension in the film between them and the radius of curvature of the film [13]. It may be summarised, as observed by Plateau, that at any point on a film in equilibrium, the curvature of the film is constant.

The final point has a corollary that a free bubble will always be spherical. Plateau's rules were developed from experimental observation, and later explained by asserting that a foam will always adopt a structure to minimise its surface energy $E = \Gamma A$, where A is the area of its films and Γ is

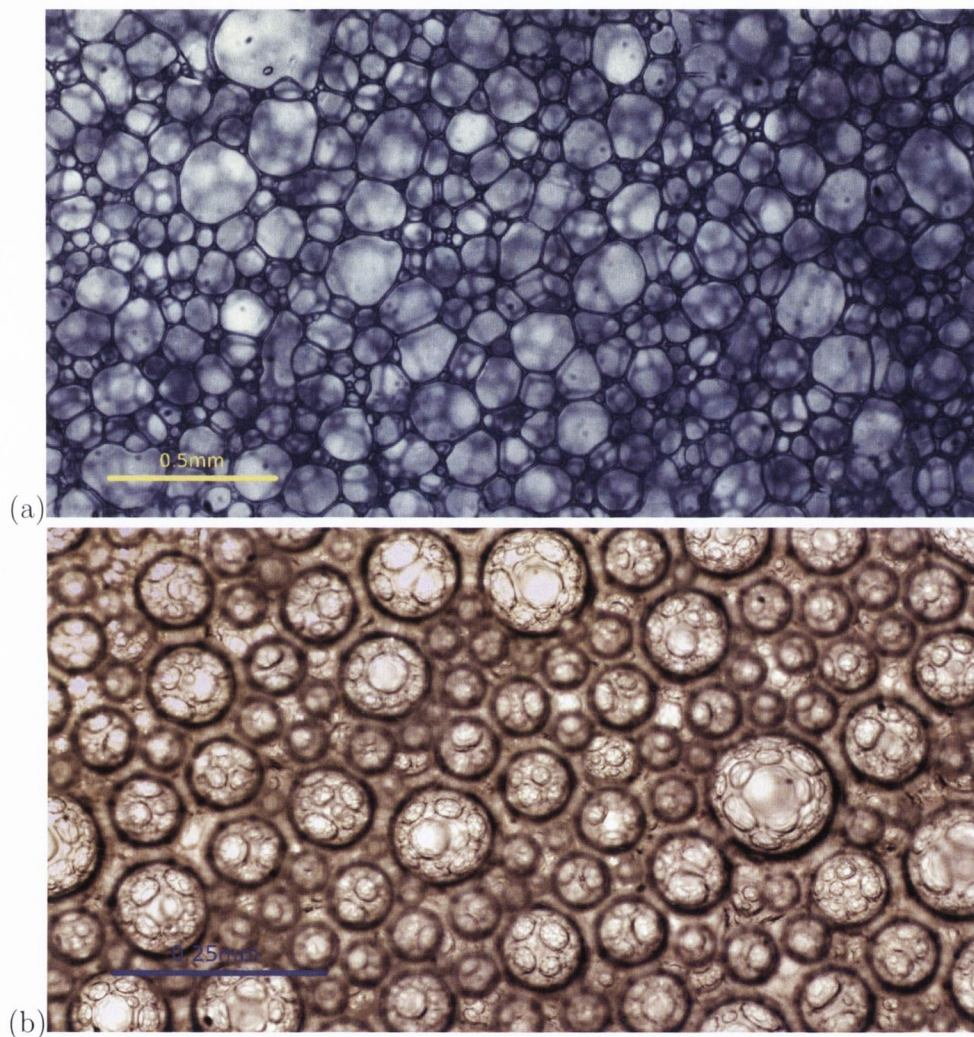


Figure 1.1: **Dry and wet foams.** (a) A three dimensional dry foam consisting of commercial surfactant, air and water, resting on a glass plate and photographed from beneath. Vertices meet at well defined angles described by Plateau's rules [16]. (b) A close-up photograph of the head on a pint of Guinness, which is an example of a wet foam. The bubbles are predominantly spherical, with refraction patterns due to neighbouring bubbles visible on their surfaces. Images courtesy of G. Ryan.

the surface tension. These rules generate the familiar foam structures seen in Figure 1.1 (a). In this thesis, we are concerned with wet foams, where Plateau's requirement of fourfold vertices has been relaxed, and stable vertices (in reality liquid-filled junctions) of higher order can appear [3].

Wet foams have a high liquid fraction; for three dimensional wet foams, it ranges approximately between $15\% \lesssim \phi_l \lesssim 36\%$. In such foams, the bubbles in the dispersed gas phase are well described by spheres, packed in three dimensions, see Figure 1.1 (b). For ease of comparison with different systems well modelled by the packing of spheres, such as granular media, we often instead use the complement of the liquid fraction, the *packing fraction* ϕ , where $\phi = 1 - \phi_l$. In foam experiments this is also called the *gas fraction* or sometimes the *volume fraction*.

Below a packing fraction of $\phi \approx 64\%$, packings of disordered spheres do not (in general) fill enough volume to form a mechanically stable structure [10]. Above $\phi \approx 64\%$, called the *jamming transition* or *random close packing*, the spheres begin to fill enough space to maintain the minimum number of average contacts, $\langle z \rangle$, necessary for mechanical rigidity, $\langle z \rangle = 4$ [17].

1.1.3 The study of foams

The study of foams may be split into four main subject areas: drainage, coarsening, structure and rheology. Drainage concerns the flow of liquid through the Plateau borders of a foam under gravity. Drainage is most relevant for wet foams where the bubbles are larger than the capillary length (as the capillary force opposes drainage under gravity) [3].

Coarsening refers to the diffusion of gas between bubbles driven by pressure differences. As a result, large bubbles tend to get larger, and small bubbles tend to get smaller or disappear altogether. Coarsening has a larger effect in dry foams, as it is easier for gas to diffuse through thin films of liquid [13].

The final two areas are structure and rheology, and it is these two areas which we focus on in this thesis. Structure refers to the topological arrange-

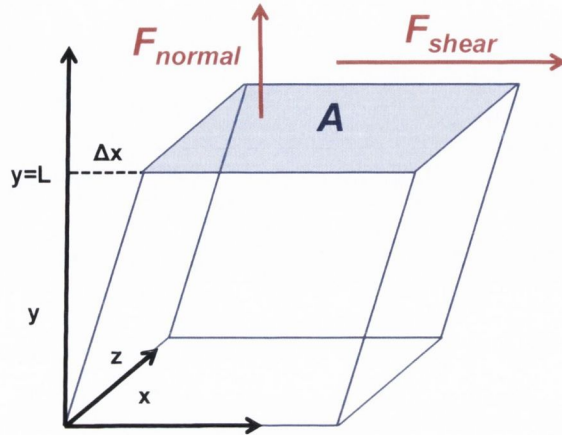


Figure 1.2: **Simple schematic of linear shear.** A shearing force F_{Shear} is applied in the x-direction to the material. The shear stress σ is given by F_{Shear}/A , where A is the area of the plane of flow. The normal stress Π is given by F_{Normal}/A , where F_{Normal} is the normal force. The shear strain γ is the fractional displacement of the shearing plane with width L of the sample, i.e. $\gamma = \Delta x/L$.

ment of the bubbles within a foam. This topology changes under deformation and flow. Rheology is the study of precisely that.

1.2 Rheology of Foams

Rheology, from the Greek *rheo*- meaning “to flow”, is the study of how materials deform and flow in response to an applied stress [13]. Foam rheology is a particularly fascinating topic - liquid foams consist of a gas phase dispersed in a liquid phase, and when they flow the complex motion of the bubbles within the liquid have dramatic effects on the flow properties of the material.

1.2.1 Stress and strain in linear shear

Figure 1.2 shows a schematic diagram of an applied force generating a simple linear shear. The *shear stress*, σ , is defined as the component of the applied force parallel to the shearing plane per unit area,

$$\sigma = \frac{F_{\text{Shear}}}{A}. \quad (1.1)$$

The *normal stress*, Π , is defined as the force normal to the shearing plane per unit area,

$$\Pi = \frac{F_{\text{Normal}}}{A}. \quad (1.2)$$

Stress thus has units of N/m^2 , i.e. the same units as pressure. In simple linear shear, the *strain*, γ is the fractional displacement of the shearing boundary with respect to the width of the channel, $y = L$,

$$\gamma = \frac{\Delta x}{L} \quad (1.3)$$

Strain is unitless, and often expressed as a percentage.

The shear and normal stresses given by Equations (1.1) and (1.2) are special cases. The general description of stress (and indeed strain) are *tensorial*. Consider, for instance, the stress at a point $P(x, y, z)$. This stress can be represented by an *infinitesimal* cube, with three stress components on each of its six sides, denoted by σ_{ij} , see Figure 1.3. In this notation, $i, j \in \{x, y, z\}$, where σ_{ij} is the stress along plane i in the j direction.

In static equilibrium, i.e. no net force on the material in the absence of an applied body force, $\sigma_{ij} = \sigma_{ji}$, and the stress is described by the stress tensor σ_T :

$$\sigma_T = \begin{bmatrix} \sigma_{xx} & \sigma_{xy} & \sigma_{xz} \\ \sigma_{xy} & \sigma_{yy} & \sigma_{yz} \\ \sigma_{xz} & \sigma_{yz} & \sigma_{zz} \end{bmatrix} \quad (1.4)$$

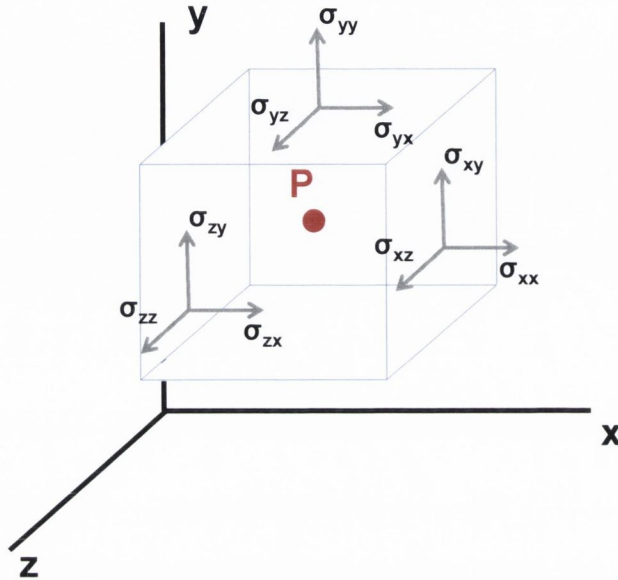


Figure 1.3: **The stress tensor.** An infinitesimal cube around point $P(x, y, z)$. The stress tensor can be represented by three components of σ_{ij} , for $i, j \in \{x, y, z\}$, at each face of the cube.

In our work, we are concerned with the elements of the stress tensor acting on the boundaries in the y plane, defined via Equations (1.1) and (1.2) as $\sigma = \sigma_{xy}$ and $\Pi = \sigma_{yy}$.

A key question for foam rheologists (not to be confused with theologians, who, thanks to the QWERTY keyboard, receive more citations than they should for foam physics) to ask is: if a foam is linearly sheared, how is the resulting strain related to the shear stress?

A simple assumption would be that foams behave like a homogeneous liquid, with the bubbles suspended in the surfactant solution and the properties of the solution determining the nature of the flow. Many homogeneous liquids, including water, obey Newton's equation when subjected to a simple shear, which postulates that the shear stress σ of a fluid is directly propor-

tional to the velocity gradient dv/dy of the fluid in the direction perpendicular to the shear (y-direction),

$$\sigma = c_v \frac{dv}{dy} \quad (1.5)$$

The proportionality constant c_v is called the consistency, which is a general term, dependent on the viscosity. Although Newton first introduced this expression in 1687, it wasn't until the nineteenth century that Navier and Stokes independently developed a full three-dimensional mathematical description of flow, including viscosity, now known as the Navier-Stokes equations [18]. A fluid obeying these equations is referred to as *Newtonian*. Since the shear strain $\Delta\gamma$ over some small time Δt can be expressed as

$$\Delta\gamma = \frac{v\Delta t}{y} \quad (1.6)$$

and thus

$$\dot{\gamma} = \frac{dv}{dy}, \quad (1.7)$$

one can express dv/dy in terms of the strain rate $\dot{\gamma}$, yielding (from Eq 1.5)

$$\sigma = \eta\dot{\gamma} \quad (1.8)$$

where c_v for Newtonian fluids is simply the viscosity, η . From this, we see that for Newtonian fluids, the rate at which the system is sheared is directly proportional to the applied stress.

What about foams? In experiment, foams are observed to be *non-Newtonian*; that is, they do not conform to the Navier-Stokes equations for viscous liquids [19]. This is not surprising, as they are far from homogeneous liquids. The interactions between bubbles within the foam lend the material a degree of rigidity and elasticity. Bubbles in liquid foam do not experience static friction, however, so this structure can readily undergo rearrangements and flow under shear.

For low strain of less than a few percent, the foam deforms elastically. In this regime the shear stress can be related to the strain via the elastic modulus G_0 , where

$$G_0 = \frac{\sigma}{\gamma}. \quad (1.9)$$

For such small strains, the deformations are reversible. At a certain *yield stress*, σ_Y , however, the foam *yields* and begins to flow. During this flow, the foam undergoes irreversible topological changes, known as T1 transitions. Foams are therefore an example of yield stress fluids: solid below a yield stress with fluid-like properties above the yield stress.

1.2.2 The Herschel-Bulkley equation

The flow of foam and the relationship between shear stress and strain rate can be described empirically by the Herschel-Bulkley equation,

$$\sigma = \sigma_Y + c_v \dot{\gamma}^n. \quad (1.10)$$

c_v is once again the consistency, a function of the viscosity, and n is known as the Herschel-Bulkley exponent [3]. The second term is often referred to as the *viscous stress*, $\sigma_{\text{visc}} = \sigma - \sigma_Y$. The relation was first formulated by Herschel and Bulkley, in their 1926 study of the response of rubber [20]. The simple case of $n = 1$ is a so-called *Bingham fluid*. This exponent is typically found to have values between $0.25 < n < 0.7$ for aqueous foams [21–29]. The Herschel-Bulkley relation has also been observed to hold for emulsions and granular media [27, 30–33].

We can conclude that while sharing similarities with both viscous liquids and elastic solids, a foam is neither. Hence it is often categorized as a so-called *visco-elastic liquid*. For low strain, the material deforms elastically via Equation (1.9). Past some yield strain γ_Y , with an associated yield stress $\sigma_Y = G_0 \gamma_Y$, the material yields and flows. A schematic representation of this stress-strain relationship is shown in Figure 1.4. In this flowing regime,

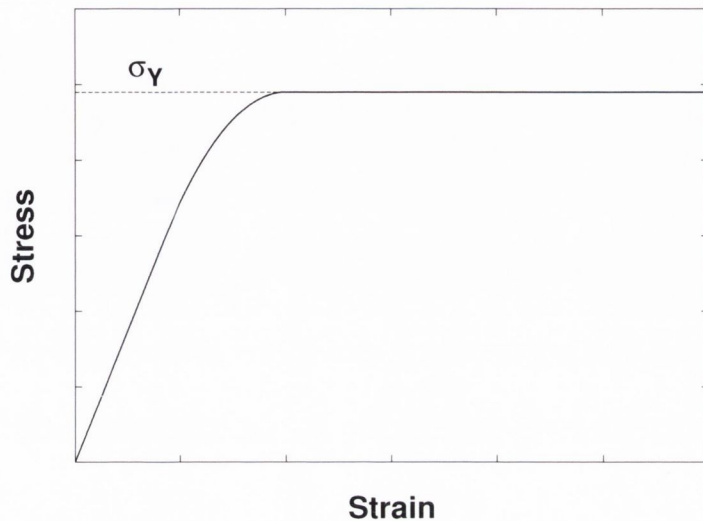


Figure 1.4: **Stress versus strain for a visco-elastic medium.** Once the stress exceeds the yield stress σ_Y , the material deforms and begins to flow.

foams behave like a *shear-thinning fluid*, which means that their effective viscosity, η_{eff} ,

$$\begin{aligned}\eta_{\text{eff}} &= \frac{\sigma}{\dot{\gamma}} \\ &= \frac{\sigma_Y}{\dot{\gamma}} + \frac{c_v}{\dot{\gamma}^{(1-n)}}\end{aligned}\tag{1.11}$$

is a decreasing function of strain rate [13, 34]. We are familiar with such liquids from everyday life, as their properties are often useful. For instance, shaving foam is a visco-elastic fluid. When it sits on your hand it remains rigid, but once a stress is applied it spreads easily across your face.

The strongly non-linear, macroscopic response to shear originates from complex, microscopic interactions between bubbles in the flowing foam. Probing the nature of these interactions and attempting to link them to the bulk rheology of the foam is the main aim of this thesis.

1.2.3 Foams in two and three dimensions

As is the case in many areas of physics and mathematics, one of the first steps in understanding such complex behaviour and interplay is to reduce the dimensionality of the system. In this thesis we focus exclusively on simulations in two-dimensions (2D), although we reference many experiments performed for three-dimensional (3D) foams.

Initially, 2D foams were introduced as a model system for numerical and theoretical studies [35,36] of foams, as they present simpler systems to treat mathematically. More recently, there have been a variety of experiments involving quasi-2D foams, consisting of a single layer of bubbles [23–26], depicted in Figure 1.5. The motivation for studying rheology of 2D foams stems from the belief that theories explaining these simpler 2D systems could be expanded to 3D foams with more complicated structures. This belief seems justified: compared with their 3D counterparts, 2D foams are seen, for example, to share similar scalings of yield stress [13,37,38] and elastic modulus [17] with packing fraction. In addition, both 2D and 3D foams are well-described by the Herschel-Bulkley equation with similar exponents [21,23,25,26,29].

Focusing on two dimensions presents a number of advantages, in addition to being a simpler starting point for theorists. In experiments, it is much easier to process images and track bubble positions and motion in 2D. In 3D, more limited or more difficult techniques must be used, such as X-ray tomography, required to resolve the centres and dimensions of the cells [41], or confocal microscopy with refractive index-matched emulsions [42]. In simulations, the decreased average contact number between bubbles (from 14 to 6) reduces the intensiveness of calculations and allows for the study of larger system sizes [43]. Nevertheless, despite the reduction of complexity in 2D compared to 3D, 2D retains subtleties which we shall explore in the coming chapters.

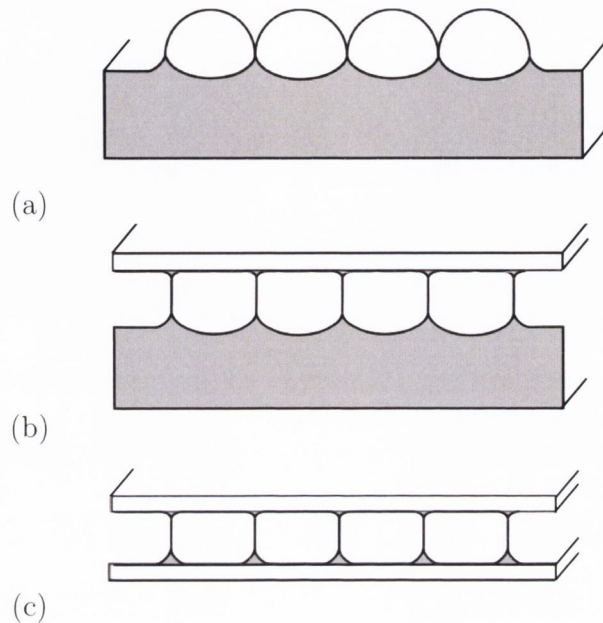


Figure 1.5: **Three types of 2D foam (side view)**. (a) Monolayer of bubbles sitting at an air/liquid interface. This configuration is also called a Bragg raft, after its namesake who proposed it as a model for atomic arrangements in a crystal [7]. (b) Bubbles floating in a liquid, confined by a single top plate (confined Bragg raft). (c) Bubbles confined between two glass plates (also known as a Hele-Shaw cell). The bubbles in (b) and (c) are subject to a drag force as they move across the plate(s), which has been found to scale as a power-law function of their velocities [39,40].

1.2.4 Experimental geometries

Also of importance in rheological experiments and simulations is the geometry of the system. When investigating linear shear, two main geometries are used, schematic 2D examples of which are shown in Figure 1.6. The first is a simple linear cell, Figure 1.6 (a). In experiments, this cell has a finite length and width. It can have a single shearing boundary and a stationary boundary. Alternatively both boundaries can be set in opposing motion. Both produce linear velocity profiles across the channel, and thus the strain rate is constant throughout the foam. In simulation, periodic boundary conditions are often used in some or all dimensions.

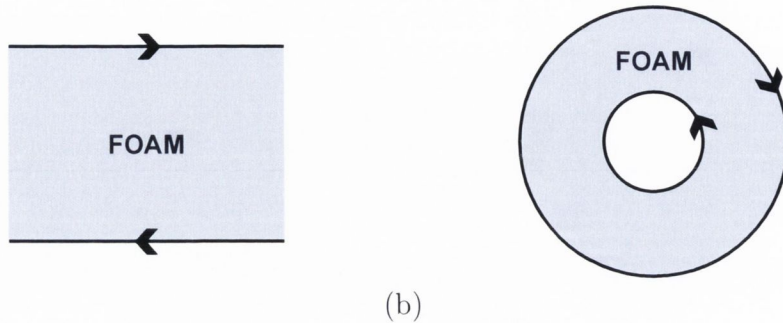


Figure 1.6: **Linear and circular Couette geometries.** (a) Linear geometry. Black arrows indicate the motion of the shearing boundary. (b) Circular Couette geometry, for 2D foams, analogous to a cross-section of the cylindrical Couette geometry for 3D.

The other geometry is a circular Couette geometry, Figure 1.6 (b). Here, the foam sample is contained between two concentric circles (or cylinders, in 3D). One or both of these cylinders rotate, shearing the foam. This leads to a shear stress across the sample which decays as $1/r^2$, where r is distance from the centre of the cylinder. One advantage to this system, however, is that there is no finite maximum shear that can be achieved in experiment, unlike linear cells.

In a discussion of geometry, we shall also include the presence or absence of a slip condition at the shearing boundary, and the presence or absence of a top plate for 2D foams, see Figure 1.5. Both of these factors can affect the flow and velocity profiles of the foam under shear.

In the case of the former, rough walls are typically used to ensure a no-slip condition at the shearing boundary. In the case of the latter, the presence of a top plate imposes a drag force on each bubble in contact with it, which has been found to scale as a power-law function of their velocities [39, 40]. In 3D this is a negligible effect, as the majority of the bulk is not in contact with the walls. Conversely, this has a large effect in 2D, as every bubble is subject to the additional drag force. The presence of a top plate has been attributed as the main cause of *shear localisation* (i.e. flow in one region, but not another) in 2D foams [44–47].

1.2.5 Summary

We have seen that rheological systems can be described in terms of many different parameters and qualities. In this thesis, we consider:

- **Simulations** of wet foams in 2D.
- These foams are confined in a linear channel, with semi-periodic boundary conditions.
- They are sheared at a constant strain rate.
- There are two well-defined, rough boundaries.
- There is no top-plate drag, or equivalent mechanism, implemented.

These parameters are consistent with a range of foam rheology experiments in the literature [29, 48–50].

The model we use to simulate wet 2D foam is the widely used soft disk model, first conceived by Durian [36, 51] and implemented with the modifications of Langlois [52]. We summarise their findings in Section 1.4.1, and we give a detailed account of the implementation of the model in this thesis in Chapter 2.

1.3 An overview of foam rheology experiments

In this section, we give a brief overview of some of the experimental work which has been done in the field of wet foam rheology. We shall pay particular attention to literature focused on interactions at the bubble level, and their effect on flow.

1.3.1 Classification of wet foam rheology by Princen *et al.*

We shall start our overview with the works of H.M. Princen, in his four papers *Rheology of foams and highly concentrated emulsions I-IV* [27, 53–55] and his work with Schwartz [56]. The first of the four, published in 1983, notes “while experimental work on the rheology of these systems is scant, there appears to be a virtual lack of theoretical understanding of how the rheological properties are linked in a quantitative way to system parameters”.

To that end, Princen was the first to theoretically model the behaviour of 2D foam by considering the bubbles as monodisperse cylinders of low thickness (or disks). He also envisioned the first stress- and strain-controlled shear experiments, although acknowledging that they were not possible for a system of cylinders [53]. He performed extensive theoretical analysis and experimental measurements (in conjunction with Kiss [27]) of properties of foams and emulsions such as yield stress, elastic modulus and effective (or shear) viscosity.

Princen was also the first to classify and illustrate what is now known as the T1 transition, so named shortly thereafter by Weaire and Rivier [57]. His representation of what he called a “Mode I to Mode II transition” is reproduced in Figure 1.7. We now know that these rearrangements are intrinsically linked to the nonlinear response of the foam. Princen, however, treated them as a geometrical adjustment to his model, which comprised of layers of bubbles sliding past one another in lanes, often referred to as *laminar flow*.

Finally, Schwartz and Princen extended their model of layered bubbles sliding past one another. They modified Bretherton’s [39] theoretical approach to the motion of long bubbles in tubes, taking the primary dissipative force in a linearly-sheared 2D foam to be the viscous dissipation due to the extension of soap films as the foam flows. From this, they formulated a relationship between stress and strain rate, finding a Herschel-Bulkley exponent of $n = 2/3$ [56]. This exponent was corroborated by Reinelt and Kraynik’s similar model [58]. In experiments in the cylindrical Couette geometry, Prin-

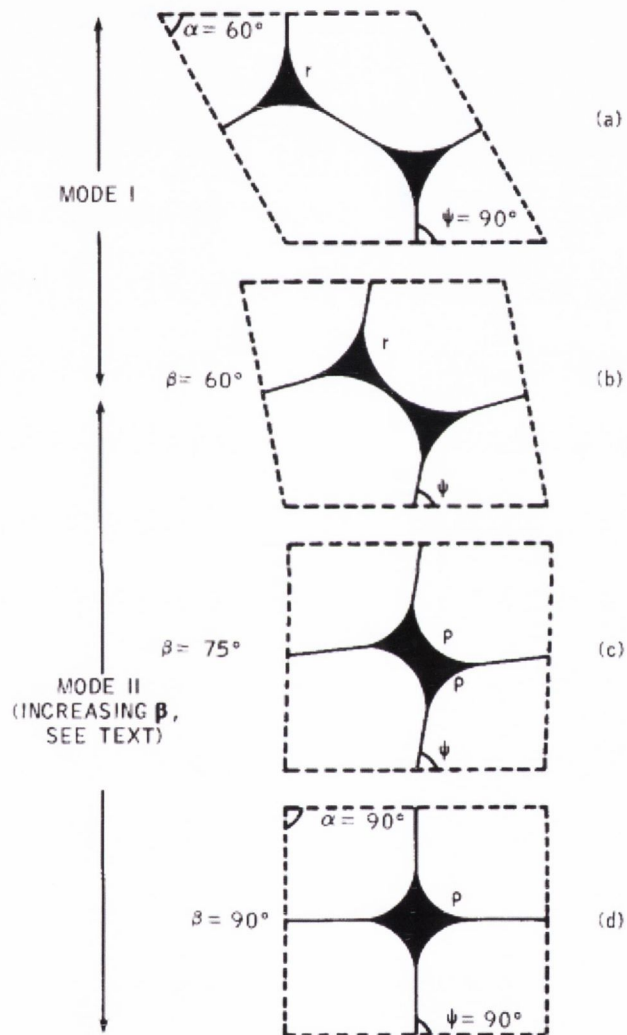


Figure 1.7: **A T1 transition.** Figure reproduced from [53]. Princen was the first to characterise these structural changes for wet foams, which he called a “Mode I to Mode II transition”.

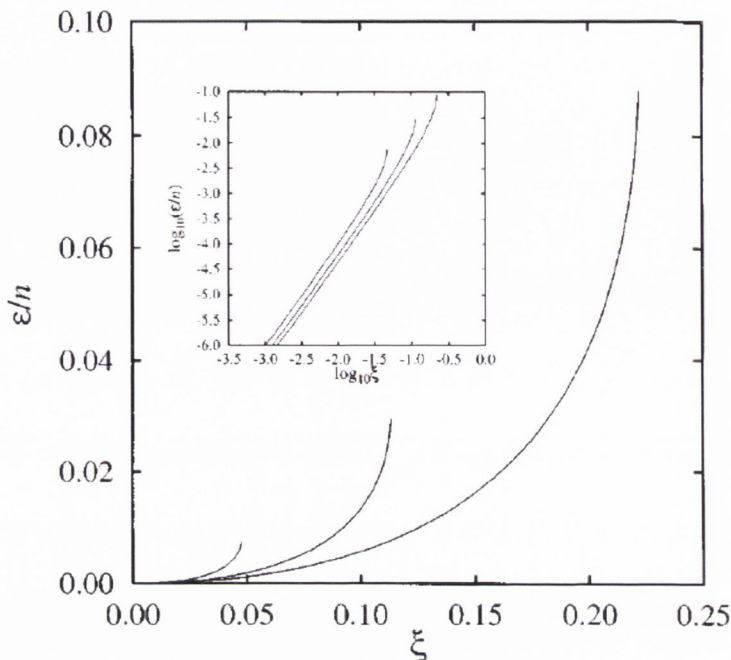


Figure 1.8: **Excess energy per facet of a compressed bubble in 2D.** Figure reproduced from [59]. Excess energy ϵ per facet n for the tessellating cases $n = 3, 4, 6$, versus ξ , where ξ is a dimensionless displacement proportional to compression. For small compressions in 2D, Lacasse observed scaling with a power law exponent of 2 (see inset, plotted on a log scale), consistent with harmonic repulsion between bubbles.

cen and Kiss instead found an exponent of $n = 1/2$ [27]. They attributed the discrepancy to disjoining pressure effects, although with the benefit of hindsight it is likely due to the investigation of strain rates over which laminar flow was a questionable assumption.

1.3.2 Deformation of droplets by Lacasse *et al.*

In relating bubble dynamics to macroscopic rheology, it is important to quantify the forces governing bubble-bubble interaction. Lacasse *et al.* studied emulsion droplets compressed between multiple plates [59]. For two plates, this compression was solved for analytically. For n plates, the compression was found numerically, using Brakke's Surface Evolver [60]. They found that,

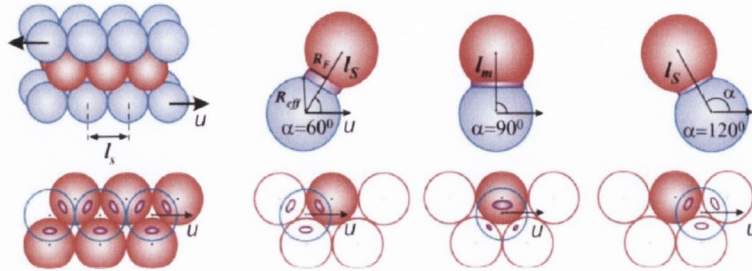


Figure 1.9: **Viscous drag between bubble layers.** Figure reproduced from [22], showing the formation of films between bubbles as layers slide past one another.

while in 3D the compression depends on the number of neighbours, in 2D the compression was well described by harmonic elastic repulsion for small deformations.

The interfacial energy of a circular droplet in 2D is given by the line tension (that is, the 2D surface tension) times the length of the perimeter. Figure 1.8 shows the dimensionless excess energy, ϵ , versus dimensionless displacement, ξ , directly proportional to compression. The excess energy is defined for 2D as $\epsilon = \frac{l}{2\pi R} - 1$, where R is the radius of a circular droplet and l is the perimeter of the compressed droplet. Thus, $\epsilon = 0$ for an uncompressed droplet. For harmonic repulsion, $\epsilon \sim \xi^2$, which Lacasse *et al.* find for compressions up to approximately 5% [59], see Figure 1.8 (inset).

This analysis forms the basis for the choice of elastic repulsion scaling in our simulations of 2D foams, introduced in Section 2.1.

1.3.3 Experiments of Denkov *et al.*

The experiments of Denkov *et al.* in Sofia University have characterised extensively the chemical properties of foam surfactants and their effect on foam rheology, so much so that at present the standard surfactant solution used for ease of comparison between experiments in the field is often referred to as the “Bulgarian recipe”.

In experiment, Denkov *et al.* have measured exponents for the Herschel-Bulkley equations, classifying them by *mobile* and *immobile* interfaces. For

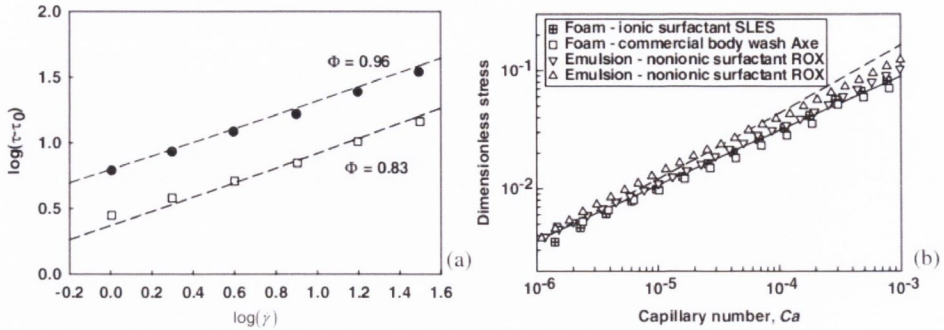


Figure 1.10: **Comparison of viscous drag law theory with experiment, for emulsions and foams.** Figure reproduced from [22]. (a) Viscous stress $\sigma - \sigma_Y$ (here called $\tau - \tau_0$) plotted versus strain rate $\dot{\gamma}$ for oil in water emulsions, for packing fractions $\phi = 0.83$, $\phi = 0.96$. (b) Dimensionless stress for foams and emulsions stabilised with synthetic surfactants, versus capillary number $Ca = \eta R_{32} \dot{\gamma} / \Gamma$. Γ is the surface tension, and R_{32} is the so-called *Sauter mean radius* $R_{32} = \langle R^3 \rangle / \langle R^2 \rangle$, the ratio of the third moment and the second moment of the size distribution of bubble radii R . The dimensionless capillary number Ca is thus directly proportional to strain rate. Denkov *et al.* observed excellent agreement between their model and experimental results, for laminar-type flow, finding the viscous drag proportional to $\dot{\gamma}^{0.465}$.

immobile, rigid interfaces, an exponent of $n \approx 0.3$ was found. For mobile interfaces, with lubricated sliding motion of bubbles past one another, Denkov *et al.* found an exponent $n \approx 0.5$ for foams and emulsions [21, 22, 61].

Recently, they have proposed a model based on this sliding motion for mobile interface, ordered 3D foams and concentrated emulsions. During steady flow, the structure periodically rearranges, and contact films form and disappear upon transient bubble collisions (see Figure 1.9). They found excellent agreement for their model, particularly noting that they collapsed data for foams of different bubble sizes with no free parameters [22], see Figure 1.10. However, this model linking bubble dynamics to bulk rheology again assumes laminar flow. While this type of flow is observed in experiments of Denkov and others at high strain rate, is not consistent with observed low strain rate flow, where the bubbles move in more turbulent patterns [29, 48, 62]. We investigate this flow regime in Chapter 3.

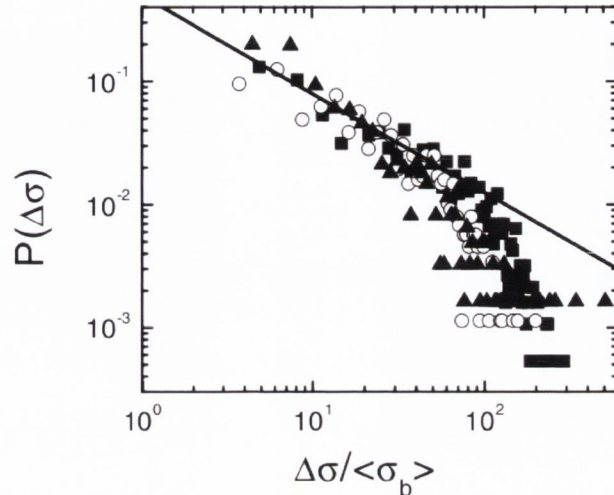


Figure 1.11: **Distribution of stress drops in a sheared foam.** Figure reproduced from [63]. Data for three different strain rates, $\dot{\gamma} = 0.031s^{-1}$ (\blacktriangle), $\dot{\gamma} = 0.31s^{-1}$ (\blacksquare), $\dot{\gamma} = 0.48s^{-1}$ (\circ). The solid line has a slope of -0.8 . Dennin suggests truncated power law scaling for stress falls.

1.3.4 Experiments of Dennin *et al.*

Dennin and co-workers have performed extensive experiments on wet foams under linear shear in 2D and 3D, and in linear and cylindrical geometries [23, 25, 62, 63]. They measured frequency of T1 transitions [23], response of the shear stress to linear and oscillatory strain [63, 64], the effect of channel dimensions [50], and the minimum strain for which the steady-state flow of foam can potentially be considered as having equivalent time- and ensemble-averages [65], among many other properties.

Of particular interest to our work in this thesis are the measurements by Dennin *et al.* of shear stress fluctuations in 2D foams. Motivated by measurements initially made by Durian in simulation, covered in Section 1.4.1, Dennin examined distributions of stress falls $\Delta\sigma$, see Figure 1.11. He found a truncated power law scaling of $P(\Delta\sigma) \sim \Delta\sigma^{-0.8}$, consistent with a fat tailed distribution often associated with avalanche-like rearrangements [63]. Lauridsen and Dennin then went on to examine the frequency of structural rearrangements during shear in an attempt to relate bubble-scale interactions

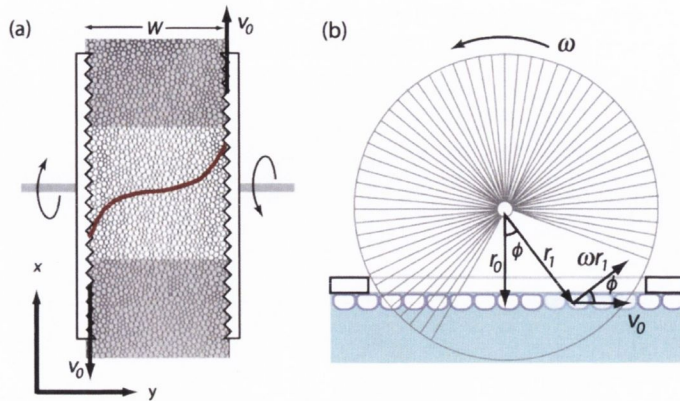


Figure 1.12: **Experimental setup of linear shear.** Figure reproduced from [48]. (a) Schematic top view of the experimental setup. Two counter-rotating wheels are partially immersed in the fluid, separated by a gap, linearly shearing the foam. The red line shows the average velocity profile during steady state flow. (b) Side view, relating angular velocity ω to strain rate.

to the rheology, finding a qualitative alignment between spikes in the number of T1 transitions, and falls in the macroscopic shear stress [23].

1.3.5 Bubble fluctuation experiments of Katgert *et al.* and Möbius *et al.*

The experiments of Katgert *et al.* and Möbius *et al.* in the Leiden group concerned steadily sheared foam in both linear and cylindrical Couette geometries. The rheological measurements were carried out in a Couette cell, whilst in the linear apparatus (shown in Figure 1.12), they performed a novel and extensive study of bubble fluctuations in time using image analysis.

By shearing two layers of bubbles in a 2D foam past one another in a circular Couette geometry, they measured the viscous drag force experienced by bubbles sliding past one another, as a function of their relative velocity. They found this dissipative force to scale with the relative velocity to the power of an exponent approximately equal to 0.7, very close to the bubble-wall drag coefficient measured, and theoretically proposed by Bretherton to be $2/3$ [39] as discussed in Section 1.3.1. This yields a second scaling rela-

tionship for the forces governing bubble-bubble interaction, in conjunction with the work of Lacasse (Section 1.3.2).

In addition to measuring the bubble-bubble interaction in experiment for the first time, Möbius *et al.* subsequently used image analysis to resolve the flow of individual bubbles in time [29]. From this, they were able to calculate displacement distributions, and study the scaling of the mean square displacements $\langle \Delta s^2 \rangle$ over a time interval Δt . Their results are shown in Figure 1.13.

At short times, they observe fat-tailed distributions consistent with strong, non-affine flow (that is, flow that deviates from the mean flow). They found that the bubbles undergo a process akin to random-walk diffusion, induced by rearrangements due to shear, at sufficiently long times. This allowed them to fit diffusion constants, and they went on to propose a deformation-relaxation argument relating bubble fluctuations to macroscopic rheology. Inspired by this method, we expand on this work in Chapter 3.

1.3.6 Experiments of Pouliquen *et al.* and Lespiat *et al.*

Pouliquen and co-workers have recently developed a constitutive relation for dense granular flows, which has been successful in predicting, in complementing experiments performed by Jop *et al.*, the flow behaviour and shape of velocity profiles without any fitting parameters [32].

The model, which we define mathematically in Section 2.3, relates the shear stress to the strain rate via the so-called I parameter. This parameter, which is the square root of the Coulomb number from granular media literature [66], can be viewed as the ratio of the deformation timescale to the typical timescale of rearrangement in the medium. In the original form of Pouliquen *et al.*, the latter is governed by friction between grains and the confining pressure.

Lespiat *et al.* showed that this constitutive model also holds for foams, with modification. In the absence of static friction, they assert that the rearrangement rate is governed by the viscous dissipation and the normal

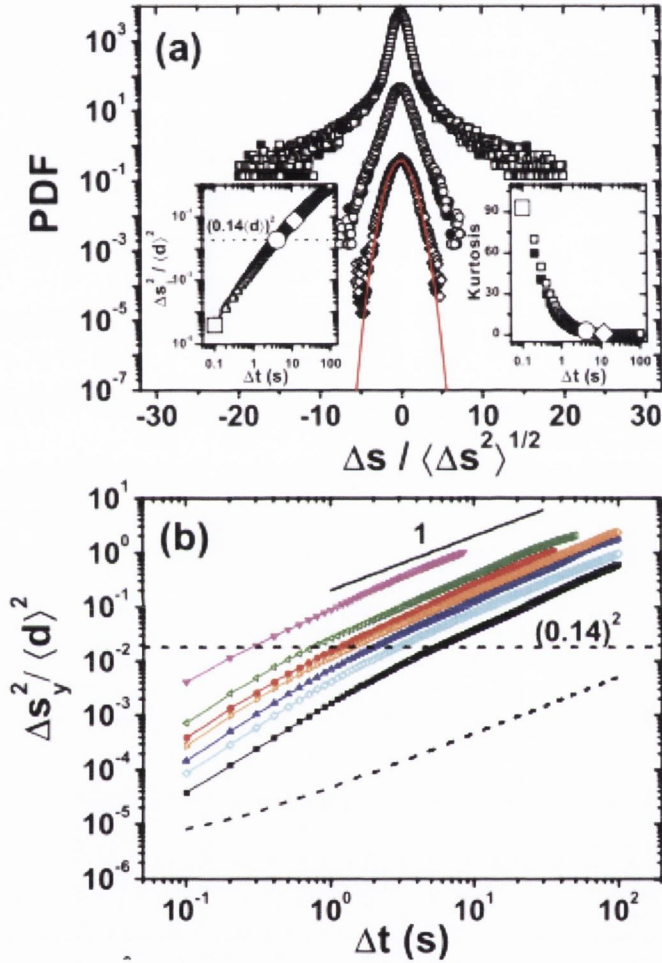


Figure 1.13: Evolution of mean square bubble displacements in time. Figure reproduced from [29]. Möbius *et al.* used image analysis to track individual bubble motion in a flowing 2D foam. (a) Probability distributions of bubble displacements evolving in time. At short times, the distributions are fat-tailed; at long times the distributions tend to Gaussian. (b) Mean square displacements, normalised by average bubble diameter, versus time lag. The slope 1 region corresponds to the onset of shear-induced diffusion.

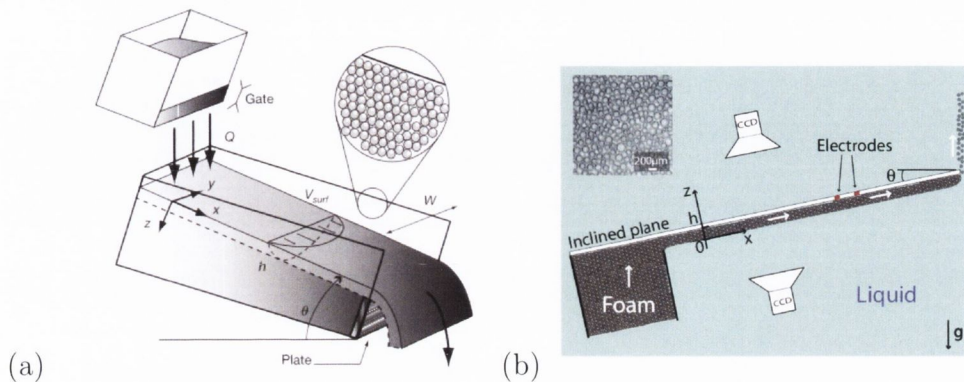


Figure 1.14: **Inclined plane linear shear for grains and foams.** (a) The experimental setup of Jop *et al.* [32]. The setup is tilted until the grains begin to flow, past the static angle of repose. (b) The analogous experimental setup for foams of Lespiat *et al.* [30]. The system is inverted, with buoyancy for foams taking on the role of gravity for grains, and the bubbles flowing upwards.

pressure, and find good agreement for their experimental results for both foams and granular media [30].

In both cases, the relation was investigated using an inclined plane experimental setup, as shown in Figures 1.14 (a) and (b). For a granular medium, the plane is tilted until the grains begin to flow, and a velocity profile is extracted as a function of channel width. The ratio of the shear and normal forces can be extracted from the tilt angle. For foams, buoyancy plays the role of gravity, and the foams flow up the plane.

In both experiments, the angle where the material just begins to flow corresponds to the *static angle of repose* [67]. Fitting to the functional form proposed for the scaling of the constitutive model with strain rate allows one to extract a value for the angle of repose in a linear geometry, which we shall cover in greater detail in Sections 2.3.3 and 4.2.1.

1.3.7 The non-local continuum model of Goyon *et al.*

A popular model for foam flow in 2D, which up until now we have not discussed, is the continuum model. Unsurprisingly, such a model considers a

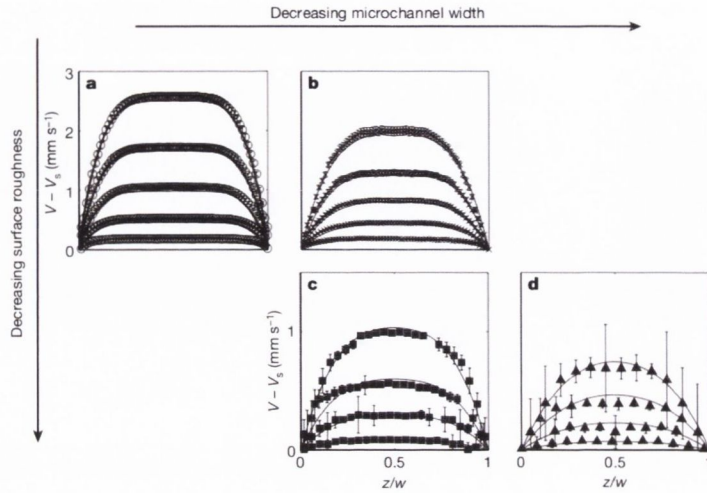


Figure 1.15: **Velocity profiles predicted by the non-local model, for varying channel width, w .** Figure reproduced from [31]. The non-local model expands the continuum model using a coordination length associated with non-affine bubble motion. The solid black lines indicate the model's predictions as a function of channel width (left to right) and surface roughness (top to bottom). They are seen to accurately capture the behaviour of the measured data and the finite size effects of narrow channels.

foam flow as a continuum, i.e. a homogenous fluid whose flow is described by modified differential equations of fluid mechanics [45]. It has been successful in describing, for instance, the occurrence of shear localisation in 2D flow [68].

As such, this model may perhaps be considered the antithesis to this thesis, which is concerned precisely with deviations and fluctuations from the mean flow. Recently, however, Goyon *et al.* have introduced the so-called non-local model - a modification to the continuum model to take into account long-range spatial cooperativity they observe in the flow of emulsions [31].

Ordinarily, the continuum model is a purely local model, where the flow properties are a function of the position x with no consideration for events happening nearby. It has been observed, however, that topological changes in a foam induce further topological changes nearby. This effect is particularly important when the characteristic length associated with shear, or the channel dimensions, are of the order of the bubble size [69]. Goyon *et al.*

define a *fluidity*, f , where for the bulk $f = 1/c_v$, where c_v is the consistency from the Herschel-Bulkley relation, Equation (1.10). The fluidity f is defined to obey a non-local scaling governed by a *non-locality length* ξ . They found their modification successfully described velocity profiles of flow in narrow channels, with no free parameters, shown in Figure 1.15.

Such a model may provide a stepping stone between the analysis in this thesis and the continuum model for foam flow.

1.4 An overview of foam rheology simulations

In the previous section we examined experimental work on the rheology of wet foams and dense granular flows. We shall now turn to simulations which have been performed in a effort to model and understand these systems. Once again, we shall focus on papers which have aimed to relate individual dynamics to macroscopic rheology, starting with the development of the soft disk model as a simulation of 2D wet foams under shear.

1.4.1 Durian, Langlois *et al.*, and the Soft Disk Model

Early simulations of foams made use of cellular representations of foams in *quasistatic* simulations. By “quasistatic” we refer to simulations where the foam is at all times in a state of energetic equilibrium, with small perturbations from a stable state followed by energy minimisation. These include the simulations of Weaire and Kermode [70–72], PLAT simulations of Bolton, Weaire and Hutzler [35, 38, 73–75], and simulations using Brakke’s Surface Evolver [60].

As implied by the name, quasistatic simulations are not well-designed for capturing the *dynamics* of a system. Furthermore, while dry foams are well described by Plateau’s rules, wet foams are not found to obey such rigid geometrical strictures. Durian was among the first to tackle the dynamics of wet foams using a simpler, non-cellular representation of the bubbles. This model is referred to as the soft disk model (or, also, the bubble model).

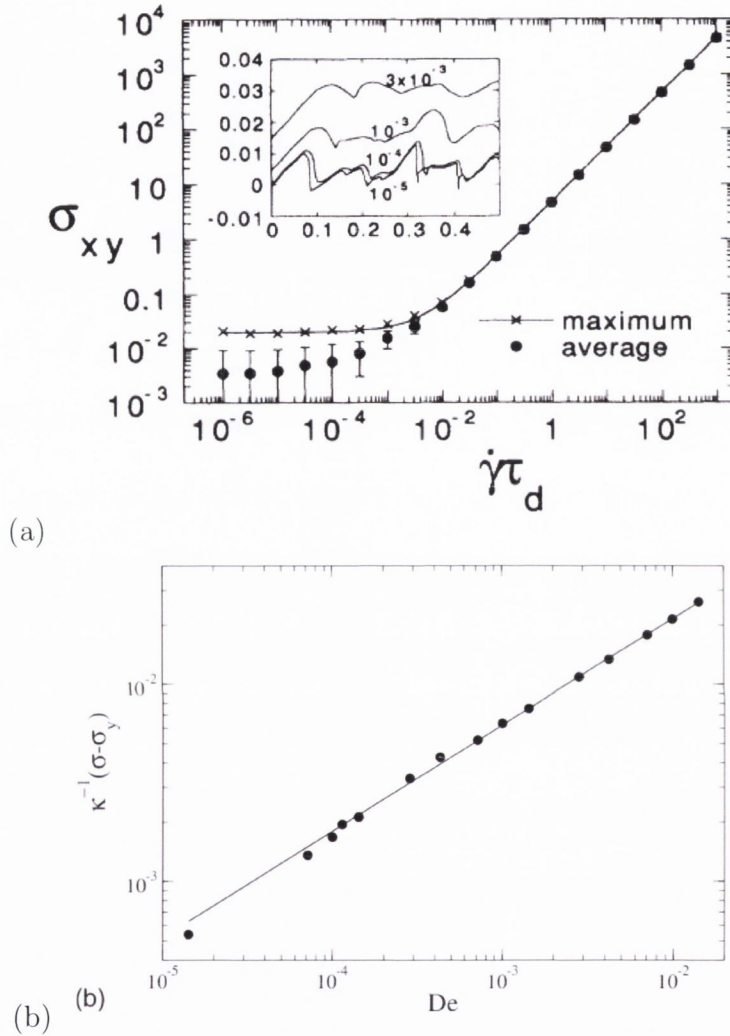


Figure 1.16: **Stress and strain rate in the simulations of Durian and Langlois *et al.*** (a) Stress versus strain rate in Durian's original soft disk model, using the mean field approximation for viscous drag. He found that the relationship was well described by that of a Bingham fluid, with the Herschel-Bulkley exponent $n = 1$. Figure reproduced from [51]. (b) Stress, minus the yield stress, versus dimensionless strain rate $De \propto \dot{\gamma}$, for the soft disk simulations of Langlois *et al.* The introduction of individual viscous drag forces had a dramatic effect. Langlois *et al.* found the flow behaviour to be well described by a Herschel-Bulkley equation fit with an exponent of 0.54, in much better agreement with experiment. Figure reproduced from [52].

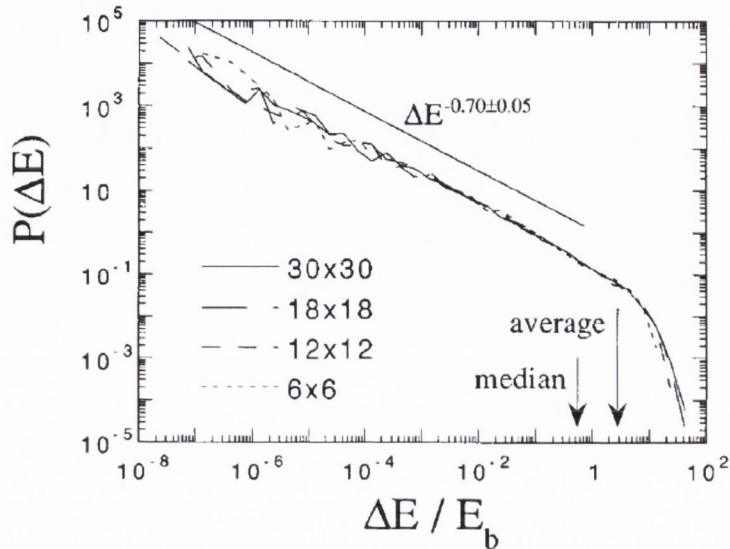


Figure 1.17: **Elastic energy fall distributions.** Durian looked at distributions of falls in the elastic energy, ΔE , in the system, similar to the stress falls examined by Dennin and shown in Figure 1.11. He also noted truncated power law scaling, which he attributed to avalanche-like rearrangement behaviour. Figure reproduced from [36].

The soft disk model represents the bubbles in foam as a series of disks, confined in some geometry. These disks are referred to as “soft” because they are allowed to overlap. Overlapping disks are subject to two forces: an elastic repulsion related to their overlaps, and a viscous dissipation. Durian chose a harmonic elastic repulsion, and used a mean-field approximation for the viscous force. A bubble experienced a dissipative force directly proportional to the mean flow velocity in its vicinity. The system was subjected to a constant strain rate imposed by a moving boundary, and the rheology investigated.

Durian found that the foam responded as a Bingham fluid, that is a fluid which obeys the Herschel-Bulkley equation (1.10) with exponent $n = 1$, see Figure 1.16 (a) [51]. Durian noted that this qualitatively agreed with Bingham-plastic-like behaviour of foams at high strain rate, and attributed this scaling to his choice of linear local laws, namely a harmonic repulsion

directly proportional to the overlaps between disks and a viscous drag directly proportional to the mean velocity.

Langlois *et al.* went on to improve on the simulations of Durian. In addition to greatly increasing the system size (by an order of magnitude or more), they modified the simulation to remove the mean-field approximation. Now, the viscous dissipation experienced by a bubble i in contact with a bubble j was set to be directly proportional to the relative velocity between i and j , thus dynamically changing in time in a fashion similar to the harmonic repulsion force.

The results were dramatic, see Figure 1.16 (b). Without the mean field approximation, strongly non-linear flow was resolved, with a Herschel-Bulkley exponent of $n = 0.54 \pm 0.01$ found by Langlois *et al.*, in closer agreement with values measured for foams and emulsions in experiment (Section 1.3).

The soft disk model makes no attempt to model foams as the liquid fraction decreases to the dry limit, where bubbles are polygonal, subject to elongation and deformation, and no longer well described by disks or spheres. However, for wet foams, and indeed some other granular media, the model has been shown to capture the key characteristics of flow [76–80]. We use the soft disk model, as implemented by Langlois *et al.*, in this thesis. We define the model in much greater detail in Chapter 2.

Returning to Durian’s original work, Durian [36] and later Ono *et al.* [81] looked at fluctuations in the elastic energy. Specifically, Durian was interested in the distribution of energy drops, and how these related to structural rearrangements, see Figure 1.17. He found a truncated power law scaling for elastic energy falls ΔE , described by an exponent $P(\Delta E) \propto \Delta E^{-0.7}$ [36]. He associated this power law scaling with avalanche-like rearrangements in the foam. Dennin later investigated analogous falls in the shear stress and their relationship with T1 transitions, as mentioned in Section 1.3.4.

These results, although somewhat qualitative, attempt to link microscopic bubble rearrangements to the foam rheology. We develop a quantitative approach to the investigation of stress fluctuations in Chapter 5.

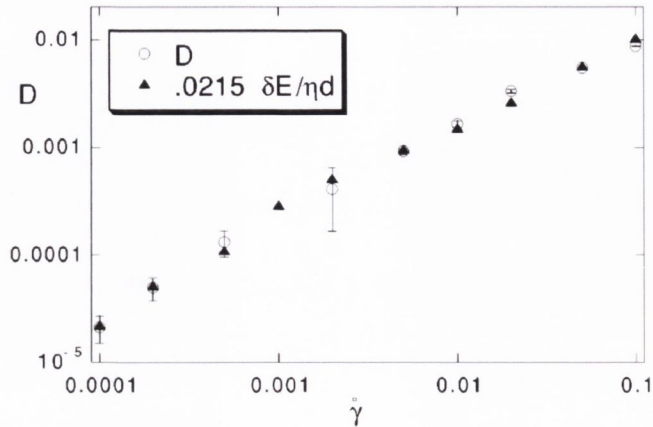


Figure 1.18: **Shear induced diffusion and the Stokes-Einstein relation.** Diffusion constants, D , associated with shear induced rearrangements, versus strain rate, $\dot{\gamma}$. The black triangles represent the Stokes-Einstein equation as envisaged for foams by Ono *et al.* [81], which they found to agree with their diffusion constants with one fit parameter. Figure reproduced from [81].

1.4.2 Simulations of Ono *et al.*

Building on the work of Durian, Ono *et al.* performed extensive soft disk model simulations, focusing on the velocity fluctuations of bubbles under shear [81]. They observed that motion of individual bubbles transverse to the mean flow was diffusive. This diffusion differs from thermal diffusion, where the random-walk motion is caused by vibrations proportional to temperature. Instead, successive rearrangements under shear are found to evolve diffusively in long time. Ono *et al.* were the first to measure such *shear-induced diffusion*, fitting diffusion constants $D(\dot{\gamma})$ as a function of strain rate, shown in Figure 1.18.

They found D to scale non-linearly with strain rate, and noted, furthermore, that D did not have a simple power law relationship with $\dot{\gamma}$. Ono *et al.* also identified a critical strain rate, exceeding the typical rate of rearrangement in the system. They noted that past this critical strain rate, fluctuations were essentially dominated by the timescale of deformation, observing that spatial correlations decayed exponentially in the limit of high

strain rate. This change in macroscopic behaviour past some critical rate of deformation shall play a key role in arguments we make in Chapter 3.

The simulations of Ono *et al.* were the most extensive of their kind using the soft disk model, and their study of fluctuations bears direct relevance to this thesis. However, we note that they were performed using Durian's implementation of the soft disk model, with a mean field approximation. This approximation was shown to have a dramatic effect on bulk rheology by Langlois *et al.* [52], and was later shown to cause spurious correlations in fluctuations by Tighe *et al.* [79].

1.4.3 Jamming in the soft disk model: Olsson and Teitel, and O'Hern *et al.*

The soft disk model comprises of interacting disks governed by an elastic repulsion and a viscous dissipation. There is no attractive force in the system, with the system instead held together in mechanical stability by the confining geometry.

To understand such systems under shear, it is important to understand their structural properties. Particularly, what, for a given arrangement of disordered spheres in a confining volume, determines whether a packing will be mechanically stable? In 2D, a disk needs (in general) no fewer than 3 contacts to prevent movement. In 3D, a sphere needs 4 contacts. In recent years, packings of disordered disks and spheres have been studied close to the so-called *jamming transition*, that is the packing fraction at which a packing *just* reaches mechanical stability. At this point, the sudden appearance of a finite shear stiffness signals a transition between a flowing liquid and a rigid, disordered visco-elastic state.

Properties such as elastic modulus, yield stress and average contact number have been found to scale with packing fraction ϕ scaled by the jamming or random-close-pack packing fraction ϕ_c , see Figure 1.19. In 2D, the elastic modulus, G_0 , and the average number of contacts of a disk, $Z - Z_c$ where $Z_c = 4$, are found to obey square root scaling with $\phi - \phi_c$ [17].

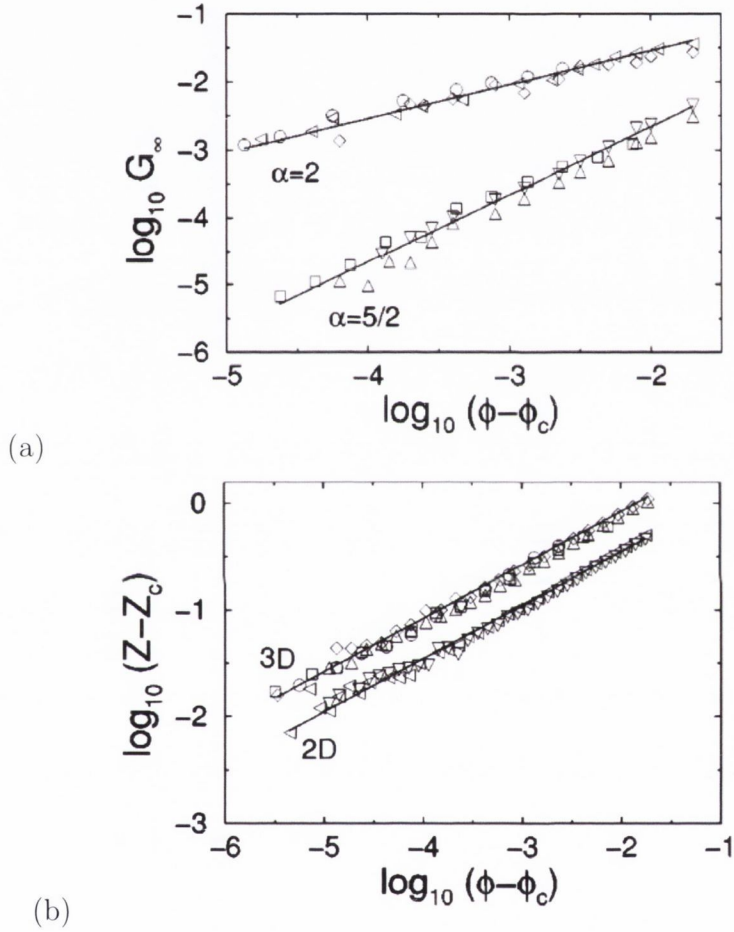


Figure 1.19: **Elastic modulus and contact number close to jamming.** Figure reproduced from [17]. (a) Elastic modulus G_0 versus packing fraction $\phi - \phi_c$, where $\phi_c \approx 0.84$ is the onset of jamming, for a range of polydispersities in 2D and 3D. α denotes the coefficient of elastic repulsion, with $\alpha = 2$ for harmonic repulsion. The solid line for $\alpha = 2$ denotes slope 0.5 on a logscale. (b) Contact number Z minus contact number at jamming transition, Z_c , versus $\phi - \phi_c$. The solid line denotes slope 0.5 on a logscale.

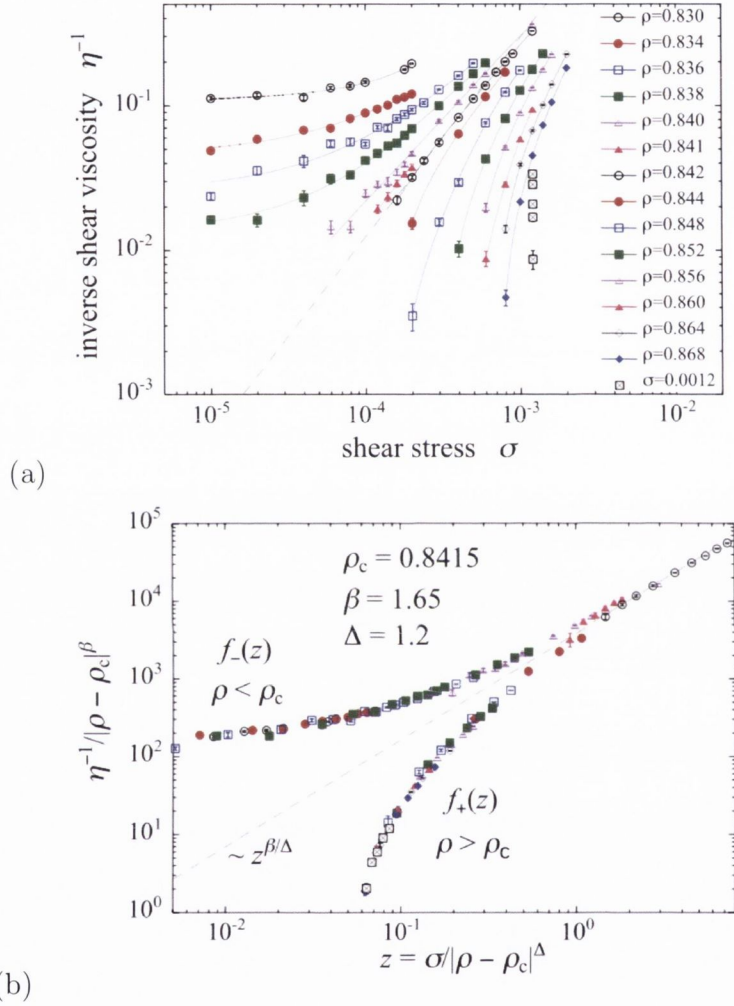


Figure 1.20: **Inverse viscosity versus shear stress in systems near jamming.** (a) Inverse shear viscosity, η , versus shear stress, σ , for a range of packing fractions, ρ , inset, calculated using the soft disk model. (b) Rescaling by the packing fraction minus the packing fraction at jamming, here called $\rho - \rho_c$, collapses the data onto two master curves, $\rho > \rho_c$ and $\rho < \rho_c$. Their scaling exponents, β and Δ , are calculated from the scaling of η with ρ and σ respectively. Figures reproduced from [77].

Static soft disk packings have been extensively studied by O’Hern *et al.* [17, 76], in order to characterise packing behaviours close to the jamming transition and to classify a so-called critical point J for foams, modelled after thermodynamic phase transitions. The structures are calculated by minimising the potential energy of the overlapping disks via conjugate gradient descent. O’Hern *et al.* suggest that the jamming point is “a point of maximal disorder and may control behaviour in its vicinity”. As such, in Chapter 2 we probe packing fractions in our simulations towards, but not below, random close packing, and extrapolate scaling behaviour based on ϕ_c , similar to O’Hern *et al.*

Olsson and Teitel expanded on the work of O’Hern *et al.*, considering dynamic simulations using the soft disk model [77]. Furthermore, they added an additional ingredient to the soft disk model: a uniform shear flow in the event that disks do not touch. This allows the simulation of systems below ϕ_c . They showed that the inverse shear viscosity η^{-1} , where $\eta = \sigma/\dot{\gamma}$ could be rescaled using $\phi - \phi_c$ to collapse onto two master curves, above and below the jamming density ϕ_c , for a range of packing fractions, see Figure 1.20. The scaling strongly suggests that J is a second-order phase transition [77], illustrated in the inset of Figure 1.21.

1.4.4 The Leiden model, in simulations by Tighe *et al.*

Motivated by the work of Olsson and Teitel, and in complement to the experiments of Katgert *et al.*, the Leiden group have recently published a theory connecting the scaling of velocity fluctuations in a foam to the scaling of the viscous shear stress near jamming [79]. A schematic representation of the outcome of their theory is reproduced in Figure 1.21 (a).

Their theory suggests four regimes: a yield stress regime, where Eq (2.4) holds; a transition regime, close to jamming, where the exponent of a Herschel-Bulkley type relation scales with both $n \propto (\phi - \phi_c)^{1/3}$ and $n \propto \dot{\gamma}^{1/3}$; a critical regime with $n \propto \dot{\gamma}^{1/2}$; and finally a viscous regime with $n \propto \dot{\gamma}$.

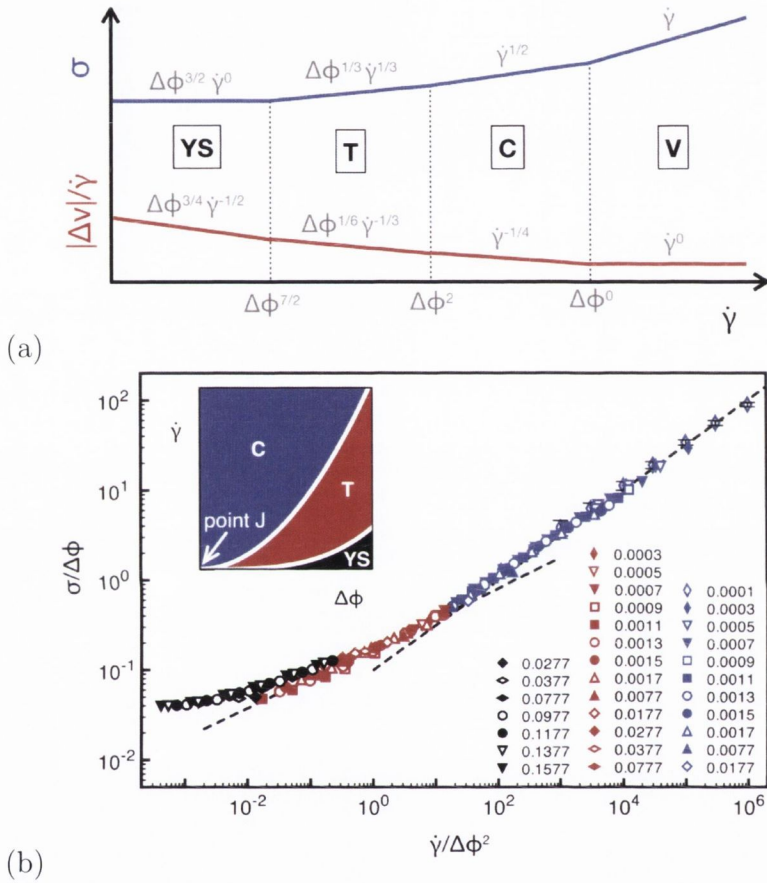


Figure 1.21: **The Leiden model.** Figure reproduced from [79]. (a) Schematic representation of the four regimes of the Leiden model, YS: yield stress, T: transition, C: critical, V: viscous. The blue curve depicts the scaling of the viscous stress, whilst the red curve describes the bubble fluctuations in terms of average velocity divided by strain rate, $|\Delta v|/\dot{\gamma}$, versus $\dot{\gamma}$. $\Delta\phi = \phi - \phi_c$, where ϕ is the packing fraction and ϕ_c the jamming transition. (b) Collapse of the data of Tighe *et al.* for the “transition” and “critical” regimes, for a range of packing fractions and strain rates.

With three flow regimes (excluding the regime below the yield stress), they note that it is impossible to collapse all data onto one curve, showing a collapse and excellent agreement of their simulated data with their theory across a range of strain rates and packing fractions for the “transition” and “critical” regimes (Figure 1.21 (b)) [79].

Tighe *et al.* note that their model could explain the range of values for n found in the literature, based on the range of strain rates an individual experiment examines. It indeed yields a convincing collapse for a range of system parameters, but some questions remain. Despite classifying four regimes, data for only three are presented, with the viscous regime where $\sigma \sim \dot{\gamma}$ omitted. Their derivation requires the disassociation of the elastic and viscous components of the shear stress into dominant regimes, but does not address what (if any) interplay exists between these two quantities during the transient, “critical” regime.

Of interest to us in this thesis is that, beyond the initial power balance assumption that the power supplied $\sigma\dot{\gamma}$ is dissipated by viscous effects $\sim |\Delta v|^2$ - an argument, incidentally, which is again applicable to layers of bubbles sliding past one another in the vein of Schwartz and Princen [56] and Reinelt and Kraynik [58] - their model has no further dependence on the nature of fluctuations with respect to the rheological response. Rather, they show that their model is not inconsistent with distributions of fluctuations, provided that scaling is applied only to the variance of the fluctuation distributions [79] and noting that it does not capture the change in their character, which has been observed in simulation to be rate-dependent [82].

We attempt to link displacements to rheology directly in Chapter 3, and shall look at the time evolution of displacement distributions at short times in Chapter 6. Our motivation for this is tied to the study of “emergence”, a property of complex systems which we shall now introduce.

1.5 Foam as a complex system

The traditional approach of physics in understanding a phenomenon, as noted by Pietronero [83], is to consider the simplest systems and to study them in

great detail. This so-called “reductionist” approach focuses on elementary building blocks and applies, very successfully, in a great deal of physical systems. The existence of these blocks inherently implies a characteristic scale associated with the system: atoms, molecules, or some other macroscopic property.

There are many situations, however, where knowledge of individual elements is not sufficient to characterise the whole system. Such systems, in physics, are called *complex*. In physics, complexity is thus closely related to *emergence*. Emergence refers to often non-linear properties of a system of interacting particles or agents that are not simply inherent in their individual characteristics, or derivable from them by simple averaging procedures. Complexity in physics initially arose in the study of solid state physics, classified in spirit, if not in name, by Anderson [84]. Entitled “More is different”, the paper questions this reductionist approach, arguing that nature is organised in a hierarchical way, with individual elements and collective emergent behaviour every time one moves from one hierarchy to the next.

The study of complexity and complex systems in mathematics, physics, biology and the social sciences has exploded in recent years, facilitated by von Neumann’s prediction that high performance computing would revolutionise non-linear mathematics [85]. Weaire and Hutzler argue that 2D liquid foams, particularly wet foams, are an ideal test-bed for complexity [86]. They feature complex topological rearrangement, non-linear flow profiles, and fractal scaling observed in ageing and evolution [72]. Many of these properties are generic, occurring independent of the foam’s constituents.

Can we then say that a foam is a complex system? As we shall show in this thesis, foams possess many of the traits found for complex systems. Power-law scaling, which we have already seen to emerge in the experiments of Dennin and the simulations of Durian, and fat-tailed, non-Gaussian distributions, like those seen in the experiments of Möbius *et al.* are key components of complex systems.

In addition, complex systems may have some or all of the following features [87]:

- **Complex systems may be open.** Complex systems are usually open, in that they exist in a thermodynamic gradient and dissipate energy. Sheared foams are open systems, with the work done to shear the foam dissipated in viscous interactions. Such systems are usually far from energetic equilibrium.
- **Complex systems may feature cascading failures.** Due to strong coupling between components in complex systems, a failure in one or more components can lead to failures in many others, with a wide ranging effect on the system as a whole [88]. Avalanche-like topological rearrangements are an example of this phenomenon in foams.
- **Complex systems feature non-linear relationships.** In linear systems, the response is always directly proportional to the cause. In complex systems, strongly non-linear coupling can lead small changes to have large effects, proportional effects or even no effect at all. This is sometimes referred to as the *Butterfly Effect*. As we shall see for foams, the non-linear response of the stress with strain rate arises from such coupling.
- **Complex systems relationships can contain feedback loops.** Both negative (damping) and positive (amplifying) feedback are always found in complex systems. The effects of an element's behaviour are fed back to in such a way that the element itself is altered.
- **Complex systems may exhibit memory or hysteresis.** We shall see that foams possess long-memory correlations, with the state of the system at a given time having a propagative effect on its future state.
- **Complex systems may feature nested or scale-free behaviour.** In fluctuations of shear stress in our foam simulations, we shall observe in the identification of trends that nested trends can be identified on multiple different timescales.

We conclude that a foam is well-described as a complex system. We can frame our discussion of foam properties in the context of Anderson's hierar-

chies, by considering the two general scales in our system: the **microscopic** local rearrangements and interactions between neighbouring bubbles, and the **macroscopic** global or bulk response of the system.

1.6 Conclusions and Outlook

In this chapter, we have introduced foams as a material and as a complex system. We have introduced rheology, and outlined the system that we shall study in simulation in an effort to link foam rheology to the complex dynamics at the bubble scale. Finally, we have given a brief overview of some of the experiments and simulations we shall make reference to throughout this thesis.

We now look forward. In Chapter 2, we shall rigorously define the simulation we study, and we shall investigate the macroscopic rheology that emerges from our model, comparing it to experimental and simulation results for foams, emulsions and granular media. This will provide a framework for the investigation of the origins of this rheology, in subsequent chapters.

Chapter 2

Macroscopic Rheology in Soft Disk Simulations

The first step in understanding any physical system is to express its key traits as simply as possible. This philosophy is encapsulated by computer simulation. In simulation, we attempt to model complex physical processes using a minimal set of basic ingredients and assumptions, in order to determine the dependencies of the physical system.

In this thesis, we wish to investigate the relationship between the non-linear response of a foam under shear and the interactions at the bubble scale. To do this, we utilise computer simulations, modelling the foam as a packing of overlapping disks. We shall see that, despite our model being governed by two simple, linear interaction forces, a rich, non-linear rheology emerges.

In this chapter, we shall define in detail the simulation model we use to investigate the flow properties of wet foams, namely the soft disk model introduced in Section 1.4.1. We then present results from the model for the scaling of the shear and normal stresses with strain rate and packing fraction. We find excellent agreement between our simulated rheology and experimental results for foams, providing us with a solid framework for the investigation of the origin of this macroscopic rheology at the microscopic level.

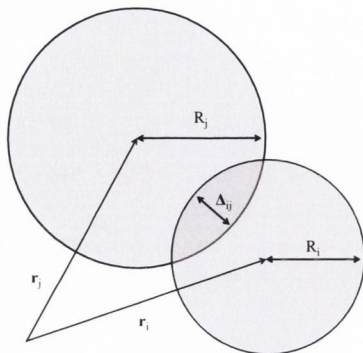


Figure 2.1: **Schematic of bubble-bubble interaction**, for overlapping bubbles i and j , described by position vectors \mathbf{r}_i and \mathbf{r}_j respectively.

2.1 The soft disk model

We perform simulations using the soft disk model, first developed by Durian [36, 51], as implemented by Langlois *et al.* [52]. The model is widely used in foam rheology, and has been shown to capture many of the key features of liquid foams found in experiment. In this section, we define the implementation of the model used for this thesis, in terms of its governing forces, parameters and geometry. A further discussion of the technical implementation of serial and parallelised computer code is included in Appendix A.

2.1.1 Interaction forces

The soft disk model represents a 2D foam as a series of overlapping disks, confined in some geometry. The disks are subject to two types of forces when they overlap. The first is a simple spring force, where the displacement of the spring corresponds to the radial overlap of the disks. The resulting elastic repulsive force \mathbf{F}_e acting on bubble i due to bubble j is given by:

$$\mathbf{F}_e = \kappa \frac{2R_0}{R_i + R_j} \Delta_{ij} \mathbf{n}_{ij}, \quad (2.1)$$

where κ is the coefficient of elasticity, \mathbf{n}_{ij} is the normal vector between bubbles i and j ,

$$\mathbf{n}_{ij} = \frac{\mathbf{r}_i - \mathbf{r}_j}{|\mathbf{r}_i - \mathbf{r}_j|}, \quad (2.2)$$

and the overlap Δ_{ij} is given by:

$$\Delta_{ij} = \begin{cases} (R_i + R_j) - |\mathbf{r}_i - \mathbf{r}_j| & \text{if } (R_i + R_j) < |\mathbf{r}_i - \mathbf{r}_j|. \\ 0 & \text{otherwise} \end{cases} \quad (2.3)$$

R_i and R_j are the radii of overlapping bubbles i and j , centered at \mathbf{r}_i and \mathbf{r}_j respectively, shown schematically in Figure 2.1. R_0 is the average bubble radius of the entire packing. The ratio $\frac{2R_0}{R_i + R_j}$ in Equation (2.1) takes into account that larger bubbles are easier to deform than smaller bubbles. For our simulations, we use a linear, Hookean repulsion between the disks, directly proportional to their overlaps. Experiments by Lacasse *et al.*, introduced in Section 1.3.2, have shown that this is a good approximation to the force exerted by spherical bubbles in contact, provided the deformation is small [59].

In addition to the repulsion the bubbles are subject to a viscous drag force when they are in contact,

$$\mathbf{F}_d = -c_d(\mathbf{v}_i - \mathbf{v}_j). \quad (2.4)$$

Here c_d is the dissipation constant for bubble-bubble interaction, and \mathbf{v}_i and \mathbf{v}_j are the respective bubble velocities. Thus the dissipative force is directly proportional to the bubbles' relative velocity.

As mentioned in Section 1.4.1, early simulations of the Durian model used a mean-field approximation for the viscous dissipation experience by the bubbles [36, 51, 77, 81], motivated by the reduction in computational intensiveness. The drag force was taken to be directly proportional to the mean flow velocity, assumed to be linear, as a function of channel width. Following the work of Langlois *et al.* and others, we do not use the mean

field approximation for the viscous dissipation as it has recently been shown to cause spurious correlations [79].

As in previous simulations on foam flow [51, 52, 79], we impose the drag force to be linear to the relative bubble velocity. This is an approximation, in the interest of retaining a simple model using linear forces. We shall return to a discussion of this approximation in Section 3.1. The model also neglects any dissipation due to the stretching of the films [21]. Furthermore, the model contains no equivalent of the attractive capillary force normally found in wet foams, instead relying on the system to be constrained by its geometry.

2.1.2 System geometry

The simulated systems comprise of bubbles, represented by circular disks, that are confined in a rectangular geometry with semi-periodic boundary conditions in the horizontal direction. The bubbles at the lower boundary have their positions fixed and are stationary. The bubbles at the upper boundary have their y coordinates fixed, and are given a constant velocity V in the x direction. This corresponds to a constant applied strain rate of $\dot{\gamma} = V/L$ to the entire system, where L is the width of the channel as depicted in Figure 2.2.

We have simulated systems ranging from tens of disks, up to packings of 12000 disks. For the purposes of our analysis, the system size we consider (unless otherwise specified) consists of 1500 bubbles in the bulk, 80 bubbles in the walls and a channel width of $L = 33\langle d \rangle$, where $\langle d \rangle$ is the average disk diameter. In Chapter 4 we investigate the effect of varying the system dimensions.

The distribution of disk sizes is known as the *dispersity* of the sample. A sample containing disks that are all the same size is *monodisperse*. In all of the results presented, we consider disordered, *polydisperse* samples, with the disk radii uniformly distributed in the range

$$R = R_0(1 \pm 0.3), \quad (2.5)$$

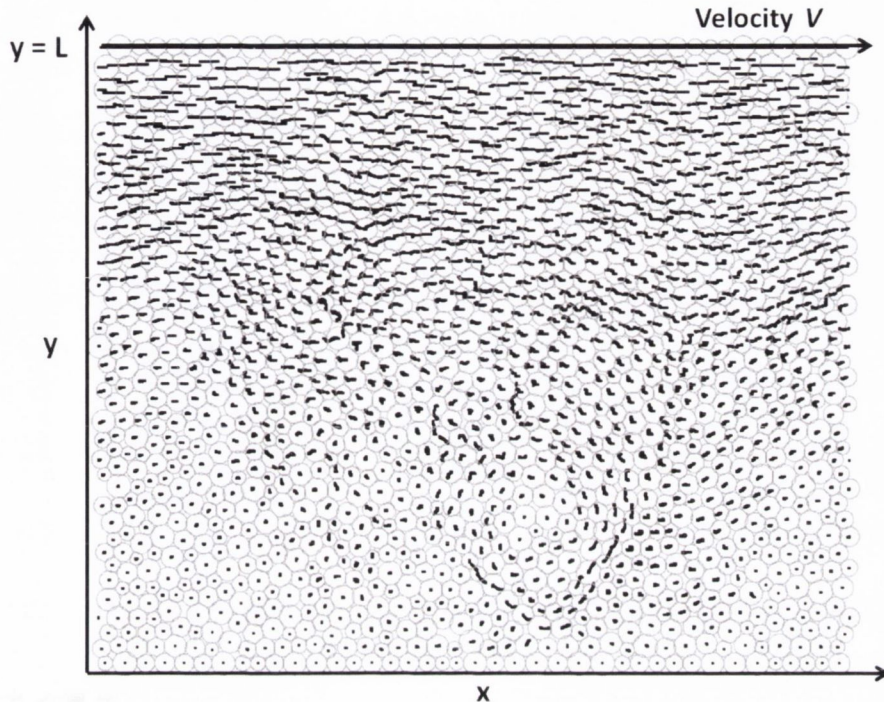


Figure 2.2: **Bubble trajectories of a linearly sheared foam, for a low strain rate.** Black trails represent the positions of the bubble centres during a total strain of $\Delta\gamma = 0.04$. Swirls in the bubble trajectories indicate strongly non-affine displacement fluctuations.

where R_0 is the average bubble radius, set as a simulation parameter. Polydisperse samples are studied in order to avoid crystallisation effects, which are well known to occur for monodisperse foams [7, 89].

In the soft disk model, the packing fraction, ϕ , is defined as

$$\phi = \frac{1}{A} \sum_i^N (d_i/2)^2 \pi, \quad (2.6)$$

where N is the total number of disks, A is their area of confinement and d_i is the diameter of disk i . The disks are randomly placed and A gradually reduced until the desired packing fraction is achieved. In our simulations, we consider a range of packing fractions above the jamming transition in 2D of $\phi_c \approx 0.84$ [17].

When comparing the packing fraction in soft disk model simulation results to the liquid fraction measured in experimental results, it is important to note that they are not quite equivalent. The above definition for packing fraction, whilst being widely-used and accepted, double-counts overlaps between disks to return artificially high values. For instance, it is possible to define a simulation packing fraction greater than 1.0, which is not possible in a physical system. We discuss this discrepancy and possible corrections in Appendix B. For the purposes of presenting our results in this thesis, we use packing fraction as defined by Equation (2.6).

2.1.3 Strain rate, characteristic timescales and Deborah number

As discussed in the previous section, the strain rate $\dot{\gamma}$ is imposed by the moving boundary, such that $\dot{\gamma} = V/L$. We then allow the resulting elastic and viscous dissipative forces, caused by the motion of the wall, to propagate through the system. Each bubble is allowed to move independently subject to the forces in Equations (2.1) and (2.4), with the respective position and velocity resolved at each simulation time step using the Verlet algorithm. We define this algorithm in Appendix C. Following a transient regime, a steady state, linear velocity profile is established, see Figure 2.3.

As a type of molecular dynamics simulation, timescales play an important role in the properties of the soft disk model. We will briefly discuss three relevant timescales here, namely the *inertial* and *viscous* timescales, and the characteristic timescale of the deformation process.

The inertial timescale, a measure of the characteristic time of the motion of disks with respect to their masses and inertias, is given by

$$\tau_i = m_b/c_d, \quad (2.7)$$

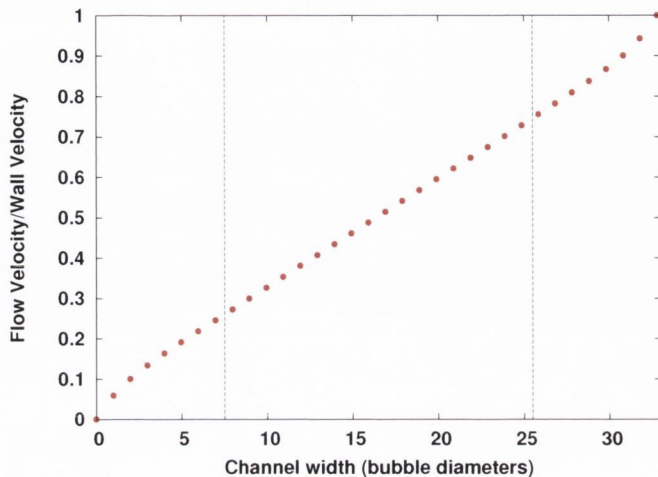


Figure 2.3: **A typical velocity profile for the steady state flow in a soft disk model simulation.** Here, the velocity profile has been averaged over a strain of $\gamma = 375$, in the steady-state flow. We consider the region between the vertical dashed lines as within the bulk flow, away from the effects of the boundaries, for analysis performed in Chapter 3.

where m_b is the average mass of a bubble and c_d is the coefficient of viscous dissipation defined in Equation (2.4). The viscous timescale, related to the rate of dissipation of energy due to drag, is defined as

$$\tau_v = c_d/\kappa, \quad (2.8)$$

where κ is the coefficient of elastic repulsion from Equation (2.1). Finally, the characteristic time of the deformation process is simply the inverse of the strain rate, $\dot{\gamma}^{-1}$.

In order to accurately model the physical system, where bubbles are essentially massless, we ensure that inertia is negligible in the system, i.e. that the dynamics in the system are overdamped. This is achieved by choosing a very small ratio of the inertial timescale to the viscous timescale. In our simulations the ratio τ_i/τ_v is set to $\tau_i/\tau_v = \kappa m_b/c_d^2 = 0.015$.

It is convenient, for a dimensionless presentation of the results, to introduce the *Deborah number*, De , which is defined as the ratio of the characteristic time of the material that is sheared to the characteristic time of the

deformation process $\dot{\gamma}^{-1}$. Since inertia is negligible in our simulation, the characteristic time scale for the foam is $\sim c_d/\kappa$ and we have

$$De = \dot{\gamma}c_d/\kappa. \quad (2.9)$$

In order to accurately resolve the motion of the disks in simulation, the timestep used to perform the Verlet calculations should be much shorter than the shortest timescale in the system. This has the effect that for high strain rates, the simulation timestep must be reduced, as the inverse strain rate rapidly becomes the shortest timescale in the system. We list the time resolutions used in Appendix D.

2.1.4 Stress and the elastic modulus

We calculate the stress in the system due to shear by summing the forces acting on the boundaries. The two-dimensional shear stress σ is measured by taking the sum of the forces along the x direction that act on the boundary bubbles, divided by the length of the channel, at each output time step. Analogously, the normal stress Π is found by summing the forces on the boundary bubbles along the y direction. The stresses are measured on both boundaries.

As introduced in Section 1.2, and depicted schematically in Figure 1.4, for low strains, below some *yield strain* γ_Y , the foam deforms elastically, as described by Equation (1.9). After the stress exceeds the *yield stress*, σ_Y , the foam yields and begins to flow.

We measure the static shear modulus G_0 from the stress-strain curves averaged over multiple different realisations for each value of packing fraction ϕ . Each realisation is allowed to relax to mechanical equilibrium, before being sheared at a very low strain rate. For small strains (less than the yield strain of a few percent) the deformation is approximately linear in strain such that $\sigma = G_0\gamma$, see Figure 2.4 (a). We non-dimensionalise our results for

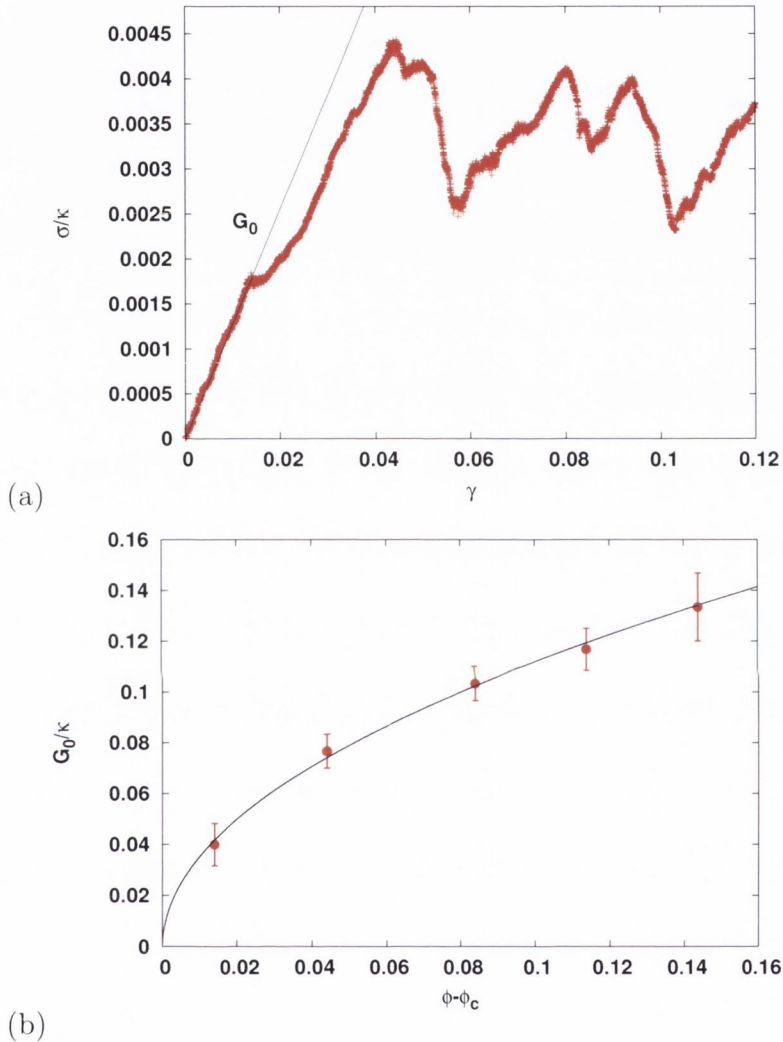


Figure 2.4: **The elastic modulus, G_0 .** (a) Stress, normalised by the coefficient of elastic repulsion κ from Equation (2.1), versus strain, for a very low strain rate simulation. This sample has been relaxed to mechanical equilibrium before being sheared. The solid line marks the value of G_0 calculated for this packing. (b) G_0/κ plotted as a function of packing fraction ϕ . The solid line plots a two-parameter fit to the power law relation $G_0 \propto (\phi - \phi_c)^{0.5}$, where ϕ_c is the jamming point. We find $\phi_c = 0.84$, in good agreement with the literature for 2D foams [17]. This relation has been found to hold for foams with harmonic interaction in both 2D and 3D simulations [17].

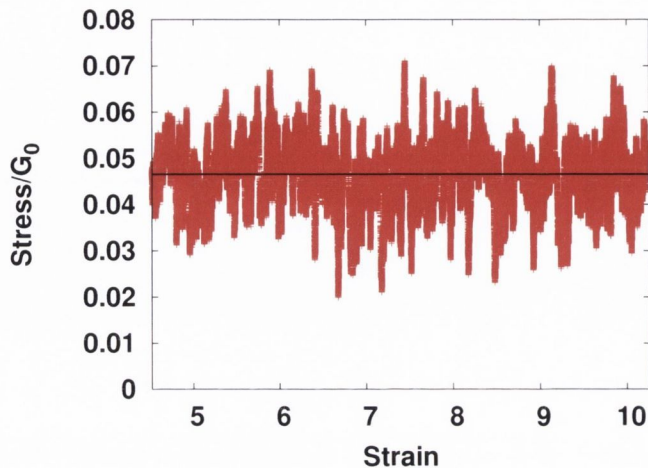


Figure 2.5: **Shear stress versus strain.** Shear stress, normalised by the elastic modulus G_0 , versus strain, for $De = 7.56 \times 10^{-6}$ and $\phi = 0.95$. The stress oscillates about the mean, which we calculate from the data and which is shown here by the horizontal black line.

stress using the appropriate value of G_0 for the simulation, which varies as a function of packing fraction, Figure 2.4 (b), via

$$G_0 \propto (\phi - \phi_c)^{0.5\alpha} \quad (2.10)$$

where ϕ_c is the jamming transition, and α is the exponent of repulsive interaction - in our case $\alpha = 1$, for harmonic interactions [3].

After an initial transient regime, the foam reaches a steady-state flow, with the stress fluctuating about a mean value which is independent of time. Figure 2.5 shows a typical example of shear stress versus strain for steady state flow, with $De = 7.56 \times 10^{-6}$. The black horizontal line delineates the average shear stress calculated from the data. We calculate the mean stresses in the steady state flow, for high strains far beyond the yield strain.

We now use these results to investigate two relations: the Herschel-Bulkley equation (Equation (1.10)), and the model put forward by Jop *et al.* [32] introduced in Section 1.3.6.

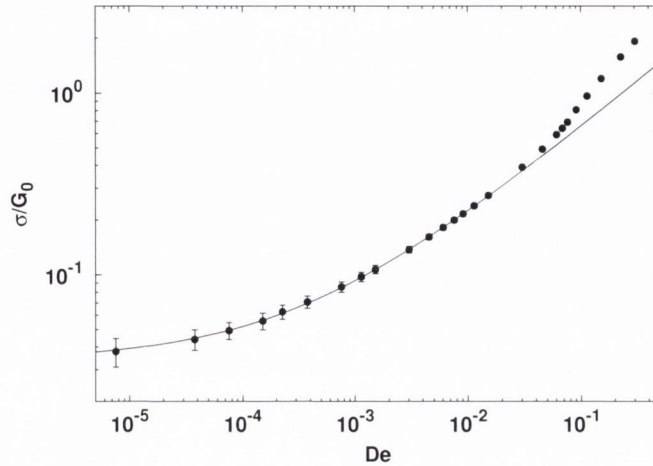


Figure 2.6: **Shear stress versus Deborah number.** The normalised shear stress σ/G_0 versus close to five decades of Deborah number, for $\phi = 0.95$. The black line is a fit to the Herschel-Bulkley equation (1.10) up to $De = 2.0 \times 10^{-2}$, with $n = 0.51 \pm 0.01$, $\sigma_Y = (3.4 \pm 0.1) \times 10^{-2}G_0$ and $c_v = (2.04 \pm 0.04)G_0(c_d/\kappa)^n$. The Herschel-Bulkley equation is found to inadequately describe the data for high strain rates. We return to this in Chapter 3.

2.2 The Herschel-Bulkley relation for packings of different densities

As introduced in Chapter 1.2, the Herschel-Bulkley equation (1.10) is an empirical relation that has been found to describe well the flow of foams and other non-Newtonian fluids.

Figure 2.6 shows average shear stress σ , normalised by G_0 , plotted as a function of Deborah number (which is simply the non-dimensionalised strain rate $\dot{\gamma}$, see Equation 2.9), for a packing fraction of $\phi = 0.95$. The range of these simulations covers nearly five decades of strain rate. This range poses several technical challenges, discussed in more detail Appendix D. We do not probe Deborah numbers beyond $De \approx 0.5$. At this point, voids start to appear in the sheared foam (see Figure D.1). This is a known limitation of

the soft disk model and is ascribed to the simplification of the model that non-overlapping disks do not experience viscous interactions [90].

The Herschel-Bulkley relation is found to describe the flow profile well for low strain rates, yielding an exponent of $n = 0.51 \pm 0.01$ for $\phi = 0.95$, in agreement with the range of experimental results observed [21, 22, 27]. However, as the strain rate increases the relation is found to no longer hold. We shall discuss this in more detail in Chapter 3. For now, we shall focus on the dependence of the yield stress σ_Y and the Herschel-Bulkley exponent n with packing fraction ϕ , for the regime which we shall refer to as the ‘‘Herschel-Bulkley regime’’.

Figure 2.7 plots the shear and normal stresses as a function of Deborah number, for five different packing fractions, $\phi \in \{0.85, 0.88, 0.92, 0.95, 0.98\}$. These values of shear stress σ and normal stress Π have been normalised by the appropriate value of $G_0(\phi)$, see Figure 2.4 (b). For comparison, the axes and symbols in both plots are identical. The black circles in Fig 2.7 (a) are identical to those in Figure 2.6.

The solid lines in Fig 2.7 (a) show fits to the Herschel-Bulkley equation (1.10), $\sigma = \sigma_Y + c_v \dot{\gamma}^n$, over the range $5 \times 10^{-6} < De < 2 \times 10^{-2}$. For higher values of De , we once again find that the Herschel-Bulkley equation fits the data poorly. Again, we postpone discussion of this regime until Chapter 3, and shall instead focus on the low strain rate regime where we observe the Herschel-Bulkley equation to well describe the flow properties.

In Figure 2.8, we plot the yield stress σ_Y and exponent n , taken from the fits in Figure 2.7 (a), as a function of $\phi - \phi_c$. We use $\phi_c = 0.84$, from our fit in Figure 2.4 (b) and in agreement with the literature [17].

It has been found that, for foams and emulsions in 3D, the yield stress scales with packing fraction [3, 37], via

$$\sigma_Y = \frac{S}{R_0} (\phi - \phi_c)^{0.5}, \quad (2.11)$$

for packing fractions in the range $0.7 \lesssim \phi \lesssim 0.95$. At lower values of ϕ , Saint-Jalmes *et al.* attributed deviation from this square root scaling to

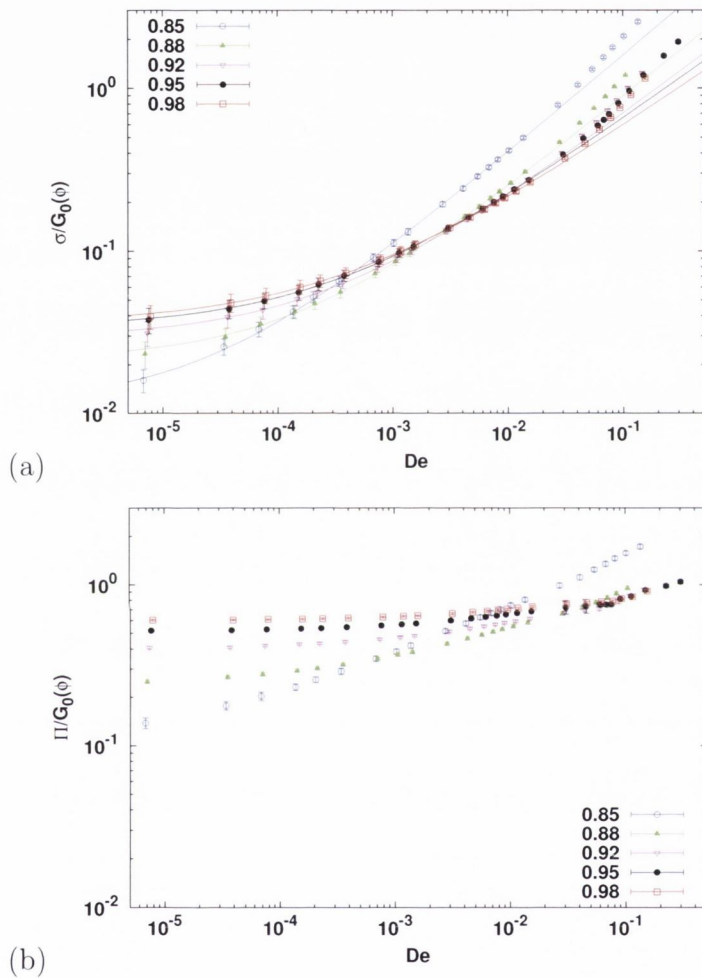


Figure 2.7: **Shear and normal stress as a function of packing fraction.** (a) Shear stress σ , normalised by $G_0(\phi)$, versus De for five values of packing fraction: $\phi = 0.85$, (\circ); $\phi = 0.88$, (\blacktriangle); $\phi = 0.92$, (∇); $\phi = 0.95$, (\bullet); $\phi = 0.98$, (\square). The solid lines show fits to the Herschel-Bulkley equation (1.10) up to $De = 2.0 \times 10^{-2}$. Once again, for all packing fractions the Herschel-Bulkley equation is found to fit poorly as one approaches high strain rate. (b) Normal stress Π , normalised by $G_0(\phi)$, versus De .

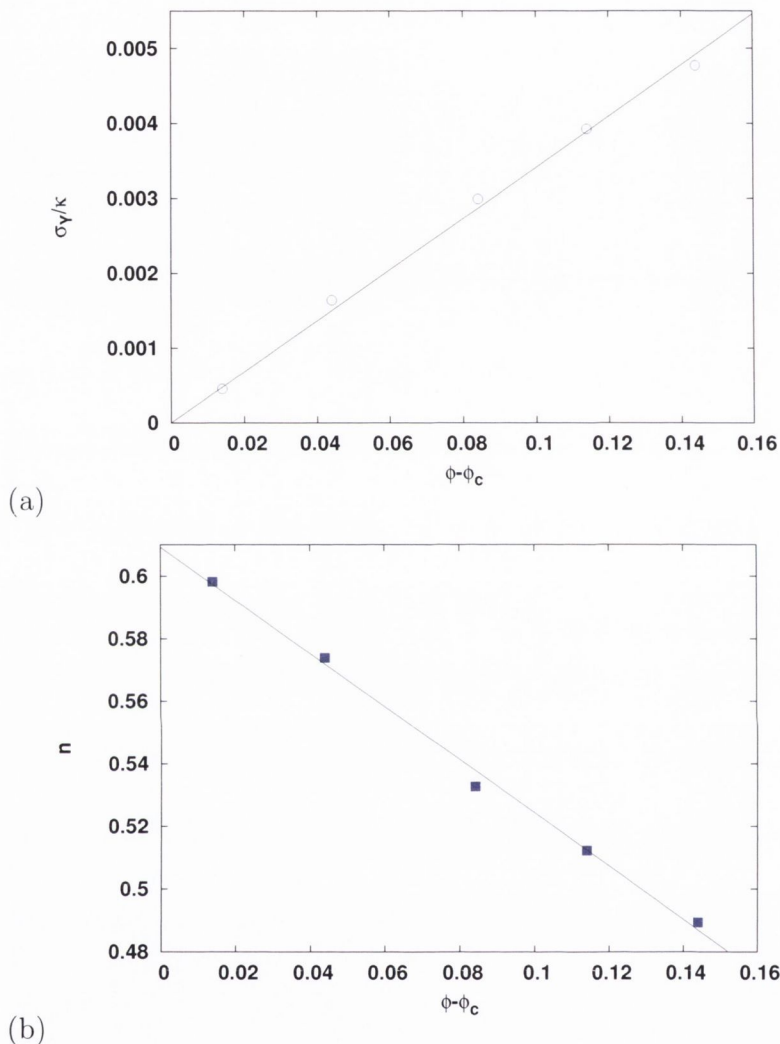


Figure 2.8: **Yield stress and Herschel-Bulkley exponent versus packing fraction.** (a) σ_Y/κ , versus $\phi - \phi_c$. The solid line shows a one-parameter fit $f(x) = mx$, with $m = 0.033 \pm 0.003$. In experiment, yield stress in foams and emulsions is found to be approximately linear at low packing fraction, in qualitative agreement with our findings [13, 33]. The yield stress then rapidly increases for dry foams at high packing fraction (or low liquid fraction). We remind the reader that our values for ϕ ranging up to $\phi = 0.98$ are higher than their equivalent experimental gas fraction, see Appendix B. (b) Herschel-Bulkley exponent, n , versus $\phi - \phi_c$. The solid line plots a linear regression fit, $f(x) = -0.85(\pm 0.03)x + 0.606(\pm 0.003)$. All values lie within the range reported in experiment [21–29].

rapid drainage of the wet foams making measured values of packing fraction unreliable [37].

In contrast, we find σ_Y to increase approximately linearly with ϕ for 2D, shown in Figure 2.8 (a). Quasistatic simulation results in 2D have found that, for wet foams, the yield stress initially increases linearly with packing fraction. As the foam approaches the dry limit, the yield stress then dramatically increases [13, 38].

This behaviour is not surprising: for an increased packing fraction, the foam gains more rigidity and more elasticity. In the limit of $\phi \rightarrow \phi_c$, the foam (in general) loses mechanical stability (below random close pack), and the yield stress falls to zero. We do not observe a rapid increase in yield stress as we reach higher packing fraction. The linear trend continues even for $\phi = 1.05, 1.10$, not presented here. We attribute this to the soft disk model, ultimately, being a model appropriate for **wet** foams. The model makes no attempt to capture the physical behaviour of dry foams as the liquid fraction tends to zero, where the bubbles are no longer well represented by disks. Our results compare well with quasistatic simulation results for low ϕ , provided one accounts for effective packing fractions our values of ϕ represent (see Appendix B). Comparing with experiments in 2D is more difficult, as it is not straightforward to define a liquid fraction for a 2D foam either trapped between two plates, or in contact with a liquid reservoir (see Figure 1.5).

In Figure 2.8 (b), we see that the Herschel-Bulkley exponents calculated scale inversely proportional to $\phi - \phi_c$. All values for n measured fall within the range reported in experiment and simulation [21–29]. To our knowledge this is the first time the Herschel-Bulkley exponent has been calculated as a function of packing fraction, using the soft disk model. The closest comparable study is that of Tighe *et al.* [79]. Their model expects that the exponent should scale independent of packing fraction within their critical regime, and should increase with packing fraction within their transient regime, see Figure 1.21 (a). Our results do not agree with their model, for the range in which we have fitted the equation. We note that our values fall within the range $n = 0.5 \pm 0.1$, close to their expected exponent for the critical regime, and also that the model of Tighe *et al.* concerns only the elastic component

of the shear stress. A weak dependence of the viscous component of the shear stress on the packing fraction could perhaps explain the discrepancy.

2.3 A constitutive model of foam rheology

In this section, we apply a modified version of the constitutive law of Jop, Forterre and Pouliquen [32], developed as a continuum model for dense granular flows, to foam flow data. This is the first time this has been done for foam data in simulation. We find that their model provides a good collapse of the data presented in Section 2.2, for all packing fractions, and find our data to agree well with comparable experiments of Lespiat *et al.* in 3D [30].

2.3.1 Origin of the model for granular media

The constitutive model builds on work showing that, for granular flows, the shear stress σ is proportional to the normal stress Π , via a coefficient of proportionality $\mu(I)$:

$$\sigma = \mu(I)\Pi. \quad (2.12)$$

I is a dimensionless parameter, called the *inertial number* for granular media, given by

$$I_{\text{gran}} = \frac{\dot{\gamma}d}{(\Pi/\rho_s)^{0.5}}, \quad (2.13)$$

where d is the average particle diameter, and ρ_s the coefficient of static friction. For granular systems, I can be interpreted as the ratio between two timescales: the characteristic timescale of deformation $1/\dot{\gamma}$, and an inertial timescale $(d^2\rho_s/\Pi)^{0.5}$ [32].

2.3.2 Adapting the model for foams

For foams, and in our simulations, the inertial timescale is negligible, as discussed in Section 2.1.3. Furthermore, there is no static friction. Motivated

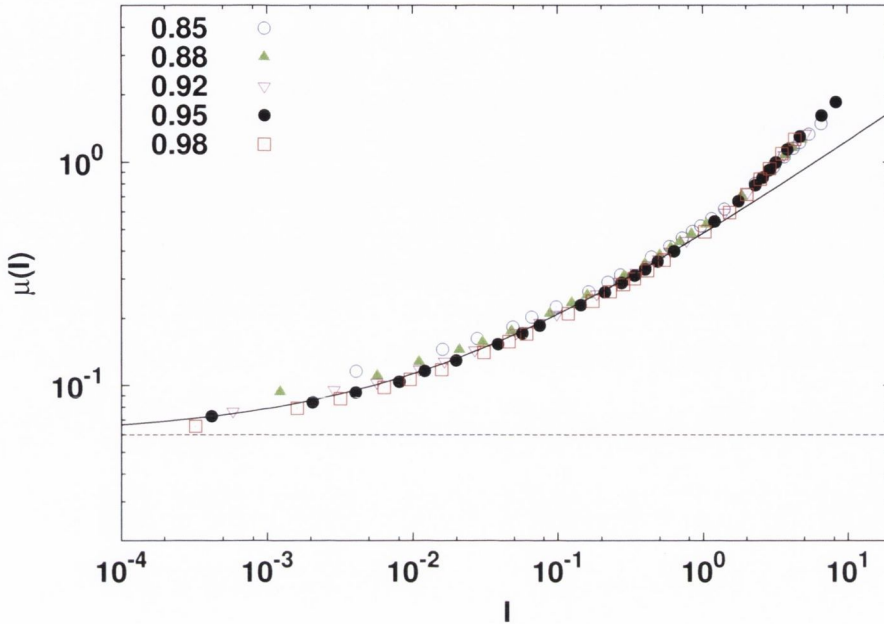


Figure 2.9: **Constitutive model collapse for five packing fractions.** $\mu(I) = \sigma/\Pi$ versus I , for five packing fractions over nearly five decades of strain rate. Data and symbols identical to Figure 2.7. The solid line plots the fit to Equation (2.15) over the same range as our Herschel-Bulkley fits (Section 2.2), with $\mu^* = 0.060 \pm 0.002$ (shown also as the asymptotic limit for zero strain rate by the horizontal dashed line), $k = 0.42 \pm 0.02$ and exponent $a = 0.45 \pm 0.02$. Although the data collapses in the high strain rate regime, it is no longer well described by the empirical scaling for I from Equation (2.15).

by these differences, we instead use the *viscous* timescale, c_d/Π , where c_d is the coefficient of viscous drag from Equation (2.4). This yields

$$I = \frac{c_d \dot{\gamma}}{\Pi}. \quad (2.14)$$

In Figure 2.9, we rescale the data from Figure 2.7, plotting $\mu(I) = \sigma/\Pi$, also called the *coefficient of viscous friction*, versus I for five different packing fractions, $\phi \in \{0.85, 0.88, 0.92, 0.95, 0.98\}$, over nearly five decades of strain rate. The data collapses remarkably well for all packing fractions and strain rates.

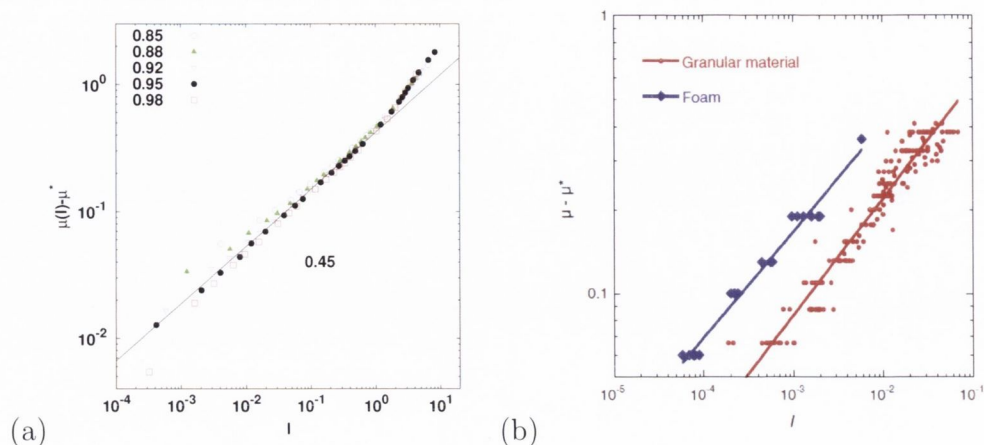


Figure 2.10: **Comparison of coefficient of viscous friction in simulation and experiment.** (a) $\mu(I) - \mu^*$ versus I , for our simulations. μ^* is calculated from the fit to the data in Figure 2.9. The solid line, with a log-log scale, shows the power-law scaling $a = 0.45 \pm 0.02$. (b) $\mu(I) - \mu^*$ versus I , for the experiments of Lespiat *et al.* [30]. Our results compare favourably to their result of $a = 0.38$, for foams (blue) and immersed granular material (red) in 3D.

We find $\mu(I)$ is well fit by the empirical functional form

$$\mu(I) = \mu^* + kI^a, \quad (2.15)$$

where μ^* is the static value for ratio of shear to normal stresses, i.e. $\mu = \mu^*$ when $\dot{\gamma} = 0$, k is a proportionality coefficient, and a is a scaling exponent. The solid line in Figure 2.9 plots the fit to Equation (2.15) over the same range as our Herschel-Bulkley fits (Section 2.2), with $\mu^* = 0.060 \pm 0.002$ (shown also as the asymptotic limit for zero strain rate by the horizontal dashed line), $k = 0.42 \pm 0.02$ and $a = 0.45 \pm 0.02$. Although the data collapses in the high strain rate regime, it is no longer well described by the empirical scaling for I from Equation (2.15). We attribute this to a change in the flow behaviour in this regime, which we discuss in Chapter 3.

Figure 2.10 (a) replots our data in the form $\mu(I) - \mu^*$ versus I . Comparing our results with the experiments of Lespiat *et al.*, we find good agreement.

For 3D foams subjected to linear shear, they find $\mu(I) - \mu^* \propto I^{0.38}$, shown in Figure 2.10 (b) reproduced from [30].

2.3.3 The angle of repose

The *static angle of repose* is the angle a pile of grains at rest on a plane makes with that plane, see Figure 2.11 (a). The angle of repose for sand, for instance, is visible on a large scale in arrays of sand dunes, whose downwind faces tend to have slopes close to the angle of repose for dry sand of about $30^\circ - 34^\circ$ [91]. For granular media, this angle is related to the coefficient of static friction $\mu_s = \sigma/\Pi$ [67]. This friction opposes the sliding motion of grains down a pile as more grains are added.

For foams, where the bubbles are essentially massless, we instead look at piles formed by bubbles rising under the effect of buoyancy and coming to rest against a plane. Such wet foams are observed to have a static angle of repose, in planar and circular geometries (Figure 2.11 (b)) in experiment [30] and simulation [92], even in the absence of static friction.

At zero strain rate, $\mu(I) = \mu^*$, and Equation (2.12) returns the static angle of repose α , where

$$\alpha = \tan^{-1} \frac{\sigma}{\Pi} = \tan^{-1} \mu^*. \quad (2.16)$$

From our data, we can compute a static angle of repose for foams. We find $\alpha = 3.4 \pm 0.2^\circ$. In a 3D linear geometry, Lespiat *et al.* find a value of $4.6 \pm 1.0^\circ$ in experiment [30], whilst Peyneau *et. al* find $5.76 \pm 0.22^\circ$ for simulations [92]. In experiments and simulations using the 2D rotating drum geometry featured in Figure 2.11, our group find a value of $4.8 \pm 0.5^\circ$ [93]. The slightly lower value we obtain from our soft disk model simulations compared to other values might be caused by the effects of different system geometries. We return to this discussion of the angle of repose in Section 4.2.1.

Our results, showing that a constitutive law developed for dense granular flows also describes the flow of foams in simulation, provide further support for the analogy of foams as granular media.

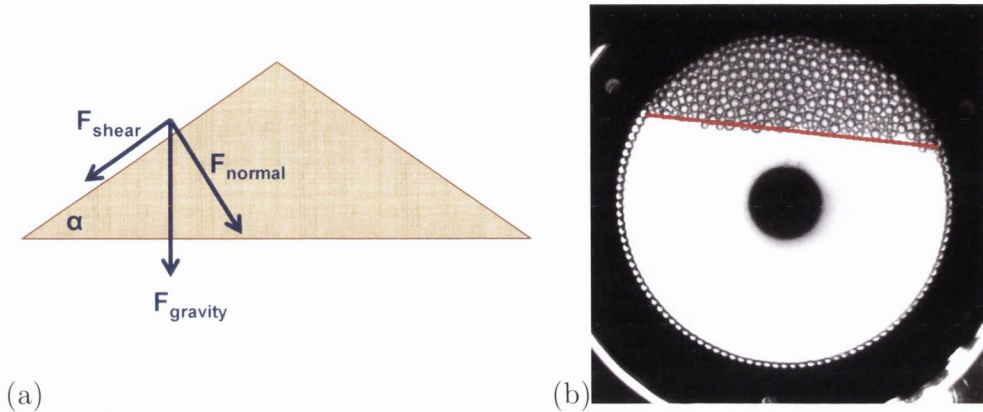


Figure 2.11: **The angle of repose.** (a) Schematic representation of the angle of repose α . In this schematic gravity is acting downwards, and the shear and normal stresses generated by the particles' weight. The balance between normal and shear stresses controls α , via $\tan \alpha = F_{\text{Shear}}/F_{\text{Normal}} = \sigma/\Pi$. (b) The static angle of repose of a wet, 2D foam in a rotating drum geometry. For foams, where the bubbles are essentially massless, the buoyancy plays the role of weight. After having been subject to oscillatory motion in the drum, the foam comes to rest at a non-zero angle of repose, shown by the red line. Photograph courtesy of V. Poulichet.

2.4 Conclusions and Outlook

The soft disk model, which we have defined in this chapter and which we shall use extensively in this thesis, has been seen to accurately capture many of the key features of bulk wet foam rheology. It captures the visco-elasticity of the medium, with a yield stress scaling with packing fraction in agreement with experiment, in the wet limit. It reproduces the non-linear scaling of stress with strain rate empirically described by the Herschel-Bulkley equation, with exponents in the range of values reported in the experimental literature. Furthermore, we have shown that it captures scaling of the macroscopic friction coefficient $\mu(I)$ with dimensionless strain rate I . This constitutive model was first shown to hold by Jop *et al.* for granular media in experiment,

and later by Lespiat *et al.* for foams in 3D experiments. Here, we have shown for the first time that this scaling is also found in 2D foam simulations.

All of these results are important, in the overall context of this thesis. We aim to study the complex dynamics in the flow of foams, and in this respect simple models such as the soft disk model are crucial. Unlike the more challenging experimental equivalents, in these models it is easy to track the dynamics, and to obtain good statistics over many decades of variation. Large volumes of high-quality data are vital in the study of complex systems, where one often relies on statistical measures. The soft disk model accurately captures these quintessential features of foam flow, strongly validating it as an appropriate model of how bubble-scale interactions propagate. This makes it an ideal tool for attempting to understand complexity in foams.

Chapter 3

Microscopic Dynamics, Relaxation and Flow

In the previous chapter, we have defined the simulation model utilised to study 2D foam rheology, and we have shown that it captures the strongly non-linear, visco-elastic behaviour known for foams from experiments. At a local level, the model is extremely simple, where interacting bubbles are governed by two linear forces. Yet, from the aggregation of these interactions throughout the system, we see a rich landscape of complex dynamics emerging.

It is from these complex dynamics that the non-linear response, often described by the Herschel-Bulkley equation, originates. Ultimately, the shear-thinning rheology originates from dissipative bubble rearrangements that relax transient elastic stresses and from non-linear viscous dissipation between bubbles. The main aim of this thesis is to find meaningful ways of relating the complex dynamics at the bubble scale to the rheology of foams. In this chapter, we shall look at fluctuations in bubble displacements during shear, and relate these to the shear stress via a deformation-relaxation argument which has been used to calculate the viscosities of Newtonian fluids [94].

The link between the shear-induced dynamics on the bubble scale and the resulting non-linear bulk response is not entirely resolved. Moreover, the validity of the Herschel-Bulkley relation itself has been called into question [79].

Previous work on the relation between bubble motion and bulk stresses in sheared foams has often focused on the extremes of low or high shear rate regime. For the latter, models [21] based on Princen's work [53] have been proposed that assume an ordered foam structure that flows along the crystal planes. For low shear rates, deformation-relaxation type models [29, 79] have been put forward as well as a theory based on fluidity [95], which has been motivated by recent experiments that exhibited non-local rheology in emulsions [31, 96]. However, the transition between these two regimes is not well understood. While it is known from experiments [97] and simulations [81] that the dynamics on the bubble scale undergo a change from intermittent rearrangements to a more laminar-type flow, the corresponding regimes of validity of the rheological models mentioned above is unclear. Furthermore, the mean field approximation used in many foam simulations [36, 51, 77, 81] has recently been shown to differ from simulations without this approximation [79].

We address this issue using our simulations without the mean field approximation, probing the flow over nearly five decades of strain rates. In doing so, we succeed, for the first time in simulations of wet foam rheology, in capturing the full transition from low strain rate, non-affine flow to high strain rate, laminar flow. In the Sections 3.2 and 3.3 we focus on the former, and we shall see how dissipative rearrangements in the foam under flow leads to shear-induced diffusion of the bubbles with a characteristic relaxation time intrinsically linked to the flow properties. In the Section 3.4, we investigate the transition to the high strain rate regime, where we see the Herschel-Bulkley equation no longer holds, and where a dramatic change in microscopic dynamics leads to distinctly different rheology.

3.1 Origin of non-linear rheology

Two different aspects of foam flow contribute to the complex bulk rheology. First, the drag force experienced by neighbouring bubbles sliding past each other is nonlinear [22, 48] and governed by a power law of the relative velocity: $\Delta \mathbf{v}^\alpha$. Depending on the nature of the surfactant, the exponent α lies in the

range $\alpha \approx 0.2 - 0.5$. Denkov and co-workers [21, 22, 61] have shown in experiments and theoretical work that the viscous stress is directly related to this non-linear viscous interaction between the bubbles, at least for high strain rates. Their model prediction is based on the flow of ordered foams in experiments carried out by Princen [53].

The other source of non-linearity is more subtle. As the foam is sheared, bubbles compress and built-up stress is relaxed through local bubble rearrangements. The interplay between elastic loading and subsequent dissipative relaxation leads to intermittent bubble dynamics with transient swirls. Therefore, at least for low strain rates, bubbles do not move smoothly along the direction of shear, seen clearly in Figure 2.2.

This appears to be the reason why the macroscopic stress scales differently than the viscous dissipation between bubbles, as was shown both in experiments [48] and simulations [52] which probed the low strain rate regime.

A recent model by Tighe et al. [79] predicts a viscous regime at high strain rates where the shear stress simply scales with the local bubble-bubble dissipation. At low strain rates, the competition between elastic and viscous forces leads to an effective Herschel-Bulkley exponent lower than expected from the local drag law.

We show that the results from the soft disk model, as detailed below, are consistent with recent experimental observations in both the low and high strain rate regime.

3.2 Non-affine motion of disks under shear

In a flowing foam bubbles undergo continuous rearrangements which leads to random motion with respect to the steady-state mean flow $\langle \mathbf{v} \rangle(y)$. In this section, we analyse this so-called *non-affine* motion for a system of $N = 1500$ bubbles in the bulk, with $N_{\text{Wall}} = 80$ bubbles making up the walls, and the channel width $L = 33\langle d \rangle$, where $\langle d \rangle$ is the average bubble diameter. The packing fraction is set to $\phi = 0.95$. For the purposes of our analysis of bubble fluctuations, we consider only bubbles with y-coordinates of $0.2L < y < 0.8L$,

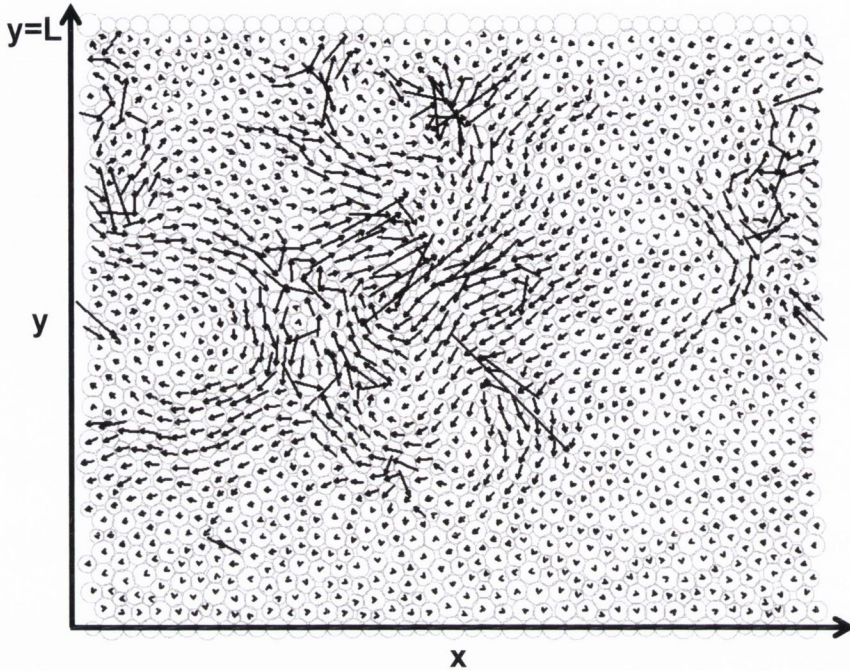


Figure 3.1: **Non-affine velocity vector field for low strain rate.** Visualisation of a soft disk model simulation, with $De = 3.79 \times 10^{-5}$ and $\phi = 0.95$. The arrows show the instantaneous non-affine velocity vectors of the bubbles, that is their velocities minus the steady-state mean flow $\langle \mathbf{v}(y) \rangle$. We see complex, swirling patterns and strongly non-affine motion in this low strain rate regime. The wall bubbles have no arrows, as their non-affine velocities are imposed by the simulation to be zero.

to avoid edge effects due to close proximity to the boundary. We return to a discussion of what happens close to the boundaries in Chapter 4.

3.2.1 Mean Square Displacements

Fluctuations from the steady-state mean flow can be quantified by non-affine displacements [29, 62, 81] $\Delta \mathbf{s}(\Delta t)$ over some time interval Δt , which are defined as follows

$$\Delta \mathbf{s}(\Delta t) = \mathbf{r}(t + \Delta t) - \mathbf{r}(t) - \langle \mathbf{v} \rangle(y) \Delta t, \quad (3.1)$$

where $\mathbf{r}(t)$ is the trajectory of a bubble. In a linear shear geometry the average velocity of the foam, $\langle v_x \rangle(y)$, changes linearly with y , as shown in Figure 2.3. We note that, for constant strain rate, the time interval Δt is directly proportional to the strain interval $\Delta\gamma$ - as a dimensionless quantity, the latter is often a more convenient choice of variable.

Figure 3.1 shows a visualisation of the non-affine flow of bubbles in our simulations, for $De = 3.79 \times 10^{-5}$ and $\phi = 0.95$. The black arrows plot the instantaneous non-affine velocity vectors of the bubbles, that is, their individual velocities minus $\langle v_x \rangle(y)$, during linear shear. The strongly non-affine displacements and swirling, transient motion shown are characteristic for the simulations, in the low strain rate regime. While an individual vortex in the bubble motion is transient, in general these vortices form and dissipate continuously over short timescales throughout the steady state flow.

For our analysis, we concentrate on the non-affine motion in the y direction, transverse to flow. Longitudinal motion presents difficulties when subtracting the mean flow. In calculating the mean flow we average the displacements of the bubbles into bins. The longitudinal mean flow is thus discretised, and there can be small errors upon subtraction when the bubbles' y -coordinates change. These errors, while small, accumulate throughout calculations. The mean flow in the transverse direction is zero, and the fluctuations in the mean flow with time are smaller, producing much smoother statistics.

From the non-affine displacements, Equation (3.1), we can compute the mean square displacement $\langle \Delta s_y^2 \rangle$ transverse to the shear direction. Figure 3.2(a) shows the change of $\langle \Delta s_y^2 \rangle$ with strain $\Delta\gamma$ at $De = 7.6 \cdot 10^{-5}$, which is again in the low strain rate, Herschel-Bulkley regime.

The corresponding probability distribution functions (PDFs) in Figure 3.2(b) of the transverse non-affine displacements $\Delta s_y(\Delta t)$ reflect the qualitative change in behaviour as a function of strain interval. At low strain intervals $\Delta\gamma$, we see a fat-tailed distribution. Such distributions are often encountered in the study of complex systems, and we will return to a much more detailed discussion of them in Chapter 6. The majority of the bubbles move very little relative to the bulk flow of the medium; hence the PDF of the non-affine

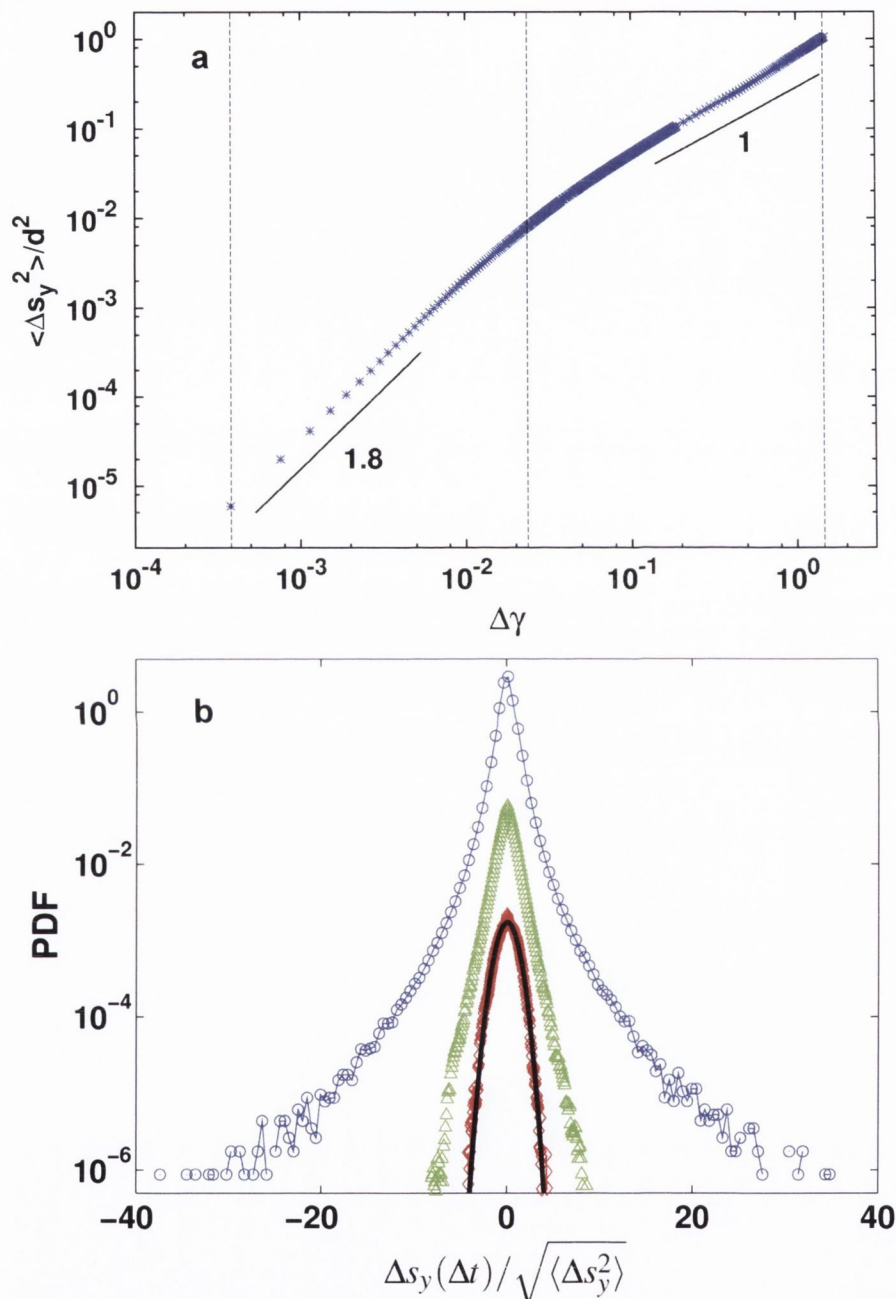


Figure 3.2: **Non-affine displacements at low strain rate.** (a) Transverse mean square displacement $\Delta s_y(\Delta t)/d^2$, non-dimensionalised by the average bubble diameter d , plotted as a function of strain $\Delta\gamma = \dot{\gamma}\Delta t$ at $De = 7.6 \cdot 10^{-5}$. The black lines indicate the super-diffusive and diffusive regimes, where the logarithmic slopes are 1.8 and 1, respectively. (b) The distributions of the non-affine displacements transverse to the shear direction $\Delta s_y(\Delta t)/\langle \Delta s_y^2 \rangle^{0.5}$ for three different strains $\Delta\gamma$ at $De = 7.6 \cdot 10^{-5}$ as indicated by the dotted vertical lines in (a). The distributions are shifted for clarity and are normalised by their respective widths. (\circ) $\Delta\gamma = 3.4 \cdot 10^{-4}$; (\triangle) $\Delta\gamma = 2.3 \cdot 10^{-2}$; (\diamond) $\Delta\gamma = 1.46$. The black curve is a fit to a Gaussian. The initially fat tail distributions converge to a Gaussian with increasing strain $\Delta\gamma$.

displacements has a strong peak at 0. However, when a rearrangement does occur it causes a very large movement relative to the bulk flow, leading to fat tails.

In contrast, at high $\Delta\gamma$, we obtain a Gaussian PDF, a signature of diffusion. We shall focus on this diffusion in the next section. At the crossover between the two regimes we observe exponential tails, similar to those found in the experiments of Möbius *et al.* [29].

The mean square displacements $\langle \Delta s_y^2 \rangle$, as a function of strain interval $\Delta\gamma$, follow the same trend for a wide range of Deborah numbers, as shown in Figure 3.3. Note that the curves do not lie on top of each other. We conclude from this that the fluctuations are not rate-independent, that is, shearing twice as fast does not cause the same fluctuations to occur, just twice as quickly. This affords immediate insight into the origin of non-linearity in foam rheology: the stress cannot scale linearly with strain rate (as for Newtonian fluids, or Bingham fluids past a certain yield stress regime [13]) when the motion of the bubbles - which ultimately affects their interactions with the walls and thus the stress - is non-trivially rate-dependent.

For a given strain, we find the fluctuations of the bubbles to decrease with strain rate, which again agrees with experimental observations [29].

3.2.2 Shear-induced diffusion in foams

In thermal systems, particles are subject to diffusion over time due to random vibrational motion associated with their thermal energy. In general, the mean square displacement of particles, $\langle \Delta s^2 \rangle$, diffusing in time Δt can be described by the diffusion equation,

$$\langle \Delta s^2 \rangle = 2nD\Delta t^{d_w}, \quad (3.2)$$

where n is the number of dimensions, D is the *diffusion constant* and d_w is the *anomalous diffusion exponent* [98].

For normal diffusion $d_w = 1$, and one recovers the familiar Brownian motion or random walk, i.e. $\langle \Delta s \rangle \propto \sqrt{t}$. We call this the *diffusive regime*. This regime corresponds to regions of slope 1 in logscale plots of $\langle \Delta s^2 \rangle$ against

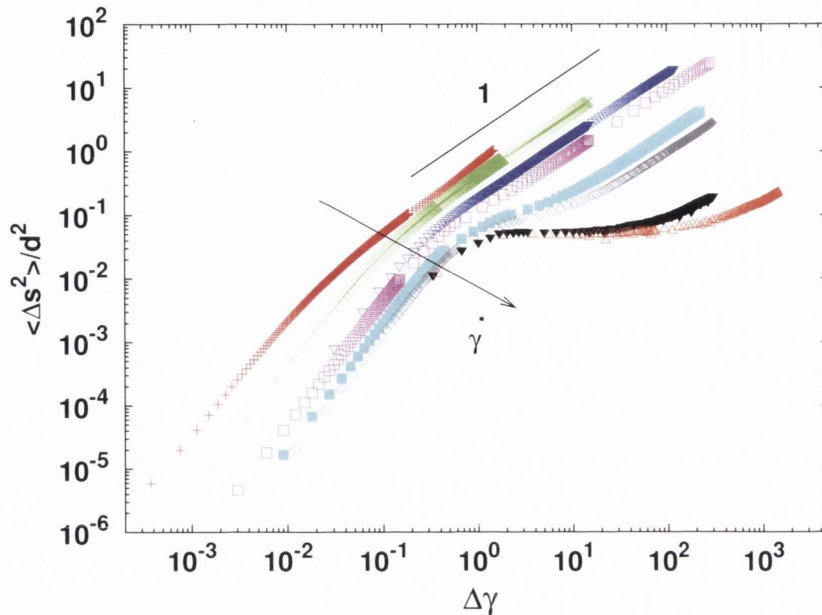


Figure 3.3: **Mean square displacement versus strain interval.** $\langle \Delta s_y^2 \rangle$ plotted as a function of $\Delta \gamma$, for a range of Deborah numbers (\propto strain rates): De : (+) $7.6 \cdot 10^{-5}$; (\times) $7.6 \cdot 10^{-4}$; (∇) $6.1 \cdot 10^{-3}$; (\square) $1.5 \cdot 10^{-2}$; (\blacksquare) $4.6 \cdot 10^{-2}$; (\diamond) $6.1 \cdot 10^{-2}$; (\blacktriangledown) $6.8 \cdot 10^{-2}$; (\triangle) $7.6 \cdot 10^{-2}$. The black line indicates a slope of 1 which corresponds to diffusion. At high strain rates a plateau emerges as a result of lane motion, discussed further in Section 3.4.

$\Delta \gamma$ (analogous to Δt for constant strain rate $\dot{\gamma}$), as is plotted in Figures 3.2 (a) and 3.3.

For transport through porous media, fractal networks, and other complex systems such as financial markets (see Chapter 6), *anomalous diffusion* has been observed [98]. Here, d_w can have a value less or greater than 1, corresponding to a *subdiffusive* (slope < 1) or *superdiffusive regime* (slope > 1) respectively.

In Figures 3.2 (a) and 3.3, linear regions of slope 1 are visible for sufficiently high $\Delta \gamma$, consistent with diffusion. Furthermore, as shown in Figure 3.2 (b), we recover Gaussian distributions for non-affine displacements at high strain intervals. The Gaussian function is a solution of the linear diffusion equation $\frac{\partial P}{\partial t} = D \nabla^2 P(x, y)$. From these observations, the conclusion is drawn that the bubbles undergo diffusion.

However, unlike similar colloidal systems such as glasses, which have thermal interactions and thus undergo thermal diffusion, foams are athermal systems. In foams, this diffusive motion is instead due to a process called *shear-induced diffusion*, where diffusion of bubbles over time results solely from the topological structural rearrangements caused by the shearing of the foam. For a sufficiently large strain, the non-affine motion of an individual bubble undergoing successive rearrangements as the foam flows is well-described by a random walk, where the “steps” are irreversible T1 transitions.

It is interesting to note that, for short times, we observe the mean square displacements to be superdiffusive, scaling as approximately $t^{1.8}$ (Figure 3.2 (a)). A scaling with t^2 would correspond to ballistic motion, which we would not expect since in our model the disks are at all times in contact with neighbours and thus subject to a dissipative force. Superdiffusion has been found to arise in systems featuring fat-tailed distributions such as Lévy flights [99]. Here, then, it is perhaps not surprising that our fat-tailed, strongly nonaffine motion generated by T1 transitions scales superdiffusively at short times. Superdiffusion has been attributed to active cell transport properties, where average local motion is expedited above that of a random-walk diffusion by topology or chemical interactions [100].

From our mean square displacements, we can thus calculate strain rate dependent diffusion constants, $D(\dot{\gamma})$. We use the relevant, simplified form of Equation (3.2),

$$\langle \Delta s_y^2 \rangle = 2D(\dot{\gamma})\Delta t, \quad (3.3)$$

fitting to the data in the diffusive regime.

As seen from Figure 3.4, the diffusion constant D increases with strain rate. This behaviour is expected since diffusion is a direct result of shear-induced rearrangements whose rate is increasing with $\dot{\gamma}$.

At low strain rates, we find that D is approximately linear in $\dot{\gamma}$ as is expected in a quasistatic regime where all the displacements scale with the strain; i.e. as the strain rate is doubled, the rate of rearrangements doubles

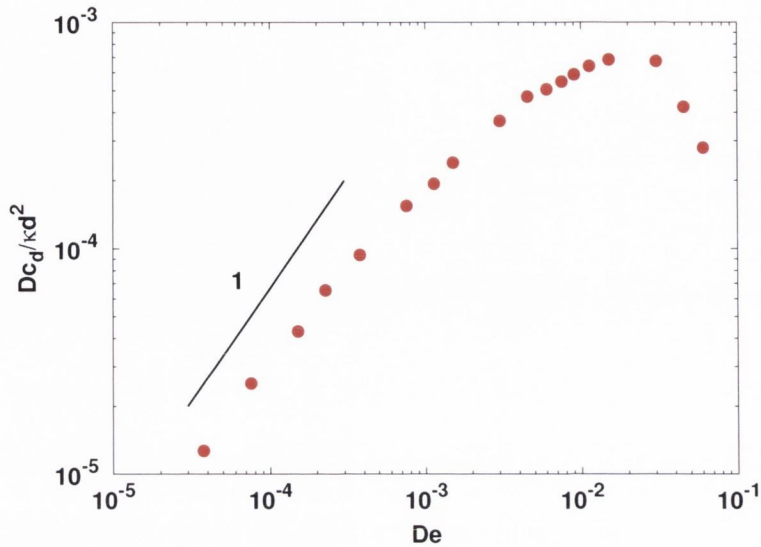


Figure 3.4: **Diffusion constants versus Deborah number.** Normalized diffusion constant $Dc_d/(\kappa d^2)$ as a function of De . At low De , $D \propto De$. For $De > 0.03$ D is starting to decrease due to bubbles starting to be trapped in lanes.

which in turn leads to twice as much diffusion. In experiments on two-dimensional foams this quasistatic regime [29, 97] has not been observed, presumably due to the fact that creep due to coarsening would dominate at these low strain rates.

At around $De \approx 10^{-3}$, the increase of D becomes nonlinear, which is also observed in experiments [29] and simulations of the Durian bubble model [81]. A power law scaling for D has been suggested in experimental work by both Wang *et al.* [62] and Möbius *et al.* [29]. We observe there to be a nontrivial scaling of D over a larger range of strain rates than examined in these papers, in agreement with simulations of Ono *et al.* [81].

At yet higher Deborah numbers we see, once again, that the behaviour of the system undergoes a qualitative change, at around the same Deborah number where we found the Herschel-Bulkley equation to no longer accurately describe the data (Section 2.2), and the empirical fit to the Pouliquen model collapse to fail (Section 2.3).

Here, finally, we can glean an insight into why this occurs. This change in behaviour arises from a change in dynamics at the bubble level. The bubbles start to become trapped in moving lanes parallel to the shear direction, as shown in Figure 3.8. We postpone the discussion of this high strain rate regime until later in this chapter. For now, we shall simply highlight that this lane motion is the origin of the plateau in the mean square displacement starting at approximately $\Delta\gamma = 1$, seen in Figure 3.3. These plateaus occur at approximately an average displacement $\langle\Delta s\rangle \approx 0.2\langle d\rangle$, a fraction of a diameter, indicating the bubbles become trapped in lanes. At large strains, lane switching of the bubbles eventually causes transverse diffusion, on a different timescale. For this reason, the diffusion constant decreases for Deborah numbers greater than 0.03. We shall return to this transition to lane motion in Section 3.4.

3.3 A deformation-relaxation model for foam flow at low strain rate

We now relate the rearrangement rate, measured from the non-affine bubble fluctuations, to the rheology of the simulated foam in an approach similar to previous experimental [29] and theoretical work [79,95]. This approach is akin to a deformation-relaxation model that is usually used to describe the microscopic origin of viscosity in Newtonian fluids.

3.3.1 The relaxation time

In Newtonian fluids, viscosity η can be related to the dissipation rate per unit volume [94]. Consider a small volume within a flowing Newtonian liquid, dimensions Δx by Δy by Δz . The work done to maintain the flow (velocity \mathbf{v}) of the liquid in the z-direction is given by:

$$\frac{dW}{dt} = F\mathbf{v} = (\sigma\Delta x\Delta y)(\dot{\gamma}\Delta z). \quad (3.4)$$

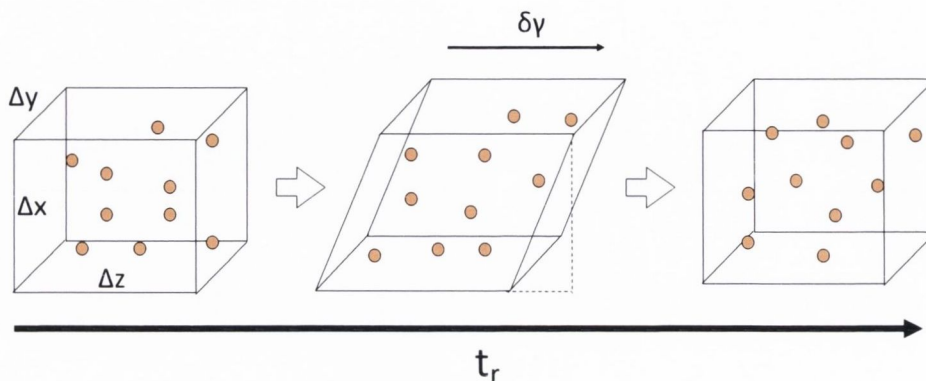


Figure 3.5: **Schematic representation of the relaxation time model for Newtonian fluids.** The small volume of fluid, $\Delta x \Delta y \Delta z$, undergoes small strain steps, $\delta\gamma$, and then relaxes fully by dissipating the elastic energy generated. The model can be used to estimate the viscosity η of Newtonian fluids, of the order of inverse picoseconds [94].

The dissipation rate per unit volume \dot{w} is thus:

$$\dot{w} = \sigma \dot{\gamma}. \quad (3.5)$$

Combining Equations (1.8) and (3.5), one obtains $\dot{w} = \eta \dot{\gamma}^2$. The viscous dissipation can be visualised by imagining the continuous strain as a series of sudden, tiny jumps. After each such jump, the work done to shear the foam is dissipated by the collisions of the molecules in the fluid, dissipating the elastic energy. These deformation-relaxation cycles occur on the time scale of the microscopic relaxation time t_r . From this analysis it follows that the viscosity of thermal fluids $\eta \propto t_r$, where the relaxation time depends on the temperature. [94].

Prior studies of colloidal glasses found microscopic relaxation times that scaled non-linearly with the inverse local strain rate, but no direct and quantitative connection to rheology had been established [101, 102]. Möbius *et al.* applied the same relaxation time analysis to foam flow, by tracking the bubbles using image analysis software and resolving each of the bubbles' po-

sitions and velocities as functions of time [29]. In foams, which are athermal, the relaxation is not driven by temperature but is entirely shear-induced (ignoring coarsening on long time scales) and one may interpret the corresponding relaxation time scale as the typical inverse rearrangement rate of the bubbles, which depends on the local strain rate.

We use the diffusion constant as a measure of the rate of plastic, dissipative rearrangements $1/t_r$. Following the theoretical work of Martens *et al.* linking the size of cooperative regions in amorphous flow to the diffusion coefficient [103], we postulate that $D \propto 1/t_r$. More precisely, we define the relaxation time to be the onset of the diffusive regime where $\langle \Delta s_y^2 \rangle \propto \Delta t$. A similar relation between relaxation time and diffusion constant has also been observed in sheared colloidal systems [101].

This allows us to plot the mean square displacements from Figure 3.3 versus a rescaled time axis $\propto \Delta t/t_r$, which is simply $D(\dot{\gamma})\Delta t/d^2$, where the average bubble diameter d appears on dimensional grounds. The result is shown in Figure 3.6.

At all Deborah numbers we find that the curves converge to the diffuse regime when the mean square displacement exceeds $\langle \Delta s_y^2 \rangle / d^2 \approx 0.18$, which is close to the Lindemann criterion. The criterion was first put forward by Lindemann to explain the melting transition in crystalline solids, stating that melting would occur when particles had sufficient thermal energy that their root mean square vibrational amplitudes exceeded 10% of their nearest neighbour distance on the lattice [104]. In colloidal systems this is equivalent to cage-breaking [101].

The corresponding relaxation time t_r is given by

$$t_r = 0.09 \frac{d^2}{D(\dot{\gamma})}, \quad (3.6)$$

as indicated in Figure 3.6.

Experiments of two-dimensional foams have shown a collapse of the non-affine fluctuations, $\langle \Delta s_y \rangle$ over two decades in shear rate [29]. While we see an approximate collapse for low Deborah numbers over two decades, this does not hold for the whole range of shear rates that were probed. Nevertheless,

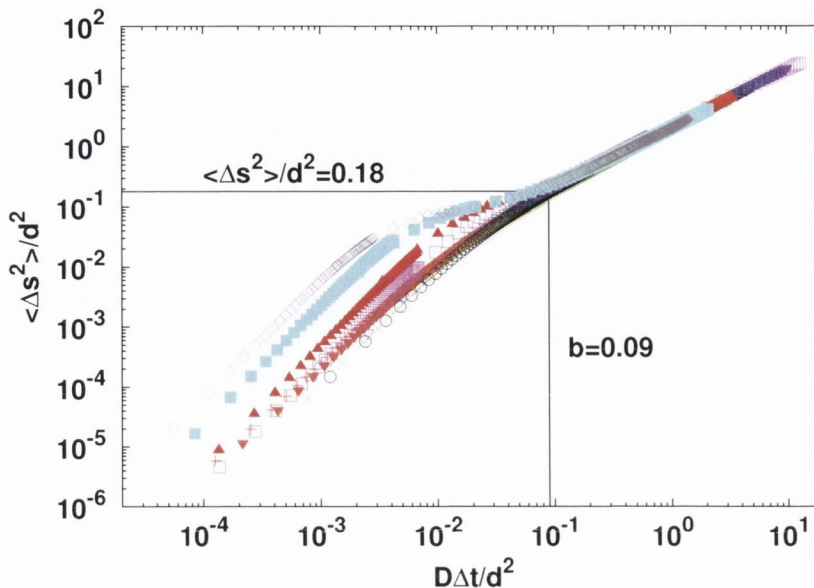


Figure 3.6: **Mean square displacements rescaled by diffusion constants.** Mean square displacements in the transverse direction for different De : (+) $7.6 \cdot 10^{-5}$; (◆) $1.5 \cdot 10^{-4}$; (×) $7.6 \cdot 10^{-4}$; (○) $1.5 \cdot 10^{-3}$; (∇) $6.1 \cdot 10^{-3}$; (□) $1.5 \cdot 10^{-2}$; (▲) $3.0 \cdot 10^{-2}$; (■) $4.6 \cdot 10^{-2}$; (◇) $6.1 \cdot 10^{-2}$. The time axis is rescaled with the diffusion constant $D(\dot{\gamma})/\langle d \rangle^2$. The onset of the diffusive regime occurs approximately at $\Delta t D / d^2 = b$, where $b \approx 0.09$. The corresponding mean square displacement is at $0.18d^2$.

the onset of the diffusive regime is well characterised by the Lindemann criterion for all Deborah numbers.

3.3.2 Relating local relaxation to the bulk deformation

We can associate a characteristic strain γ_c with t_r , such that

$$\gamma_c = t_r \dot{\gamma}. \quad (3.7)$$

In the deformation-relaxation ansatz [94], we relate the characteristic strain γ_c to the shear stress by the elastic modulus G_0 ,

$$\sigma = a \cdot G_0 \gamma_c, \quad (3.8)$$

where a is a dimensionless constant of proportionality. Combining Equations (3.6), (3.7) and (3.8), we have:

$$\sigma = a \cdot G_0 \frac{0.09d^2}{D(\dot{\gamma})} \dot{\gamma}. \quad (3.9)$$

We now have two expressions for the stress σ , Equation (1.10) and Equation (3.9), both shown for comparison in Figure 3.7. The former is the empirical Herschel-Bulkley equation, while the latter is obtained solely from measurements of the bubble-bubble dynamics, namely the bubble rearrangement rate $1/t_r$. We note that a is the only fitting parameter in this model for Equation (3.9) and is of order 1 ($a = 0.24$). We see that our derived expression describes the measured stresses very well and is indistinguishable from a fit to the empirical Herschel-Bulkley equation (Equation (1.10)).

However, beyond $De = 0.005$ the prediction from Equation (3.9) is no longer adequate to describe the data. This transition is marked by a vertical line in Figure 3.7. The physical reason for this is that at this point the relaxation time t_r becomes greater than the inverse strain rate (Figure 3.7(b)). In other words, to the right of this line the shearing timescale $\dot{\gamma}^{-1}$ is shorter than the relaxation time and prevents the foam from fully relaxing after rearrangements.

This transition can also be observed by decomposing the shear stress σ into the elastic and viscous contributions $\langle \sigma_E \rangle$ and $\langle \sigma_V \rangle$, as was done by Tighe et al. [79]. We plot these stress components versus De as shown in Figure 3.7(c).

The elastic forces are due to the overlap between the bubbles, which does not change significantly with strain rate. The viscous forces increase monotonically as expected, although in a non-linear fashion. At $De \approx 0.005$ we see a crossover at which $\langle \sigma_V \rangle$ starts to dominate. Curiously, we also

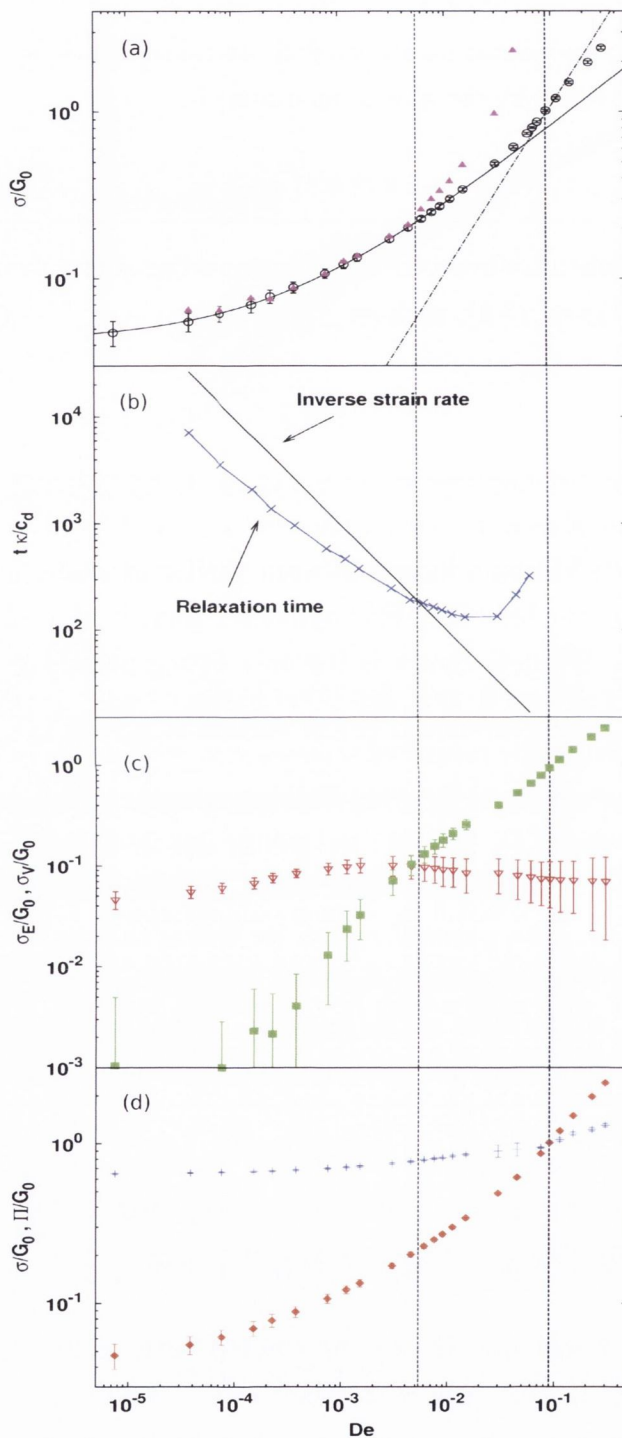


Figure 3.7: **Comparison of deformation-relaxation ansatz with stress versus Deborah number.** (a) Shear stress versus De , with Herschel-Bulkley fit (as in Figure 2.6) in black. The purple triangles correspond to $\frac{\sigma}{G_0} = a \frac{0.09d^2}{D(\dot{\gamma})} \dot{\gamma}$ with $a = 0.24$. (b) Relaxation time t_r (\times) and inverse strain rate (black line) plotted versus Deborah number. The vertical line at $De = 0.005$ marks the transition between $t_r < \dot{\gamma}^{-1}$ and $t_r > \dot{\gamma}^{-1}$. (c) Elastic $\langle \sigma_E \rangle$ (∇) and viscous $\langle \sigma_V \rangle$ (\blacksquare) components of the shear stress versus De . (d) Normal stress Π ($+$) and shear stress σ (\blacklozenge) versus De . Second vertical line at $De = 0.09$ corresponds to $\Pi = \sigma$.

observe that the elastic component of the shear stress begins to decrease at this point. We will return to this in Chapter 4.

The rheology before this crossover is well described by a Herschel-Bulkey fit with exponent 0.51 which is consistent with the Leiden group model [79], falling in their “critical” regime.

Our results differ from experiments of Möbius et al., where the relaxation time has been observed to be proportional to the viscous stress [29]. We believe this discrepancy is due to limitations of the experiments. Although the dynamics were measured in a linear geometry, the rheology was measured in a Couette geometry which was later shown to exhibit a non-local rheology [105].

3.4 Rheology at high strain rate

From the previous section, it is clear that the relaxation time ansatz that links shear-induced diffusion and shear stress breaks down when $De > 0.005$. The viscous forces dominate and the deformation time scale $1/\dot{\gamma}$ becomes shorter than the relaxation time scale t_r .

3.4.1 The transition between non-affine motion and laminar flow

At this point we see a dramatic change in the bubble dynamics. Instead of intermittent, swirl-like motion of the bubbles (Fig 2.2), we observe a laminar-type flow, where bubbles flow predominantly along the shear direction (Fig 3.8). This shear-induced ordering is somewhat surprising, given the polydispersity of the foam.

Returning to the mean square displacements $\langle \Delta s_y(\Delta t) \rangle$, we can see too that there has been a marked change in their distributions, characteristic of the change in dynamics. Figure 3.9 (a) shows $\langle \Delta s_y(\Delta t) \rangle$ versus $\Delta\gamma$ for $De = 7.6 \cdot 10^{-2}$. After some (average) time trapped in a lane, indicated by the plateau where $\langle \Delta s_y(\Delta t) \rangle \approx 0.2\langle d \rangle$, the bubble escapes and continues to diffuse, albeit this time in a random walk whose step is now the transition

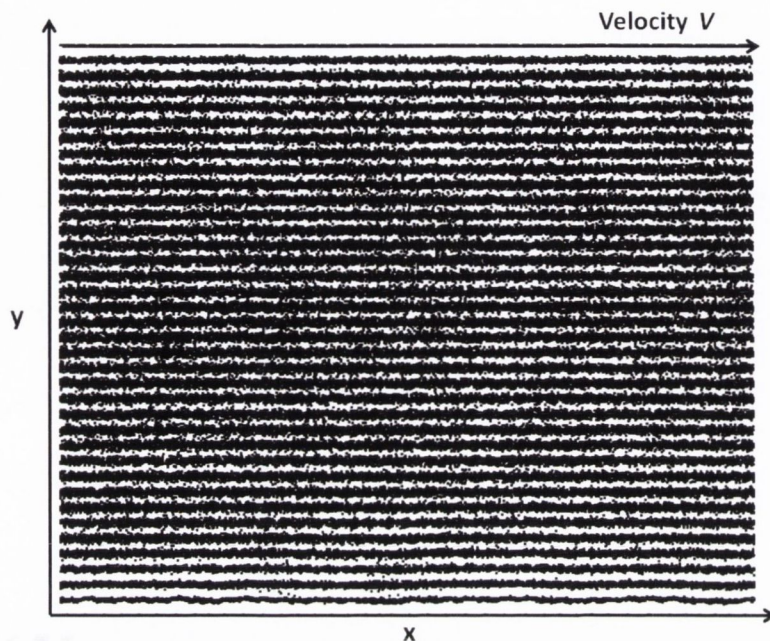


Figure 3.8: **Laminar flow.** Bubble trajectories of a linearly sheared foam, at $De = 7.6 \cdot 10^{-2}$. Black trails represent the positions of the bubble centres during a total strain of $\Delta\gamma = 38$. The bubbles move predominantly along the shear direction with reduced transverse motion. Collective, swirly bubble rearrangements have ceased.

between lanes. The black vertical lines mark different values of strain interval $\Delta\gamma$, $a = 0.379$, $b = 0.758$, $c = 5.682$, $d = 37.879$, $e = 189.39$ and $f = 757.58$, for which we calculate PDFs and plot them in Figure 3.9 (b).

In Figure 3.9 (b), we see that the PDFs of mean square displacements are now dramatically different from those shown in Figure 3.2 (b). For clarity of discussion, we normalise the displacements by the bubble lane width, equal to $0.92\langle d \rangle$. This value is obtained by noting that although the channel is $L = 33\langle d \rangle$, there are 36 bubble lanes due to the compression of the system, as visible in Figure 3.8.

At short times, e.g. for a and b in Figure 3.9, we observe Gaussian distributions with widths less than a lane width. Here, the bubbles are subject to normal diffusion, over short distances within a lane. For c and d , within the plateau, we see approximately Gaussian distributions, with

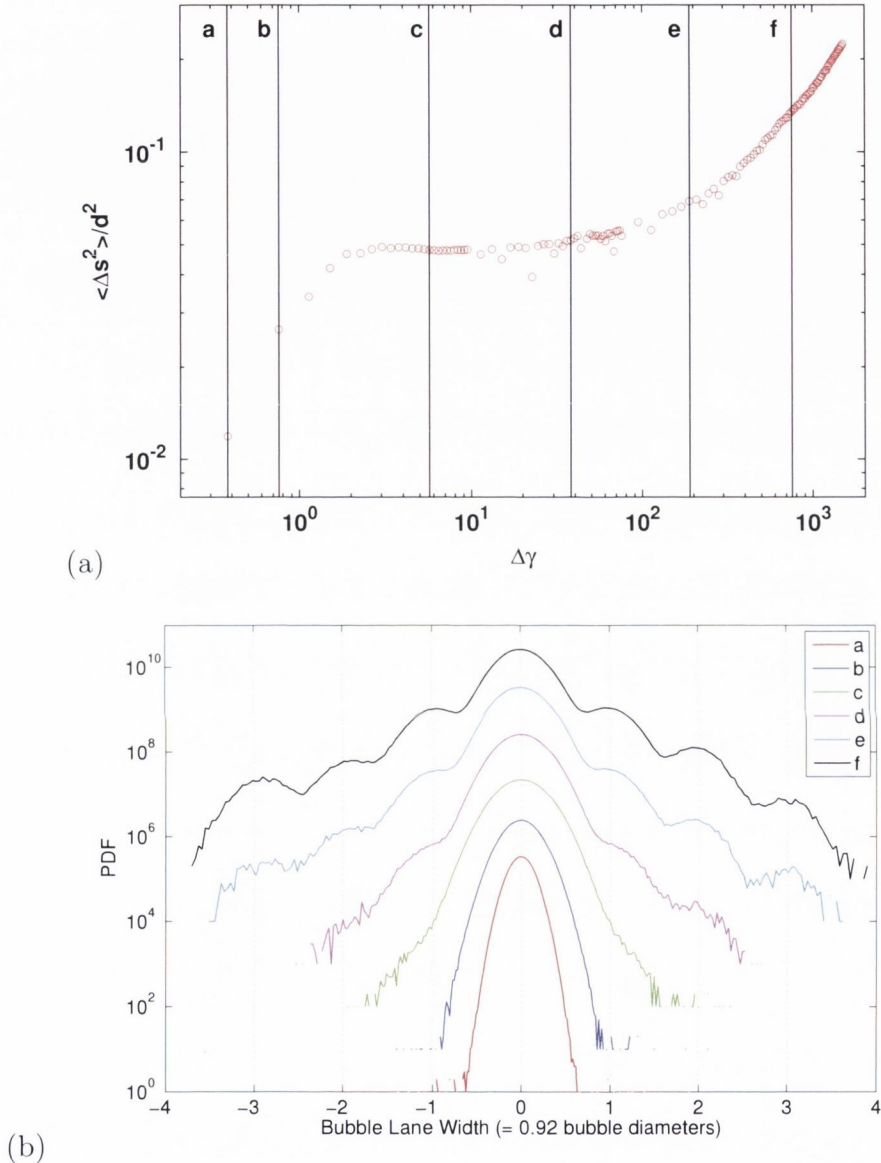


Figure 3.9: **Mean square displacements for high strain rate lane motion.** $De = 7.6 \cdot 10^{-2}$ (a) Transverse mean square displacement $\Delta s_y(\Delta t)/d^2$ plotted as a function of strain $\Delta\gamma = \dot{\gamma}\Delta t$. The vertical black lines illustrate values of $\Delta\gamma$ for which we calculate PDFs, shown in (b). These values are $a = 0.379$, $b = 0.758$, $c = 5.682$, $d = 37.879$, $e = 189.39$ and $f = 757.58$. (b) The distributions of the non-affine displacements transverse to the shear direction $\Delta s_y(\Delta t)$ for six different strain intervals $\Delta\gamma$ as indicated by the vertical lines in (a) and listed above. The distributions are shifted for clarity and are normalised by bubble lane width, which is given by $0.92\langle d \rangle$. Clear peaks at integer values of bubble lane width show that the bubbles tend to move between lanes, i.e. the lane motion is persistent throughout the whole sample. As the strain interval increases, the bubbles diffuse between lanes.

additional fat tails. Here, while the majority remain confined within a lane, a few bubbles begin to escape. Finally, for e and f , past the plateaus, many of the bubbles (on average) have diffused between lanes. We see strong peaks in the distributions at integer values of bubble lane width, consistent with jumps between discrete y-coordinates set by the lane positions. Over time, these peaked functions become enveloped by normal diffusion on a different timescale to diffusion in the early motion depicted in a and b .

3.4.2 Viscous scaling via the local drag law

We have seen that in this high strain rate regime, with strongly ordered lane motion, the Herschel-Bulkley equation (1.10) no longer describes the variation of the shear stress with strain rate. Such an ordered flow pattern features in the models proposed by Princen [53] and Denkov [22, 61].

In this case, the shear stress may be directly related to the local drag law (Equation (2.4)). Suppose the lanes are approximately one bubble diameter wide, and that the force on these lanes is governed primarily by the viscous drag between them. Then, $\sigma \approx \frac{F_d}{d} = c_d \frac{\Delta v}{d} = c_d \dot{\gamma}$, yielding (from Equation (2.9)):

$$\sigma = \kappa \cdot De \tag{3.10}$$

This analysis leads to the conclusion that for high Deborah numbers the stress ought to scale simply with the local bubble-bubble drag (in our case, linearly). We compare the prediction (Equation (3.10)), which contains no free parameters, with our data as shown in Figure 3.7(a) and find good agreement. The onset of this linear regime ($De = 0.09$) coincides with the crossover at which the shear stress becomes larger than the normal stress as shown in Figure 3.7(d). Note that the transition to the viscous regime does not occur when the viscous contribution of the shear stress exceeds the elastic one ($De = 0.005$) as predicted by Tighe et al. [79].

The Herschel-Bulkey fit becomes inadequate at around $De = 0.02$, which falls into the intermediate regime, where the stress is neither described by the

viscous prediction (Equation (3.10)) nor the deformation-relaxation ansatz (Equation (3.9)).

The limitations of the soft disk model as outlined in Appendix D prevent us from probing Deborah numbers larger than 0.5.

3.5 Conclusions and Outlook

We have analysed both the macroscopic flow properties and dynamics on the bubble scale over a wide range of strain rates in simulations of two-dimensional foam flows and identified three regimes. In the first regime, for Deborah numbers up to 0.005, the macroscopic deformation time scale $1/\dot{\gamma}$ exceeds the microscopic relaxation time. In addition, the elastic component of the stress dominates over the viscous one (see Figure 3.7(c)). The bubble motion is non-affine and intermittent, leading to shear-induced diffusion. In this regime, the shear stress can be described from a microscopic deformation-relaxation model. The apparent viscosity is proportional to a microscopic relaxation time. This time corresponds to an inverse rate of dissipative bubble rearrangements and is obtained from the measurement of the diffusion constant.

For high strain rates, when the Deborah number exceeds 0.09, the bubbles move in lanes. At the onset of this regime, the shear stresses become larger than the normal stresses. The rheology is consistent with a prediction based on the local bubble-bubble drag law, which is linear in our simulation, so that $\sigma \propto \dot{\gamma}$.

There is one decade in Deborah number between these two distinct regimes. In this intermediate regime the bubble dynamics changes smoothly from non-affine, swirly motion, to fully developed lane motion. This is reflected in the transverse mean square displacement which develops a plateau that widens with increasing strain rate (see Figure 3.3). Therefore, the bubbles become trapped in lanes for longer times as the Deborah number increases.

We note that both the empirical Herschel-Bulkley law (Section 2.2) and the empirical fit for $\mu(I)$ (Section 2.3) provide a good description of the variation in stress up to Deborah number 0.02, which lies about halfway

into the intermediate regime. For the low strain rate regime, these empirical scalings describe the data well. At high strain rate and the advent of laminar flow, the data is better described by drag laws similar to those theorised by Princen and Denkov *et al.*, and observed to hold in experiment.

Our simulations capture, for the first time, the transition from non-linear turbulent flow to laminar flow observed for foams in experiment. In our analysis so far, we have focused on bulk flow behaviour - macroscopic stresses for large systems, and fluctuations in flow away from the shearing boundaries. We now turn the discussion to the effects of finite system size, by considering channels of varying width.

Chapter 4

The Effect of Finite System Size

In Chapter 2, we presented results from soft disk model simulations over a large range of strain rates, and for five different packing fractions. One thing we kept constant, however, was the system size. What happens when we change this system size? In Chapter 3, we analysed the diffusive motion of disks under shear, in a central region away from the boundaries, asserting that this region represents “bulk” behaviour, away from the influences of the boundaries. Can we make this assumption?

In this chapter we address these questions. Finite size effects are a concern in all systems, experimental and simulated. In simulations, these are often overcome by using periodic boundary conditions. Indeed, 2D linearly-sheared molecular dynamics simulations can make use of Lees-Edwards boundary conditions to ensure periodic boundary conditions in both x- and y-directions [79, 106]. In a system with Lees-Edwards boundary conditions, shear is achieved by imposing a velocity in the flow direction on the periodic cells aligned transverse to the flow direction, illustrated schematically in Figure 4.1. This allows the application of a linear shear without boundaries.

Experiments, however, always have boundaries! In this chapter we specifically investigate the effect of boundaries in our soft disk simulations. We vary the channel width L of the systems in order to probe the way shear and

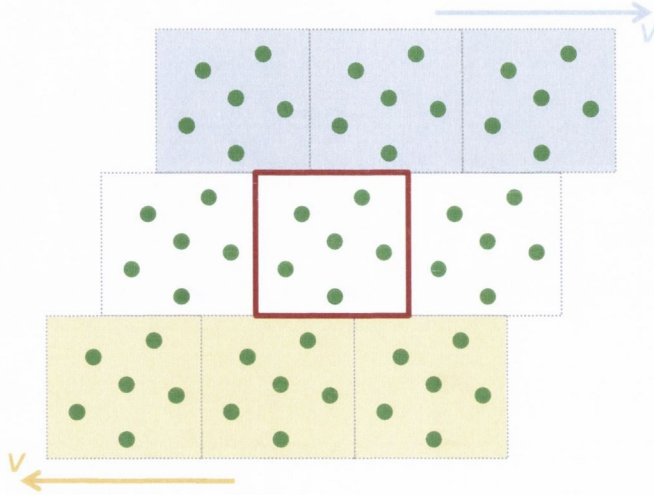


Figure 4.1: **Schematic illustration of Lees-Edwards boundary conditions.** The central cell, outlined in red, represents the simulated system, which is surrounded by periodic copies. A velocity is imposed on the cells highlighted in blue and yellow, generating a linear shear while maintaining periodic boundary conditions.

normal stresses change as a function of L . We find that, exceeding $L \approx 30\langle d \rangle$, where $\langle d \rangle$ is the average bubble diameter, the flow properties of the flows are identical, identifying an upper bound for the minimum width at which bulk properties are observed.

We also return to the constitutive model introduced in Chapter 2, investigating the rescaling of shear and normal stresses in terms of the dimensionless I parameter, as a function of channel width. We find that the constitutive model collapses our data for a given channel width for all packing fractions. However, it does not collapse data for different channel widths. From fits to these collapses, we compute the static angle of repose as a function of channel width, which we compare to experimental measurements of the angle of repose for finite system size.

Channel width L	Number of disks N	N_{Wall}/N
$2\langle d \rangle$	1200	1
$4\langle d \rangle$	1200	0.5
$8\langle d \rangle$	1200	0.25
$16\langle d \rangle$	1380	0.12
$33\langle d \rangle$	1500	0.05
$44\langle d \rangle$	2000	0.04

Table 4.1: **System dimensions for different channel-width simulations.** The first column lists the channel width in terms of average disk diameter $\langle d \rangle$. Columns 2 and 3 list the number of disks in the bulk and in the walls, respectively.

4.1 Simulations of narrow channels

In the majority of the analysis presented in this thesis, we focus on channel dimensions with 80 bubbles in the walls, and channel widths of approximately 33 average bubble diameters. These systems contain 1500 disks not part of the walls. We now extend our analysis to vary the channel width L . In doing so, we also vary the length of the walls, i.e. the number of bubbles that make up the walls. We do this for statistical reasons: although it might be aesthetically pleasing to keep the walls a constant length and vary only the channel width, doing so would mean a reduction in the number of disks in the system for a given packing fraction ϕ . This leads to reduced statistics and noisier signals for measures such as the shear stress σ .

For the results presented here, we use a range of wall lengths and numbers of disks, which we list in Table 4.1. In summary, we examine systems comprising of N disks, where $1200 < N < 2000$, controlling the channel width by varying the ratio of N and the number of wall disks N_{Wall} . Two examples are displayed in Figure 4.2 (a) and (b), which show visualisations of simulations with $L \approx 8\langle d \rangle$ and $L \approx 16\langle d \rangle$ respectively, for $\phi = 0.98$ and similar Deborah numbers.



Figure 4.2: **Visualisations of two narrow-channel simulations.** Packing fraction $\phi = 0.98$. (a) $L = 8\langle d \rangle$, with $De = 3.36 \times 10^{-4}$, $N = 1200$ and $N_{\text{Wall}}/N = 0.25$. Approximately one third of the channel length is shown. (b) $L = 16\langle d \rangle$, with $De = 1.66 \times 10^{-4}$, $N = 1380$ and $N_{\text{Wall}}/N = 0.12$. Approximately two thirds of the channel length is shown.

4.1.1 Finite system size and “bulk” behaviour

The first question we must address is, when is the channel sufficiently wide that simulations for different widths give similar results? Figure 4.3 plots shear stress σ and normal stress Π versus Deborah number, for six channel widths. The data for $L = 33\langle d \rangle$ (black) and $L = 44\langle d \rangle$ (cyan) are visually indistinguishable, and, indeed, in the case of the shear stress are well-fit with the same Herschel-Bulkley parameters, from Equation (1.10). We thus conclude that $L = 33\langle d \rangle$, used in our previous analysis, is sufficiently wide to be considered as an appropriate model for bulk flow.

For $L = 16\langle d \rangle$, and narrower channels, the shear and normal stresses do not collapse. For low values of L , we find $\sigma(\dot{\gamma})$ to decrease, and $\Pi(\dot{\gamma})$ to increase. The second question, then, is: can we explain this behaviour?

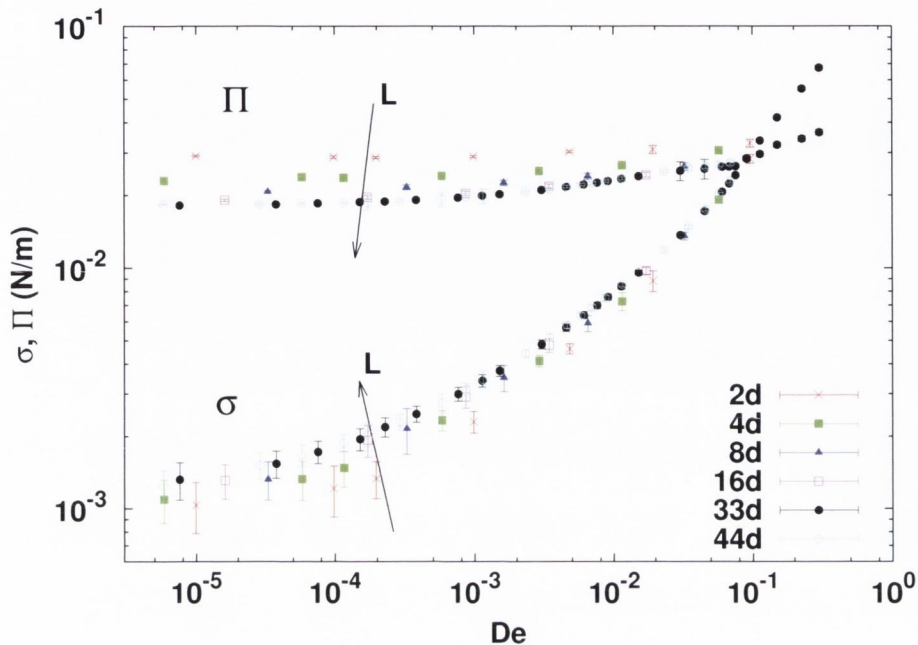


Figure 4.3: **Stress versus Deborah number, for varying channel width.** Shear stress σ (lower curves) and normal stress Π (upper curves) are shown for $\phi = 0.95$, for channel widths: $L = 2\langle d \rangle$, (\times); $L = 4\langle d \rangle$, (\blacksquare); $L = 8\langle d \rangle$, (\blacktriangle); $L = 16\langle d \rangle$, (\square); $L = 33\langle d \rangle$, (\bullet); $L = 44\langle d \rangle$, (\circ). σ is observed to increase for increasing L , up until $L = 33\langle d \rangle$. Π is found to decrease with increasing L in the same range. The data for $L = 33\langle d \rangle$ and $L = 44\langle d \rangle$ are observed to overlap, indicating bulk behaviour has been reached by $L = 33\langle d \rangle$.

4.1.2 A model for the dependence of stress on system size

We attribute this scaling of σ and Π with L to structural considerations. First, we shall focus on σ , by considering a simple, analytically tractable model. Consider a system similar to our simulations, comprising of two walls and two lanes, where the bubbles are monodisperse and constrained to move in lanes (i.e., only their x-coordinates can change), see Figure 4.4 (a). In such a system, the *average* elastic component of the shear stress $\langle \sigma_e \rangle = 0$. This arises due to geometrical symmetry. As Princen *et al.* [56] and Denkov

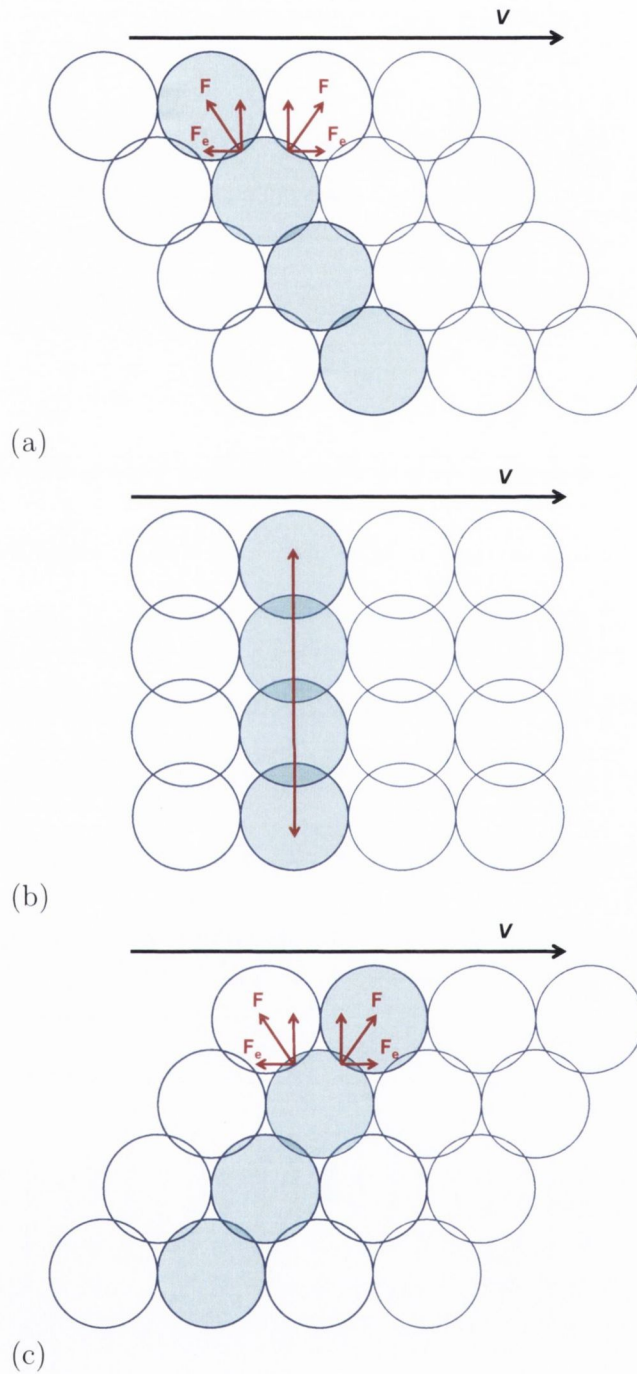


Figure 4.4: **Schematic illustration of simple model with imposed lane motion.** Here, we use a model of monodisperse disks, confined to move in lanes with a linear velocity profile, evolving as (a) through to (c). In such a system, the sum of the elastic components of the forces F_e , shown in (a) and (c) by the horizontal red arrows, is zero due to symmetry. The system passes through a state of maximal normal stress, with maximum possible overlaps when the disk centres align, as shown in (b). Any deviations from this configuration, i.e. non-affine motion, will cause a reduction in the normal stress.

et al. [22], amongst others, have shown, and as we have seen in Chapter 3, the viscous component of the stress for lane motion scales as a simple drag law, which in our case is described by $\langle\sigma_v\rangle \propto \dot{\gamma}$.

This envisaged system provides us with a lower bound for the shear stress. Focusing on the elastic component of the shear stress, we now ask: what increases the average shear stress? The answer is anything that introduces asymmetry. There are two main sources of asymmetry in our model. The first is polydispersity. This is kept at a constant ratio for all of our simulations, and introduces a finite elastic component of the shear stress.

The second is non-affine motion. If we consider our toy model as having a linear velocity profile, combined with each disk moving at the same velocity as the others in its lane and constrained to move in that lane, it is clear to see that the model has no non-affine motion. We postulate that increasing the non-affine motion increases $\langle\sigma_e\rangle$, evidence for which we have already seen in Section 3.3.2. In Figure 3.7, $\langle\sigma_e\rangle$ is seen to decrease as De increases - a decrease which begins at the onset of lane motion.

Non-affine motion is curtailed near the boundaries, which have fixed y -coordinates and inhibit transverse rearrangements in their vicinity. The boundaries themselves encourage the formation of bubble lanes (equivalent to planes of crystallisation at boundary walls, for 3D systems), a phenomenon which has also been seen in experiment [107]. As the channels are widened, the disks have more freedom to undergo rearrangements in the direction transverse to flow, and $\langle\sigma_e\rangle$ increases. Note that at high strain rate, where $\langle\sigma_v\rangle$ dominates, the curves for all channel widths collapse, as this effect on $\langle\sigma_e\rangle$ becomes negligible with respect to σ (or, put another way, systems of *every* size begin to move in lanes).

What about the normal stress, Π ? We follow the same argument, using the same toy model system. For simple shear with a linear velocity profile, the system flows through stages depicted by Figure 4.4 (a)→(c). At stage (b), the system has the highest possible normal stress achievable with that number of disks. Any non-affine motion will *decrease* this value of Π . Once again, the larger the system, the less confined the disks are with respect to transverse motion, and thus the lower the value of Π .

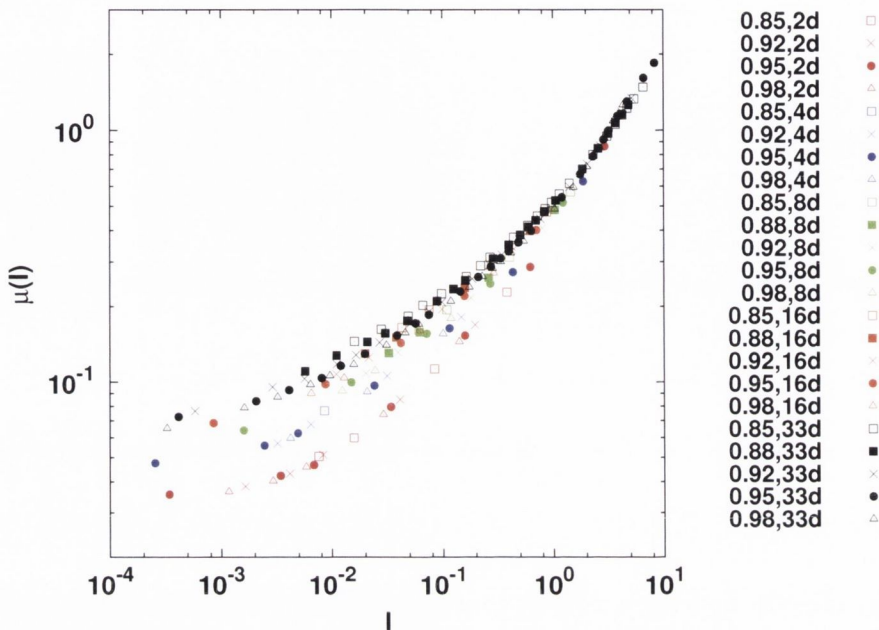


Figure 4.5: **Constitutive scaling for narrow channels.** We plot data for five channel dimensions ($L = 2\langle d \rangle$, blue; $L = 4\langle d \rangle$, red; $L = 8\langle d \rangle$, green; $L = 16\langle d \rangle$, orange; $L = 33\langle d \rangle$, black) and five packing fractions ($\phi = 0.85$, (\square); $\phi = 0.88$, (\blacksquare); $\phi = 0.92$, (\times); $\phi = 0.95$, (\bullet); $\phi = 0.98$, (\triangle)). We omit data for $L = 44\langle d \rangle$ for clarity - as discussed in Section 4.1, the scaling behaviour is identical for $L = 33\langle d \rangle$ and $L = 44\langle d \rangle$.

We now return to the constitutive model, which we found to provide a good description for our stress data as a function of dimensionless parameter I in Section ??.

4.2 Constitutive model for narrow channels

Qualitatively, Figure 4.3 might already lead one to expect that the scaling used for collapse in Section ??, namely

$$\mu(I) = \frac{\sigma}{\Pi} = \mu^* + kI^a \quad \text{where} \quad I = \frac{c_d \dot{\gamma}}{\Pi}, \quad (4.1)$$

should not collapse stress data for different channel widths L , given the different scalings of σ and Π with L discussed in the last section.

In Figure 4.5, we plot $\mu(I)$ versus I for data over a range of packing fractions and channel widths. As expected, the data does not collapse for all channel widths, showing a spread at low I (where the $\langle\sigma_e\rangle$ dominates) and a collapse at high I (where the $\langle\sigma_v\rangle$ dominates).

However, the data is well described by Equation (4.1) if we consider each channel width individually, see Figure 4.6. The solid lines show best fits to Equation (4.1), for data up to $De = 2.0 \times 10^{-2}$, in line with our previous Herschel-Bulkley and constitutive model analysis (see Sections 2.2 and ??). It is noteworthy that the constitutive model provides a good description of the flow for all packing fractions for fixed channel width L .

4.2.1 The angle of repose

In Figure 4.7 we plot the angle of repose $\alpha = \tan^{-1} \mu^*(L)$ and exponent $a(L)$, obtained from the fits to Equation (4.1) shown in Figure 4.6. We find a smooth variation of this data, with asymptotic values in the limit $L/\langle d \rangle \rightarrow \infty$.

The variation of the angle of repose α with channel width $L/\langle d \rangle$ is well described by the empirical functional form $\alpha(L/\langle d \rangle) = \alpha_\infty + \frac{q}{L/\langle d \rangle + r}$, shown by the black line in Figure 4.7 (a), with $\alpha_\infty = 3.7 \pm 0.1$, $q = -11.6 \pm 0.1$ and $r = 3.9 \pm 0.1$. In the limit $L/\langle d \rangle \rightarrow \infty$, $\alpha(L/\langle d \rangle) \rightarrow \alpha_\infty$. From our fit, we thus extrapolate the asymptotic angle of repose in the limit of infinite channel width for our soft disk simulations to be $\alpha_\infty = 3.7 \pm 0.1^\circ$. This value is lower than experimental and simulated values reported in the literature [30,92], as already discussed in Section 2.3.3.

A puzzling result of this analysis is the scaling of the angle of repose α with L for narrow channels. From our simulations, we see that the static angle of repose decreases as system size decreases. This appears to contradict results found in the literature, as follows.

In linear geometry experiments for 3D foams, Lespiat *et al.* list an angle of repose of $\alpha = 4.6 \pm 1^\circ$ that does not depend on system dimensions.

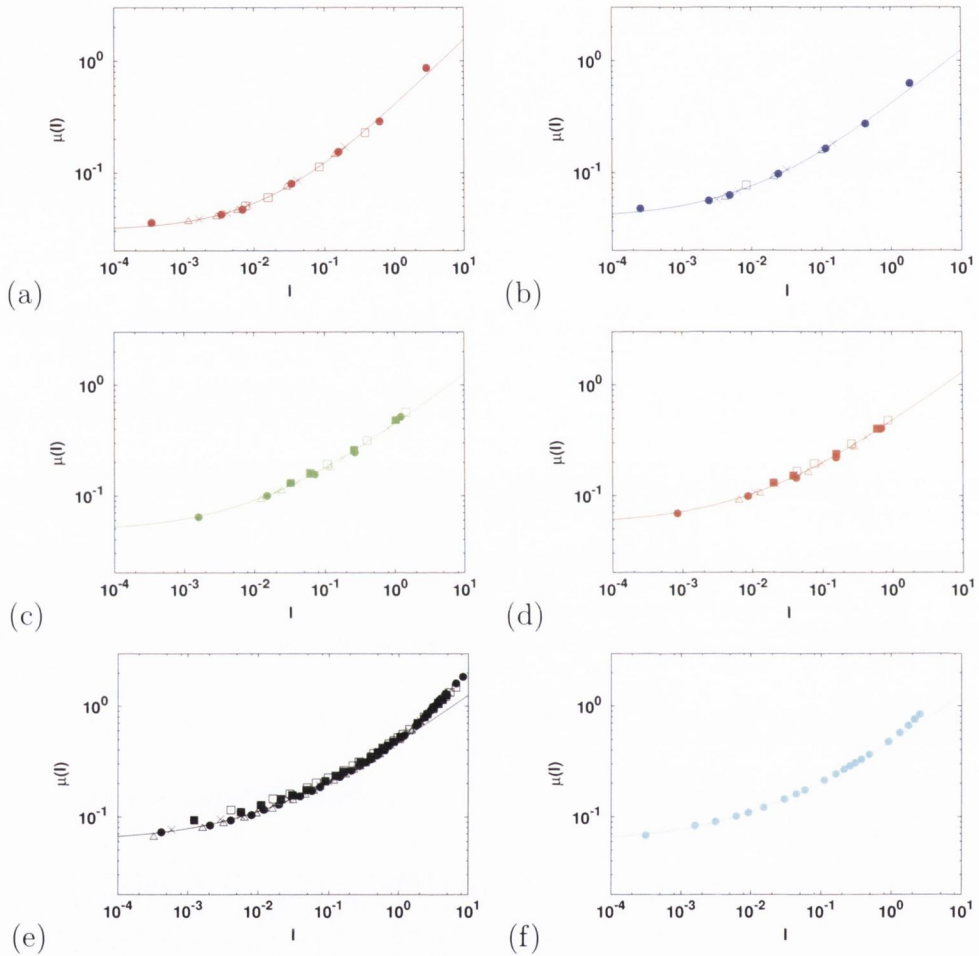


Figure 4.6: **Constitutive model collapses for six different channel widths.** We expand Figure 4.5, plotting each channel width as a separate subfigure: (a) $L = 2\langle d \rangle$; (b) $L = 4\langle d \rangle$; (c) $L = 8\langle d \rangle$; (d) $L = 16\langle d \rangle$; (e) $L = 33\langle d \rangle$; and (f) $L = 44\langle d \rangle$. Data for five different packing fractions are shown: $\phi = 0.85$, (\square); $\phi = 0.88$, (\blacksquare); $\phi = 0.92$, (\times); $\phi = 0.95$, (\bullet); $\phi = 0.98$, (\triangle). The solid lines show fits to Equation (4.1), for data up to $De = 2.0 \times 10^{-2}$, in line with our previous analysis (see Section 2.2).

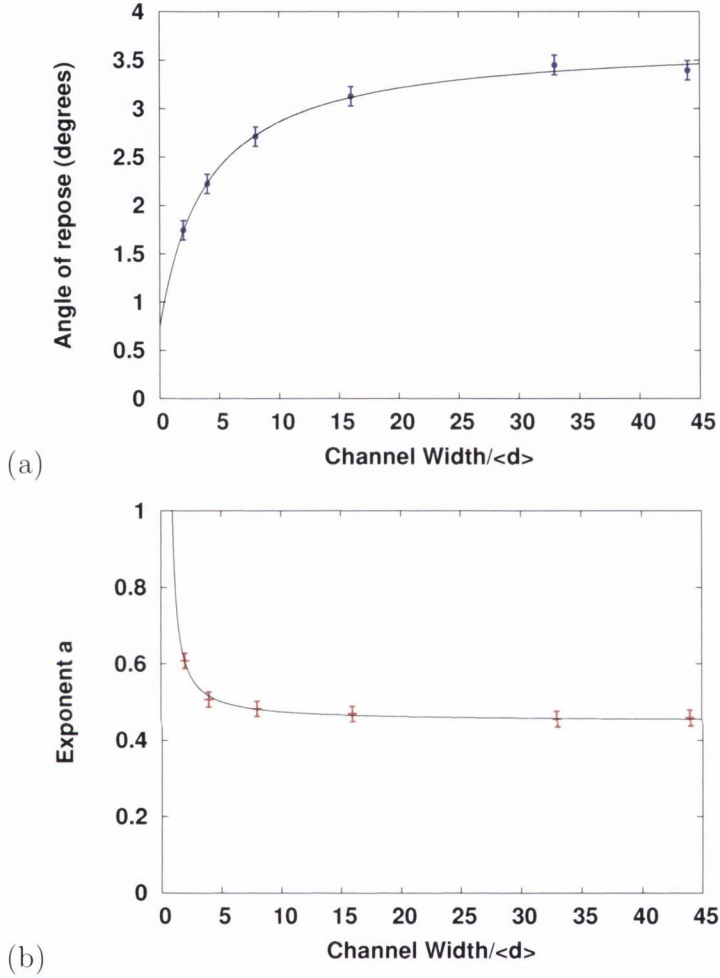


Figure 4.7: **Angle of repose and exponent a versus channel width.**

(a) Angle of repose versus L . The black line shows a fit to the empirical functional form $\alpha(L/\langle d \rangle) = \alpha_\infty + \frac{q}{L/\langle d \rangle + r}$, with $\alpha_\infty = 3.7 \pm 0.1$, $q = -11.6 \pm 0.1$ and $r = 3.9 \pm 0.1$. For narrow channels, the angle of repose is observed to decrease. As channel width L increases, we find from our fit α tends asymptotically to a value of $\alpha_\infty = 3.7 \pm 0.1^\circ$, lower than experimental and simulated values reported in the literature [30,92]. (b) Exponent a versus L . The black line shows a fit to the empirical functional form $f(x) = \frac{ux}{x-v}$, with $u = 0.449 \pm 0.003$ and $v = 0.51 \pm 0.02$. We find $a = u = 0.449 \pm 0.003$ in the asymptotic limit of infinite channel width L , similar to the experimental result of $a = 0.38$ found for foams [30]. As L decreases, a increases. From a simple scaling argument based on two bubble layers sliding past one another, we would expect $a(1) \approx 1$; we find $a(1) = 0.92 \pm 0.02$ from our fit.

Figure 2.10 (b), reproduced from [30], plots $\mu(I) - \mu^*$ for a range of channel thicknesses h , $2.5 < h/\langle d \rangle < 24$, collapsing well onto one master curve with $\mu^* = \tan(4.6 \pm 1^\circ)$, independent of system size.

For rotating drum experiments, see Figure 2.11 (b), our group has found finite size effects to *increase* the static angle of repose measured. This was supported by soft disk simulations modified to include a buoyancy term and a circular geometry, where the angle of repose was found to decrease towards $\alpha = 4.8 \pm 0.5^\circ$ as the system tended towards infinite size [93].

We suggest that these differences are likely due to the three different geometries studied. Lespiat *et al.* study a 3D pile of bubbles at the instant they begin to flow up a linear channel under the influence of buoyancy (Figure 1.14 (b)). The rotating drum's 2D circular geometry is markedly different due to the presence of curvature. Our simulations are different again, with the foam confined in a 2D linear geometry with no free surface. Our angle of repose is instead calculated from a ratio of forces on the boundaries - forces which, as we have seen in Figure 4.3, show different dependencies on channel width L .

4.2.2 The power law scaling exponent

In contrast to the collapse of the foam data over varying channel dimensions for one value of I exponent $a = 0.38$ found by Lespiat *et al.*, we find a range of values for a as a function of channel width L , shown in Figure 4.7 (b). We find the data to be well described by a fit to the empirical functional form $a(L/\langle d \rangle) = \frac{a_\infty x}{x + u}$, with $a_\infty = 0.449 \pm 0.003$ and $u = 0.51 \pm 0.02$, shown by the black line in Figure 4.7 (b).

In the limit $L/\langle d \rangle \rightarrow \infty$, $a(L/\langle d \rangle) \rightarrow a_\infty$. As for the angle of repose, from our fit we extrapolate the asymptotic value of exponent a in the limit of infinite channel width, finding $a_\infty = 0.449 \pm 0.003$.

For narrow channels, a is found to increase. We note that channel width in our model is defined as the perpendicular distance from the line of centres of the wall disks to line of centres of the lower wall disks. Therefore, channel width $L \approx 1\langle d \rangle$ would correspond to two walls sliding past one another, with no bulk bubbles between them. This is similar to the theoretical models of

bubble planes sliding past one another proposed by Princen [53] and Denkov *et al.* [22, 61], as introduced in Section 1.3. For our model's viscous interactions, this yields the scaling $\sigma \propto \dot{\gamma}$, as discussed in Section 3.4.2. Substituting this approximation into Equation (4.1), we obtain

$$\frac{\sigma}{\Pi} \sim k \left(\frac{c_d \dot{\gamma}}{\Pi} \right)^a \sim k (c_d)^a \left(\frac{\sigma}{\Pi} \right)^a. \quad (4.2)$$

From this, we would expect $a(L = 1\langle d \rangle) \approx 1$. Our fit finds $a(1) = \frac{0.449}{1-0.51} = 0.92 \pm 0.02$, in reasonable agreement with this simple scaling argument.

4.3 Conclusions and Outlook

We have seen that the boundaries in our system play an important role in the flow properties of our foam. For channels narrower than channel width $L \approx 30\langle d \rangle$, the shear stress is found to decrease, whilst the normal stress is found to increase. We explain this scaling behaviour by means of a simple model of foam confined to move in lanes in a narrow channel. Finally, we find the constitutive model to collapse data for a given value of L , but fail to collapse all data for all widths due to the effects of finite system size.

We investigate finite size effects specifically because our system contains rigid boundaries, similar to many experimental systems. A natural follow-up to this analysis would be to simulate the same systems, implementing Lees-Edwards boundary conditions [106], Figure 4.1. It would be interesting to investigate whether the tendency towards lane motion for narrow channels is a property of solid boundaries curtailing transverse motion, or whether it also arises in flow patterns that are periodic in the transverse direction, where the width of the repeated cell is small (as would be the case for Lees-Edwards conditions applied to our narrow channels).

Chapter 5

Stress Fluctuations

We have seen thus far that the complex behaviour of a system of interacting units (particles, agents), like the soft disk model, is often due to the nonlinear propagation of interactions between these units at the local level.

In this chapter, we now present a study of the global stress fluctuations in the soft disk model. We have seen in Chapter 2 that this model well describes the average flow properties of a foam under shear. In particular, it has been shown to reproduce the empirical Herschel-Bulkley relationship for the variation of the average value of the stress with strain rate for flowing foams [52, 77, 79, 81, 82], provided the simulation is in the low-strain rate regime and has not yet transitioned to laminar flow.

In experiments and simulations of flowing foams, often such average, steady-state values are the key quantities of interest. However, the character of fluctuations can provide additional information about the system. Indeed, we might expect to see evidence of the system's non-linearity in such fluctuations. Although, in general, far more focus has been placed in the literature on investigating the dependencies of foam properties via their means, these fluctuations have been studied for two-dimensional foams to a degree in the past.

We return to the origin of the soft disk model for the earliest of these studies. Durian examined the distribution of elastic energy changes occurring due to structural rearrangements [36]. He noted avalanche behaviour in the

disk rearrangements, and suggested power law scaling for small, negative elastic energy changes with an exponential cutoff at large energy changes.

Lauridsen *et al.* performed a similar analysis for experiments of two-dimensional flowing foams in a cylindrical Couette geometry, with similar results to Durian, but now for stress drops [23]. Dennin went on to look at the statistics of these stress drops. In particular, he measured the number of irreversible rearrangements (T1 events) in the foam and compared their occurrences to the variations of the shear stress with strain, noting a correlation between T1 events and stress changes [63].

In this chapter we look at the fluctuations of shear stress about the mean obtained for our simulations, at very low strain rate. Probability distribution functions of stress changes are found to show asymmetry between stress rises and falls, with fat tails for stress drops. We find the magnitude (or *volatility*) of stress changes to exhibit clustering, suggestive of long-memory processes (see Appendix E). Such long-range correlations are encountered in complex systems as diverse as economic markets [108, 109], online betting [110], seismology [111], and internet traffic [112].

Finally, we aim to expand upon the work of Durian, Lauridsen *et al.* and Dennin, relating fluctuations in the stress to changes in the topological structure of the foam in a novel, quantitative way. We use a rescaling method used in the econophysics community to analyse so-called microtrends in the data, and apply this to the analysis of contact changes of the bubbles as stress is built up and released [113]. This provides an alternative route to link dynamics at the bubble scale with the macroscopic response.

5.1 Simulation details and definitions

For the analysis we perform in this chapter, we once again use a soft disk model simulation, as described in Section 2.1. Here, we shall define the parameters of the simulation used for the results presented, and discuss the measurement of topological changes in the system as a function of time.

5.1.1 Soft disk model parameters

We shall, in the coming sections, examine the stress fluctuations in a system defined using the following parameters. The strain rate is set to be very low, with $De = 7.6 \times 10^{-6}$. This choice is motivated by our findings in Chapter 3: to study the nature of stress fluctuations and their link to bubble dynamics, we wish to maximise the non-affine motion. We also want to ensure that the characteristic rate of deformation does not overwhelm relaxation times associated with other processes in the system. Choosing a low strain rate accomplishes both of these aims. We note that at this strain rate the diffusion constant for the mean square displacements of the disks is linear with strain rate (see Figure 3.4), and the simulation approaches the quasistatic limit [82].

The system geometry studied here is the same as in Chapter 3, with packing fraction $\phi = 0.95$, $N = 1500$ bubbles in the bulk, $N_{\text{Wall}} = 80$ bubbles in the wall and a channel width of $L = 33\langle d \rangle$, i.e. we are measuring bulk properties, see Chapter 4. Much of the analysis we will perform in this chapter, particularly regarding the correlations in the system, benefits from large statistics. Consequently, data are taken in fine resolution over a total simulation run time, well past the initial transient regime and in the steady state, of $1 \times 10^6 \tau_v$.

5.1.2 Contact changes

In Chapter 3, we used non-affine displacements of the bubbles as a measure of local dynamics. In this chapter, we take a different approach to quantifying interactions on the bubble scale, by instead analysing topological changes in the foam.

In order to relate structural changes in the disk packing to changes in macroscopic properties such as shear stress, we measure the contact changes in the system, that is the number of neighbour changes over some time window $t_2 - t_1$.

We calculate these neighbour changes by generating a contact matrix, $C(t)$, for each simulation timestep. $C(t)$ is an $N \times N$ matrix, where N is the number of disks in the system. If disk i and disk j are in contact at time

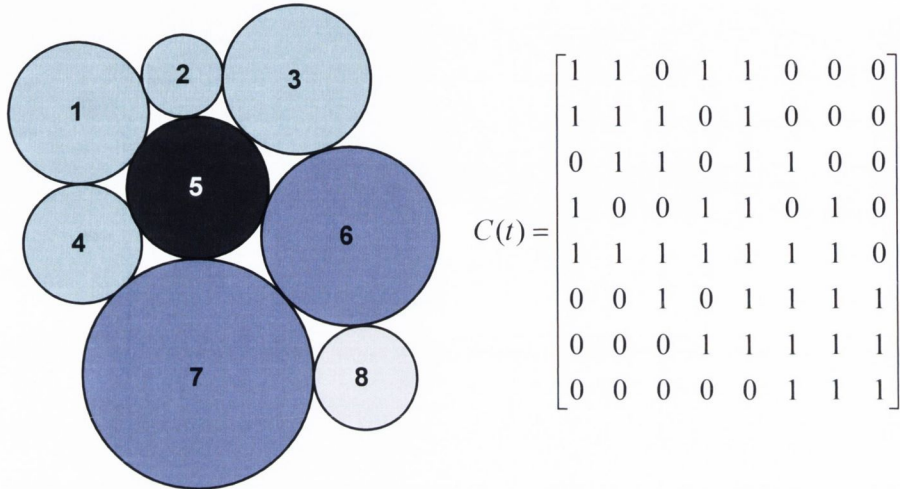


Figure 5.1: **The contact matrix.** A schematic representation of a small sample of disks in contact, with the corresponding contact matrix. Disks are coloured by their coordination number. By definition, the diagonal elements of $C(t)$ are always 1.

t , the corresponding matrix element $C_{ij}(t) = 1$. If they are not, $C_{ij}(t) = 0$. We define disks i and j as “in contact” numerically when their overlap Δ_{ij} , given by Equation (2.3), is greater than zero.

If disk i is in contact with disk j , then j is in contact with i . Consequently $C(t)$ is a symmetric matrix. From the definition we have chosen for contact, we note that a bubble will always be “in contact” with itself, and so the diagonal elements of $C(t)$ are always 1. Figure 5.1 shows a small sample system, with its corresponding contact matrix. The disks are coloured by their coordination number (i.e., their number of contacts).

By subtracting $C(t_1)$ from $C(t_2)$, summing the magnitude of the elements, and dividing by 2 for double counting, we calculate the number of contact

changes between times t_2 and t_1 as a measure of the topological change in the system.

5.2 Distribution of stress changes

Figure 5.2 (a) shows the shear stress, non-dimensionalised by the elastic modulus G_0 , plotted versus strain for a subsection of our data in the steady state. Note that for constant strain rate, strain is directly proportional to time. In Figure 5.2 (b), a zoomed image of the data shows the fluctuations about the mean stress.

We can immediately see that there exists a qualitative difference between increasing and decreasing trends. Stress rises at low strain rate generally have a slope close to the elastic modulus. This is consistent with the relationship for slow elastic loading of system, given by Equation (2.4), namely $\sigma = G_0\gamma$.

In contrast, the falls display steeper slopes and sparser point population. The points are evenly spaced in time, indicating more rapid drops in stress.

We investigate this by defining the *stress change*, $\Delta\sigma(t, \delta t)$, over time windows δt (expressed in terms of simulation timestep τ_v , as defined by Equation (2.8)) as:

$$\Delta\sigma(t, \delta t) = \sigma(t) - \sigma(t - \delta t). \quad (5.1)$$

We plot the probability distribution function of $\Delta\sigma(t, \delta t)$ in Figure 5.3.

For low values of $\delta t = 1.25 \times 10^2 \tau_v$, as shown in Figure 5.3, the PDF is asymmetric. Stress rises on average are more frequent and more narrowly distributed. The simple assumption that all rises have a slope of G_0 (based on Figure 5.2) would result in $\Delta\sigma/G_0 = \Delta\gamma = 0.00125$, for the parameters used in this simulation. This value lies close to the majority of points found, given the log scale, but there is some deviation from it. Deviation below this value is easily explained: any dissipative rearrangements should reduce the slope from $\sigma = G_0\gamma$. Values higher than this are relatively infrequent, although certainly not negligible, and attributed to the formation of temporary, unstable intermediate structures under shear.

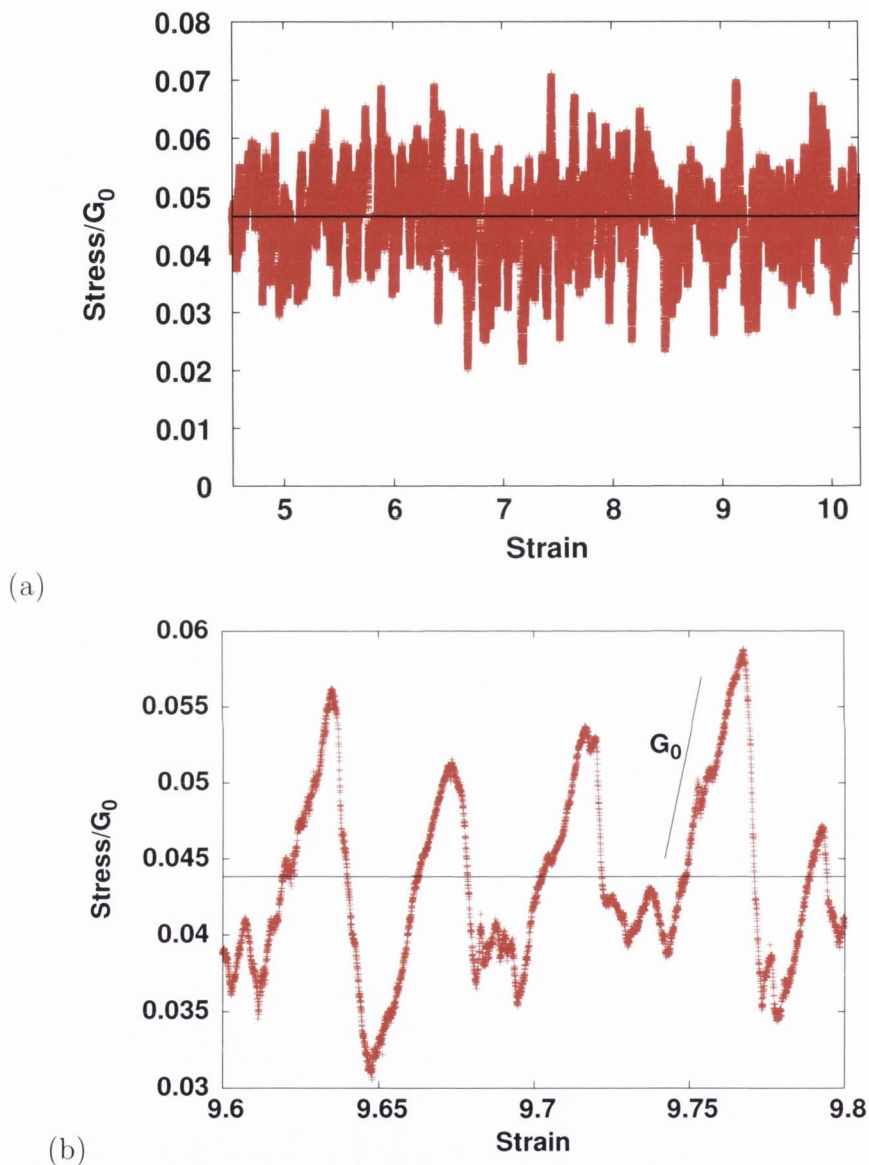


Figure 5.2: **Stress versus strain.** (a) Stress, non-dimensionalised by the static shear modulus G_0 , versus strain for low strain rate $De = 7.6 \times 10^{-6}$. (b) Magnified display of stress versus strain for a small subset of the data. The measured stress fluctuates about an average steady state value, marked by the horizontal black line in both images. Stress rises generally have a slope close to the elastic modulus G_0 , shown as a guide to the eye in (b), consistent with slow, elastic loading. Stress falls occur more rapidly, as may be seen by the lower density of data points.

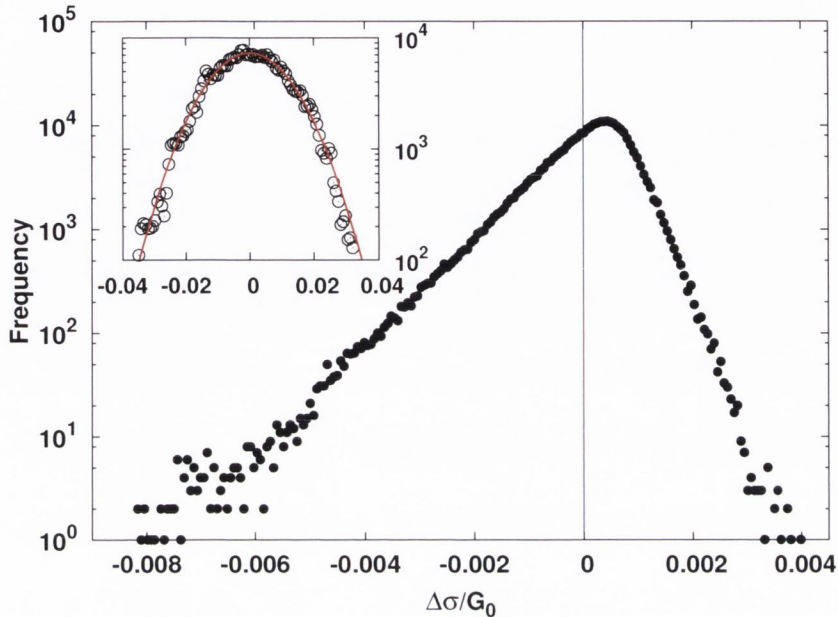


Figure 5.3: **Probability distribution of stress changes.** Distribution of stress changes $\Delta\sigma = \sigma(t) - \sigma(t - \delta t)$, for $\delta t = 1.25 \times 10^2 \tau_v$. The distribution is asymmetric. The stress rises are more narrowly distributed, whilst the stress falls exhibit fat tails. The simple assumption that all rises have a slope of G_0 would result in $\Delta\sigma/G_0 = \Delta\gamma = 0.00125$, for the parameters used in this simulation. The inset shows the distribution of stress changes for a larger value of $\delta t = 2 \times 10^4 \tau_v$. In this case δt is sufficiently large that $\sigma(t)$ and $\sigma(t - \delta t)$ are uncorrelated, recovering a Gaussian distribution (solid line).

Stress falls are found to exhibit fat tails, associated with avalanche-like behaviour and similar to the results of Durian [36] in simulation and Lauridsen *et al.* in experiment [23].

The choice of time window δt is important. Figure 5.3 (inset) shows the distribution for $\delta t = 2 \times 10^4 \tau_v$, sufficiently large that the changes in stress are statistically uncorrelated, leading to a Gaussian distribution. Likewise, for a choice of δt that is too small (eg. of the order of the simulation timestep $\tau_s = 2.5 \times 10^{-3} \tau_v$) the distribution is dominated by numerical noise and a Gaussian distribution is again recovered.

This asymmetry has not been shown before, for the soft disk model. We shall return to a discussion of the origin of this asymmetry in Section 5.4.

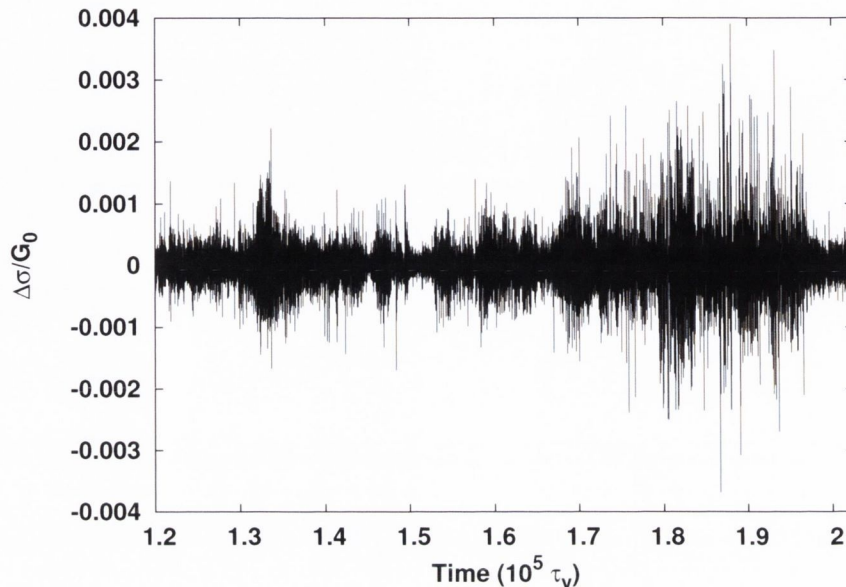


Figure 5.4: **Volatility clustering in stress changes.** Changes in stress, $\Delta\sigma$, versus time, for $\delta t = 7.5\tau_v$. Fluctuations are within slowly varying envelopes, with large changes tending to follow large changes, and small changes tending to follow small changes. Such so-called *volatility clustering* is a property of long-memory processes [108, 114].

5.3 Power-law correlations in the soft disk model

In this section, we show stress fluctuations in the soft disk model to exhibit so-called *volatility clustering* and long-range correlations. We expand on these terms in detail in Appendix E. We then compare them with similar scaling observed in the econophysics literature, where these phenomena are commonly studied, as motivation for subsequent analytical methods employed.

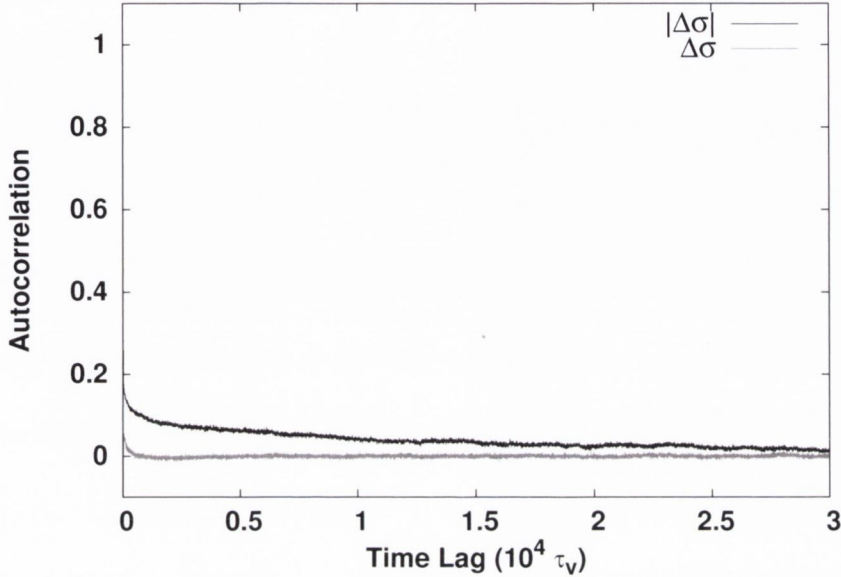


Figure 5.5: **Autocorrelation of stress changes.** Autocorrelation, $A(\tau)$, of stress changes, $\Delta\sigma$, and stress change volatility, $|\Delta\sigma|$ versus time lag τ . While $A(\tau)$ decays rapidly to zero for $\Delta\sigma$, for $|\Delta\sigma|$ the decay is much slower.

5.3.1 Volatility clustering and long-range memory

For a given choice of δt , the stress change $\Delta\sigma(t, \delta t)$ yields a timeseries, which we plot in terms of τ_v in Figure 5.4. Here, we choose $\delta t = 7.5\tau_v$. The stress changes display clear volatility clustering (see Appendix E), with fluctuations occurring within slowly varying envelopes. Large changes in stress tend to follow large changes, and small changes tend to follow small changes.

Volatility clustering is a well-known property of long-memory processes, where the autocorrelation function $A(\tau)$ of some timeseries $x(t)$

$$A(\tau) = \frac{\langle (x(t) - \mu)(x(t + \tau) - \mu) \rangle}{\Sigma^2} \quad (5.2)$$

with $\mu = \langle x(t) \rangle$ and $\Sigma^2 = \langle (x(t) - \mu)^2 \rangle$, varies as

$$A(\tau) \sim \tau^{-\beta} \quad \text{for } \tau \rightarrow \infty, \quad 0 < \beta < 1, \quad (5.3)$$

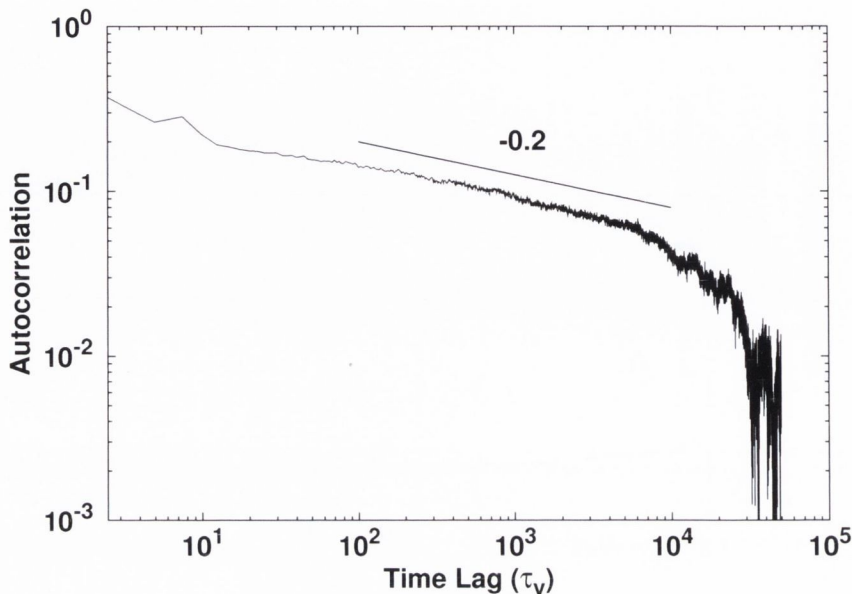


Figure 5.6: **Long memory in the autocorrelation of stress change volatility.** The autocorrelation of $|\Delta\sigma|$ on a log scale is found to vary as $A(\tau) \sim \tau^{-0.2}$ over two decades, similar to the long-memory scaling exponent found for the S&P 500 financial market in econophysics literature [115].

where τ is the time lag [108, 114], see also Appendix E.

Figure 5.5 shows the autocorrelation functions of stress changes, $\Delta\sigma$, and stress change volatility, $|\Delta\sigma|$, versus τ , for $\delta t = 7.5\tau_v$. For $\Delta\sigma$ (grey curve), the autocorrelation decays rapidly to zero, showing the stress changes to be uncorrelated. In contrast, $|\Delta\sigma|$ (black curve) decays much more slowly.

We can see this long-memory clearly by plotting the autocorrelation of $|\Delta\sigma|$ on a log-log scale, shown in Figure 5.6. $|\Delta\sigma|$ varies as $A(\tau) \sim \tau^{-0.2}$ over more than two decades. The autocorrelation function is subject to finite size errors when τ is no longer small with respect to the length of the timeseries. We compute the autocorrelation up to a time lag $\tau = 5 \times 10^4 \tau_v$, approximately 5% of the total simulation time.

We also estimate the Hurst exponent for both $\Delta\sigma$ and $|\Delta\sigma|$, see Appendix E. For $\Delta\sigma$ we find $H = 0.54$, close to the value of 0.5 expected for a random walk. For $|\Delta\sigma|$ we find $H = 0.89$, consistent with long memory.

What does this tell us about the system? We show a quantitative characterisation of the timescale within the system over which it evolves. Although in doing so one risks a common pitfall with correlation and causation, it is not unreasonable to infer, given our additional knowledge of the system, that large magnitude drops in shear stress tend to induce further large magnitude drops over relatively long periods of time.

5.3.2 Comparison with a different complex system: the Dow Jones Index

In the previous section, we have shown that volatility clustering and long-memory are to be found in the fluctuations of the shear stress in the soft disk model. This is the first time this has been shown for foam rheology. However, these properties are heavily studied in the literature for other complex systems, such as financial markets [108, 116] and in information transfer across computer networks [117]. In econophysics and the study of *log price returns* particularly, long-memory is the subject of extensive analysis and debate. Anything that might provide predictive power in the realm of stock market prices is much sought after, despite theories such as the efficient market hypothesis arguing that such advantages should be impossible [118].

The log-price returns are a measure of the fractional change in the price of an asset, defined as

$$x(t', \delta t') = \ln \frac{s(t' + \delta t')}{s(t')}, \quad (5.4)$$

where $s(t')$ is the price as a function of time t' , and $\delta t'$ the period over which the return is calculated. To remove the long-term increasing trend in stock market values, the logarithm of price changes is taken, ensuring Equation (5.4) fluctuates about a constant mean (zero). These log price returns are analogous to our stress changes $\Delta\sigma(t, \delta t)$.

In econophysics literature, the autocorrelation function of log-price returns decays exponentially, whilst the volatility of log-price returns exhibits long memory scaling with a similar exponent to our model [109, 113, 115].

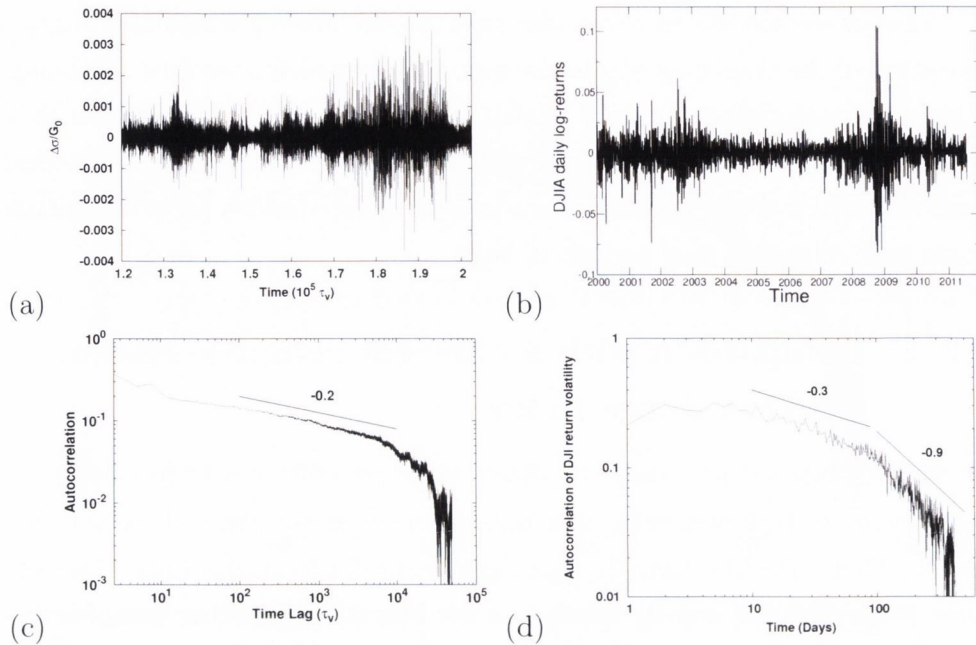


Figure 5.7: **Long memory scaling in shear stress and log price returns.** (a) $\Delta\sigma$ versus time, from the soft disk model. (b) $x(t, 1 \text{ day})$ versus time, for the Dow Jones Index (1993-2012). In both (a) and (b), we can see similar volatility clustering. (c) Autocorrelation $R(\tau)$ of $\Delta\sigma$ versus τ . (d) Autocorrelation $R(\tau)$ of $x(t, 1 \text{ day})$ versus τ . Long-range memory with a similar exponent ($\beta = 0.2$ for stress changes, $\beta = 0.3$ for daily returns from the Dow Jones Index [109], and $\beta = 0.2$ for minute-by-minute returns for the S&P 500 [115]) is observed for both volatility in stress changes, and volatility in log price returns.

In Figure 5.7 we compare log price returns and the autocorrelation of their volatility to the stress data we have shown in Figures 5.4 and 5.6. On the left, Figure 5.7 (a) and (c), we show the volatility clustering and power law scaling of the autocorrelation for stress changes from our model. On the right, Figure 5.7 (b) and (d), we show similar clustering and a similar scaling of the autocorrelation function for daily log price return data for the Dow Jones Index, over the period 1993 to 2012, from the Tickwrite database [119]. Visually, the resemblance is striking, and the similarities have motivated our analysis in the coming section and the next chapter.

We have also estimated the Hurst exponent for the Dow Jones Index (1993-2012). For the returns $r(t', 1\text{min})$, $H = 0.51$, whilst for the volatility of the returns $|x(t', 1\text{min})|$ we find $H = 0.87$. Again, this is consistent with uncorrelated values for $x(t', 1\text{min})$, with long memory behaviour in the volatility $|x(t', 1\text{min})|$, and very similar to our stress change data from Section 5.3.1. There is some variation of H reported in the literature for the Dow Jones Index, as it has been shown to depend on the range of years considered due to changes in trading frequency with technology [120]. Our estimated values are broadly consistent with similar studies [121, 122].

The physical origin of long-range memory processes and volatility clustering is widely debated in the literature [123]. Heterogeneity in time scales (for instance, rates of information arrival in financial markets, or the balance between long-term investors and short-term traders) has been suggested as a possible mechanism for the generation of such processes [124].

Multiple timescales also feature in our simulations of flowing foam. They include inertial, viscous and shear timescales, and timescales associated with disk rearrangements and swirling, vortex-like motion (as shown in Figure 3.1). Long memory could be due to the aggregation of processes with different timescales [125].

5.4 Stress fluctuations and topological changes

In Section 5.2, we saw asymmetry in the distributions of stress changes $\Delta\sigma(t, \delta t)$, for low δt . In Section 5.3.1, we saw that stress change volatility, $|\Delta\sigma(t, \delta t)|$, displayed clustering and long-range memory similar to well-known behaviour of log price returns in financial data. Motivated by this similarity, in this section we compare the asymmetric stress rises and falls using a rescaling analysis first applied to S&P 500 stock market data by Preis and Stanley [113]. In doing so, we relate topological changes in the foam to fluctuations in the macroscopic stress.

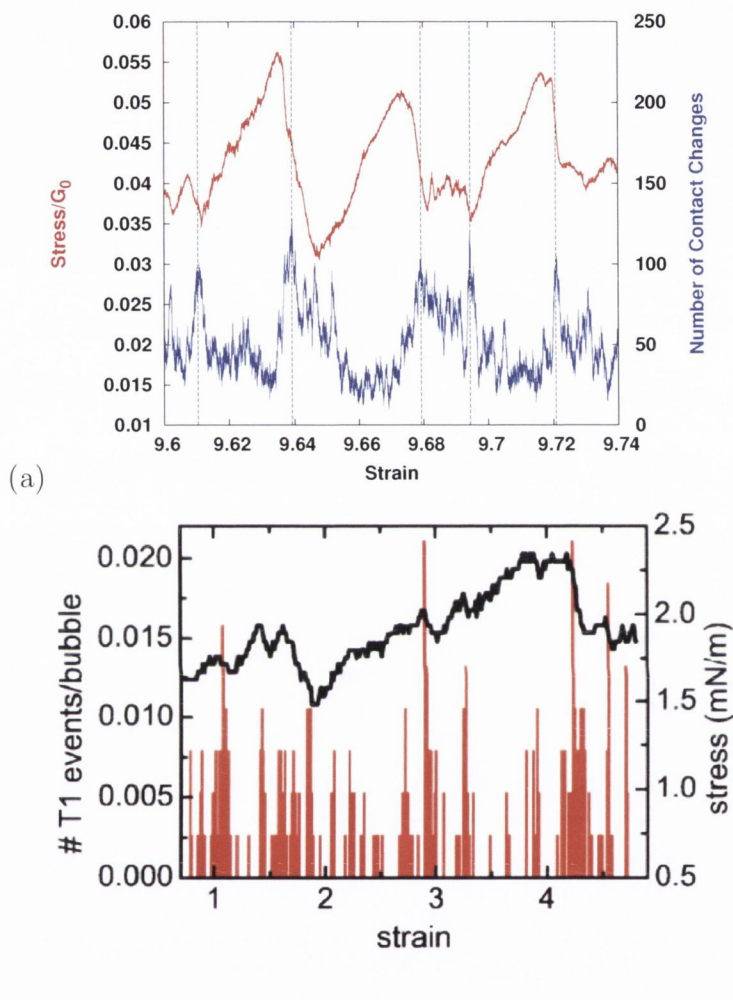


Figure 5.8: **Structural changes versus shear stress, in simulation and experiment.** (a) Stress/ G_0 versus strain (top, red), and contact changes versus strain (bottom, blue) over a time interval of $3 \times 10^2 \tau_v$. Local maxima in the contact changes are observed to align with corresponding falling trends in the shear stress. Some of these alignments are highlighted by the vertical dashed lines. (b) T1 transitions compared with shear stress in experiments carried out by Dennin, reproduced from [23]. In our simulations and in Dennin's experiments, qualitative correlations between topological changes and stress falls are observed.

As we mentioned in the introduction to this chapter, this has been studied before, qualitatively, in experiment by Lauridsen *et al.* [23]. We observe analogous behaviour in simulation too. Figure 5.8 (a) shows stress versus strain, and contact changes versus strain, as defined in Section 5.1.2. The time window over which the contact changes are calculated is $3 \times 10^2 \tau_v$. Vertical dashed lines highlight local maxima in the number of contact changes. These align well with falls in the stress, showing the dissipation of energy due to irreversible rearrangements. We reproduce Dennin’s experimental findings for T1 transitions [63] in Figure 5.8 (b), noting the agreement of our results with his findings.

The aim of this rescaling is to improve on these qualitative results, which we achieve by implementing a more quantitative analysis of these structural changes with respect to fluctuations in the stress, statistically comparing all trends.

5.4.1 Preis and Stanley rescaling method

In their paper “*Switching phenomenon in a system with no switches*” [113], Preis and Stanley attack a key question in the analysis of log price returns, common to our results from the soft disk model: what causes an upward trend to suddenly “switch” to a downward trend, and *vice versa*? To do this, they wish to compare what they call “microtrends” in their data - regions of rising (or falling) returns. Such microtrends can occur over different times, and can have different magnitudes, similar to stress rises and falls in our data. The challenge, then, is to quantitatively compare these trends with one another.

Preis and Stanley compare these rises and falls using a rescaling argument, first applied to S&P 500 stock market data [113], and which we shall apply to our stress changes in the next section. By finding a rescaled time with which they could collapse the trends, they could then apply the same collapse to other time-dependent properties of the system in order to examine their variations as a function of relative position within a microtrend.

We outline their analytical method as we have implemented it, in terms of shear stress, as follows.

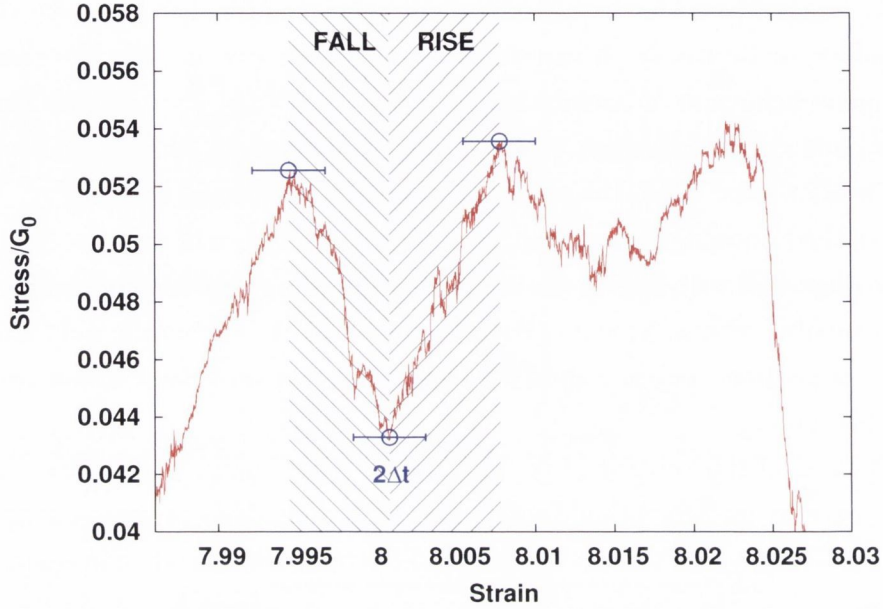


Figure 5.9: **Rescaling stress microtrends.** Local maxima and minima are located using a moving window of width $2\Delta t$. The three circles mark a local minimum and two local maxima, respectively. A *trend* is said to be the series of values for stress between each local minimum and successive maximum, for rises, and vice versa, for falls. Time t (directly proportional to strain) is rescaled to $\epsilon(t)$, via Equations (5.7) and (5.8), such that each trend starts at $\epsilon = 0$ and ends at $\epsilon = 1$.

A value of the shear stress as a function of time, $\sigma(t)$, is defined to be a local maximum, $\sigma_{max}(t, \Delta t)$, if there is no higher value of stress within the interval $t - \Delta t \leq t \leq t + \Delta t$ (Figure 5.9). Thus

$$\sigma_{max}(t, \Delta t) = \max\{\sigma(t) | t - \Delta t \leq t \leq t + \Delta t\}, \quad (5.5)$$

and analogously

$$\sigma_{min}(t, \Delta t) = \min\{\sigma(t) | t - \Delta t \leq t \leq t + \Delta t\}. \quad (5.6)$$

Following Preis and Stanley we now introduce a renormalised timescale, ϵ , between alternating pairs of local maxima and minima, as follows: let t_{min} and t_{max} be the times at which a local minimum and a successive local

maximum occur. If $t_{min} < t_{max}$, the microtrend is defined as a *rise*; if $t_{max} < t_{min}$, the microtrend is defined as a *fall*. The rescaled time ϵ is given by

$$\epsilon(t) \equiv \frac{t - t_{min}}{t_{max} - t_{min}} \quad (5.7)$$

for a stress rise, and

$$\epsilon(t) \equiv \frac{t - t_{max}}{t_{max} - t_{min}} \quad (5.8)$$

for a stress fall.

Defining ϵ in this way scales all stress microtrends to the same time interval, $\epsilon \in [0, 1]$. We now apply this time rescaling to the time-dependent contact changes $C(t)$. This enables us to monitor structural rearrangements of our disks, which are the cause of stress fluctuations, as they occur within a trend, allowing averaging over all rises and falls in the data irrespective of the individual magnitudes and durations of trends.

5.4.2 Application to stress fluctuations

Figure 5.10 (b) plots contact changes versus rescaled time ϵ , see Equations (5.7) and (5.8). The scatter data are the contact changes for all trends. The average and standard deviation of the scatter data are overplotted, showing a clear correlation between structural rearrangements and relative position within a rise or fall.

During the rises, after an initial period of large numbers of contact changes, the curve levels out, consistent with a picture of slow elastic loading involving few structural rearrangements. Surprisingly, the maximum number of contact changes tends to occur not at the beginning of a fall, as might be expected, but instead towards the end of the fall. The derivative of contact changes is maximum at the boundaries between rising and falling trends. This could suggest that at the beginning of a stress fall, the system becomes unstable and undergoes rearrangements to reduce its energy, but does not immediately reach the lowest energy state. Although many of the disks

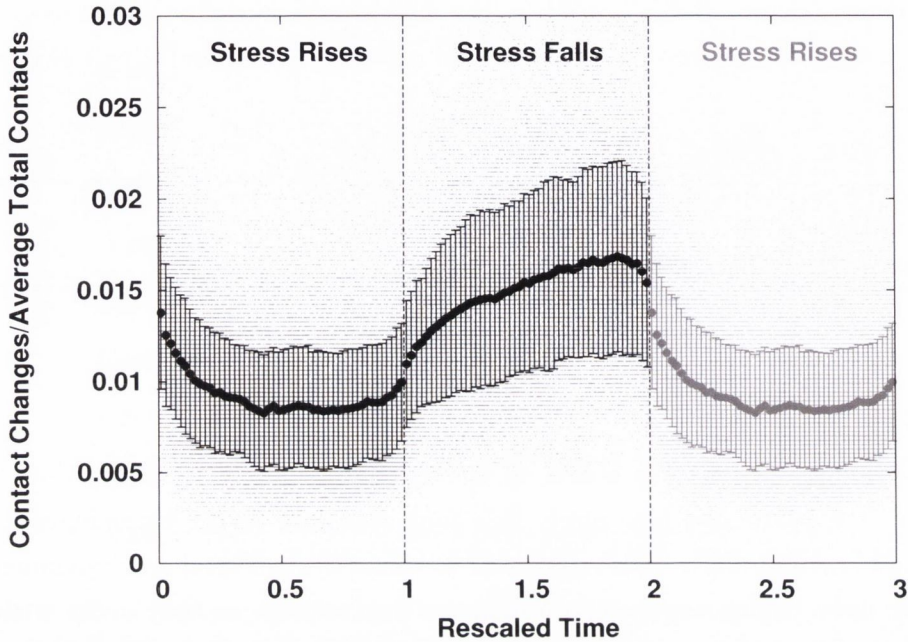


Figure 5.10: **Contact changes versus rescaled time ϵ .** The contact changes are calculated over a time interval of $3 \times 10^2 \tau_v$, and normalised by the average total number of contacts, N_{total} , computed from the data. $N_{\text{total}} = 4145$, corresponding to an average contact number of 5.15 per disk. The data from [1:2] corresponds to fall data, offset by 1 to align the beginning of the fall data with the end of the rise data. The data from [0:1] and [2:3] are identical, shown for illustrative purposes. The overlaid points, with error bars, shows the mean and standard deviation of the scatter data respectively.

might have succeeded in reaching a more relaxed configuration, regions of “trapped” stresses may still remain. Thus, the system tends to undergo a series of further rearrangements, seen at the beginning of the rises, as these disks are “shuffled” by the shearing boundary and the trapped stresses are released.

5.5 Conclusions and Outlook

The non-linearity in the soft disk model arises from irreversible structural rearrangements as the disk packing is sheared. Previous simulation work has

shown power-law scaling and avalanche-like behaviour in stress drops [36], and in experiments Dennin has qualitatively linked structural rearrangements (i.e. T1 transitions) to changes in the shear stress [63]. We successfully expand upon this work, showing asymmetric distributions for shear stress changes over short times, consistent with two distinct mechanisms: slow elastic loading as the stress increases, and rapid, dissipative rearrangements as the stress decreases.

We utilise a rescaling argument from econophysics literature to quantify, for the first time, structural rearrangements in a foam under shear as a function of position within these stress rises and falls. This analysis supports the previous hypothesis of two distinct mechanisms for rises and falls, linking them directly to changes in topology. Few contact changes occur during the majority of the rises, as we expect for an elastic loading mechanism. We find that the highest number of contact changes occur, not at the beginning, but towards the end of the falls, consistent with a picture of a few initial rearrangements rapidly propagating throughout the system.

We note that the average number of contact changes in rises and falls can vary by as much as a factor of 2. This is not a small relative variation, and could potentially have a bearing on theories of foam flow based on bubble rearrangement rates, such as fluidity models, where such rearrangement rates are often taken as approximately constant [95].

Furthermore, we show for the first time that the magnitude of stress changes displays clustering in time and long-range memory, similar to properties found for price fluctuations in financial markets [109]. Several key differences exist, however, between these price fluctuations and the stress fluctuations obtained from the soft disk model. Firstly, the price returns in financial data are not in a steady state. Secondly, log-price returns display symmetric distributions, unlike the stress changes in our model. Finally, our simulations have explicit local interactions and a well-defined driving force applied at one boundary. Nevertheless, the soft disk model features some of the complex dynamics and emergent behaviour seen in financial market data, and gives hope that detailed knowledge of trader interactions is not needed to understand key features of stock data. We note that the soft disk model

is an example of one of many similar models, widely used in the study of - among others - foams [13], suspensions [126], granular media [127] and soil mechanics [128]. Although designed for specific purposes, such models might offer insights into the mechanisms of complexity in fields beyond those for which they were initially conceived.

Chapter 6

Generalised Diffusion and the Fokker-Planck Equation

In the previous chapter, we have seen that our simulations displayed some of the statistical properties and long-memory scaling familiar from the study of econophysics, but previously unobserved in the study of foam rheology. Motivated by this, we successfully applied a rescaling argument developed for the analysis of stock market returns in the econophysics literature to our shear stress fluctuations. We now ask, can we also extend a more general analysis, which we originally developed for financial data, to our foam data?

When introducing the nature of financial markets, it is usual to outline the character of the probability distribution function for log price returns and the autocorrelation functions for the log price returns and the square of the log price returns. These are then discussed separately. The probability distribution function for log price returns exhibits fat tails with a power law exponent of the order of 4 [115, 116, 129].

The normalised autocorrelation function is essentially zero for log price returns after a short time of the order of a few minutes [115, 116, 130]. The autocorrelation function for the volatility (or magnitude) of the log price returns also falls away from its value at zero time but then exhibits a slowly decaying, long-memory region, suggesting the presence of correlations extending to times of the order of a few weeks [115, 116, 131–133].

In developing models, most emphasis has focused on the probability distribution function, perhaps because it has an immediate impact on the calculation of risk via the detailed character of the fat tails [134, 135]. Less emphasis has been placed on the calculation of expressions for the autocorrelation functions. Yet, using the basic framework of statistical physics, it can be shown that the correlation functions and the distribution functions are complementary facets of the basic Fokker-Planck equations that describe the underlying dynamics [136–138]. So from the one basic approach it should be possible to compute not just the probability distribution function but also the correlation functions. The implication of this statement is that the parameters that characterize the distribution function are related to those characterizing the correlation functions.

In Section 6.1, we present a generalised model for relating the normalised autocorrelation function $R(\tau)$ (see Appendix E) to the temporal evolution of the distribution of a random variable, via generalised diffusion coefficients.

In Section 6.2, we apply this model to the log price returns for the Dow Jones Index (1993-2012), linking the fat-tailed return distributions to long-memory in the autocorrelation of the return volatility. Finally, we return to the fat-tailed PDFs we found for mean square displacements in Chapter 3. In Section 6.3, we present an initial attempt to use the same generalised model to relate these strongly non-affine dynamics to long-memory in the soft disk model.

6.1 Generalised diffusion model

We shall now derive a generalised diffusion model, relating correlations in a time-dependent variable to the temporal evolution of the variable's distribution. In theory, this approach is valid for any time-dependent process provided one has a functional form for the variable's distribution.

6.1.1 The Fokker-Planck equation

The normalised autocorrelation function $R(\tau)$, is defined as a function of time-lag τ by

$$R(\tau) = (G(\tau) - \langle x(t) \rangle^2) / \sigma_t^2, \quad (6.1)$$

with

$$G(\tau) = \langle x(t)x(t+\tau) \rangle = \lim_{T \rightarrow \infty} \int_0^T x(t)x(t+\tau) dt, \quad (6.2)$$

and $\sigma_t = \sqrt{\langle x^2(t) \rangle - \langle x(t) \rangle^2}$.

The temporal evolution of the average of some function $M(x, t)$ of a random variable $x(t)$ is described by

$$\frac{d\langle M(x, t) \rangle}{dt} = \left\langle \frac{\partial M}{\partial t} \right\rangle + \sum_{n=1}^{\infty} \left\langle D_n(x, t) \frac{\partial M(x)}{\partial x^n} \right\rangle, \quad (6.3)$$

where $D_n(x, t)$ are the generalised n-th order diffusion coefficients [139]. $D_n(x, t)$ is given by

$$D_n(x, t) = \frac{1}{n!} \lim_{\Delta t \rightarrow 0} \frac{\langle [x(t + \Delta t) - x(t)]^n \rangle_{x(t)=x}}{\Delta t}. \quad (6.4)$$

For both financial data and for the soft disk model, our time-dependent variables measure a *change* in value over a certain time-window δt , as a function of the “global” time t . For financial data, this describes the log price returns $x(t, \delta t) = \log(\frac{S(t+\delta t)}{S(t)})$. For our foam simulations, this describes both the change in stress $\Delta\sigma(t, \delta t)$ (Equation (5.1)) and the transverse displacements $\Delta s_y(t, \delta t)$. We incorporate this dependency of a choice of time window, or lag, by extending Equation (6.4) to

$$D_n(x, t) = \frac{1}{n!} \lim_{\Delta t \rightarrow 0} \frac{\langle [x(t + \Delta t, \delta t) - x(t, \delta t)]^n \rangle_{x(t, \delta t)=x}}{\Delta t}. \quad (6.5)$$

The generalised Fokker-Planck equation relates the distribution of the variable $x(t)$ to the diffusion constants [139] via

$$\frac{\partial p(x, t)}{\partial t} = \sum_{n=1}^{\infty} (-1)^n \left(\frac{\partial^n}{\partial x^n} \right) [D_n(x, t)p(x, t)]. \quad (6.6)$$

If we know a suitable form for $p(x, t)$ and how it varies in time, we can calculate time dependent diffusion coefficients and thus calculate how the autocorrelations scale in time via Equation (6.3).

Choosing $M = x$, Equation (6.3) gives

$$\frac{d \langle x \rangle_{x(t=0)=x_0}}{dt} = \langle D_1(x, t) \rangle. \quad (6.7)$$

Note that in the above equation and in the theoretical discussion that follows we have used t to refer to the time-window or time-lag, previously called δt , in order to simplify the notation. $\langle x(t) \rangle$ corresponds to the unnormalized correlation function $G(t)$ (see Equation (6.2)), i.e.

$$G(t) = \langle x(0)x(0+t) \rangle = x_0 \langle x(t) \rangle_{x(t=0)=x_0} \quad (6.8)$$

Choosing $M = x^2$ gives

$$\frac{d \langle x^2 \rangle}{dt} = 2 \langle x D_1(x, t) \rangle + 2 \langle D_2(x, t) \rangle. \quad (6.9)$$

If one determines how $D_1(x, t)$ and $D_2(x, t)$ vary with x and t , one can then attempt to solve Equations (6.7) and (6.9) for $\langle x \rangle$ and $\langle x^2 \rangle$, respectively. This in turn yields the scaling of the autocorrelation functions for the linear and squared returns with time, via Equation (6.2) [139].

6.1.2 The choice of probability distribution function

The probability density function of log-price returns has been described [109, 136–138] using the form

$$p(x, t) = \frac{1}{Z(t)} \left[1 + \frac{\beta(t)x^2}{\alpha} \right]^{-\alpha}. \quad (6.10)$$

$Z(t)$ and $\beta(t)$ are two functions via which we try to capture the time dependence of $p(x, t)$. The nature of this distribution is such that in the limit $\beta x^2/\alpha \rightarrow 0$ it reduces to a Gaussian distribution function. For such a distribution, the variance $\sigma^2(t)$ is given

$$\begin{aligned} \sigma^2(t) &= \langle x^2(t) \rangle = \int dx p(x, t) x^2 \\ &= \frac{\alpha}{\beta(t)} \frac{\int \frac{z^2 dz}{(1+z^2)^\alpha}}{\int \frac{dz}{(1+z^2)^\alpha}} = \begin{cases} \infty & \text{if } \alpha < 3/2 \\ \frac{\alpha}{(2\alpha-3)\beta(t)} & \text{if } \alpha > 3/2. \end{cases} \end{aligned} \quad (6.11)$$

Here, we exploit another similarity between the behaviour of log-price returns and the fluctuations in the soft disk model. The form of distribution in Equation (6.10) yields fat-tails for short times, and (provided either β , x or both decay at long time) tends to a Gaussian in long time. Such a distribution captures the behaviour of the mean square displacements we found in Chapter 3. We return to this in Section 6.3.

In order to proceed, we now need more detailed information regarding the scaling of D_1 and D_2 . For this, we must forgo generality and turn our attention to the first application of the model, to Dow Jones Index log-price returns.

6.2 Application to Dow Jones financial data

In this section we shall first complete our theoretical model, taking into account results for the functional form of the diffusion constants known for financial data. We shall then present results from the application of the model to Dow Jones minute by minute data, 1993-2012, taken from the Tickwrite 6 database (over 1.7 million data points) [119].

6.2.1 Inserting D_1 and D_2 for log-returns.

For a moment, let us simplify the argument and assume that D_1 and D_2 are independent of time, in line with the analysis of Queiros *et al.* [136]. Linear and quadratic relationships for $D_1(x)$ and $D_2(x)$, of the form

$$D_1(x, 1\text{min}) = -2\kappa DCx \quad (6.12)$$

and

$$D_2(x, 1\text{min}) = D(1 + Cx^2), \quad (6.13)$$

where κ , D and C are constants, have been shown to hold for daily data [136]. $D_1(x, 1\text{min})$ and $D_2(x, 1\text{min})$ are thus related via

$$D_1(x) = -\kappa dD_2(x)/dx. \quad (6.14)$$

We show in the next section that these relationships hold for our minute-by-minute Dow Jones data.

The problem with a time independent diffusion constant D_2 is that it essentially leads to an exponential decay of the volatility with time, which does not reflect empirical data. We shall thus introduce a time dependence in the coefficients, but continue, in line with the literature [109, 136] and our own findings (Section 6.2.2), to assume that $D_1(x, t)$ and $D_2(x, t)$ are linear and quadratic in x , respectively. We now have

$$D_1(x, t) = -b(t)x, \quad (6.15)$$

and,

$$D_2(x, t) = D(t) \left(1 + \frac{\beta(t)x^2}{\alpha} \right), \quad (6.16)$$

including the terms $b(t)$ and $D(t)$ of yet unspecified forms.

At this state we will assume Equation (6.14) still holds. This immediately results in

$$b(t) = 2\kappa \frac{D(t)\beta(t)}{\alpha}. \quad (6.17)$$

We assume that $D(t)$ is dependent only on $\beta(t)$ raised to some power γ , viz:

$$D(t) = D(\beta(t)) = D_0\beta^\gamma(t), \quad (6.18)$$

where D_0 is constant, leading to $b(t) = \frac{2\kappa D_0}{\alpha}\beta^{\gamma+1}$. Using this ansatz we obtain the solution

$$\beta^{-(\gamma+1)} = \beta_0^{-(\gamma+1)} + \frac{4D_0(\alpha - 1 - \kappa)}{\alpha}(\gamma + 1)t, \quad (6.19)$$

leading to the scaling

$$\beta(t) \propto t^{-\frac{1}{\gamma+1}} \quad \text{and hence} \quad D(t) \propto t^{-\frac{\gamma}{\gamma+1}} \quad \text{and} \quad b(t) \propto t^{-1} \quad (6.20)$$

in the limit $t \rightarrow \infty$.

In the following section we see how the above results compare with empirical deductions from our Dow Jones data.

6.2.2 Results

Figure 6.1 (a) shows the probability distribution function for one minute log-price returns for the Dow Jones over the period 1993-2012. We have removed the mean (which is a very small correction for the data considered here, of the order of 10^{-4}), so that the distribution is centred around $x = 0$. The data is well described by the proposed probability function of Equation (6.10), with fitted power law exponent $\alpha = 1.84 \pm 0.04$. The tail exponent is thus $-2\alpha \simeq 3.7$, similar to values obtained for other datasets [115, 129]. Since the power law tail is most pronounced in the one-minute data, we keep it fixed in all the fits of log-price returns for different time windows, i.e. 10, 100 and 400 minutes, as shown in Figures 6.1 (b), (c) and (d).

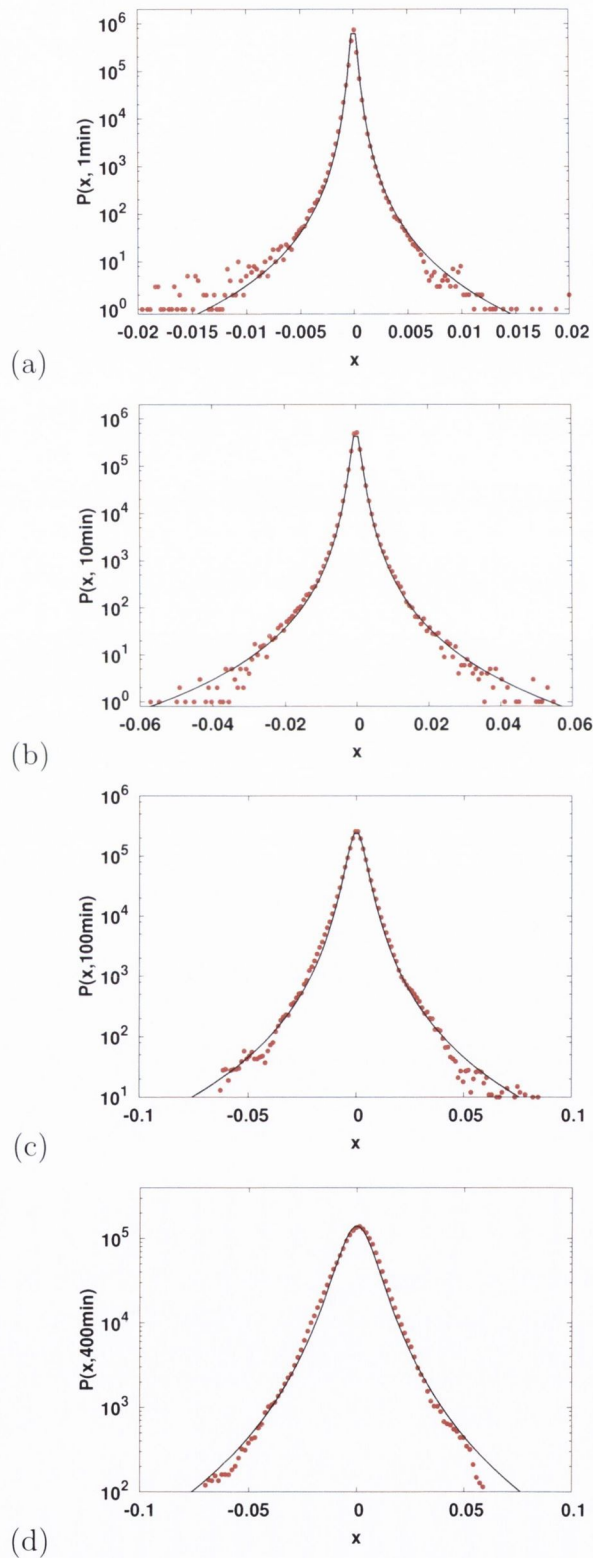


Figure 6.1: Plots of the probability density distribution for log price returns for time lags 1, 10, 100 and 400 minutes. The transition from a distribution with what appears to be a cusp to a Gaussian shape as time increases is clearly visible. The solid lines are fits to the probability function of Equation (6.10), resulting in an exponent $\alpha = 1.84 \pm 0.04$ (Dow Jones minute by minute data, 1993-2012, taken from the Tickwrite 6 database (over 1.7 million points)).

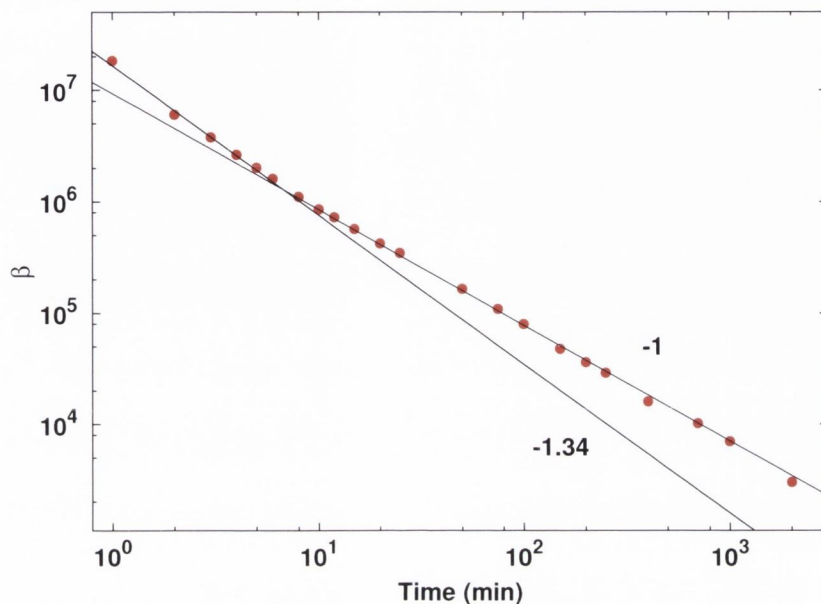


Figure 6.2: **Variation of β as a function of the time lag, for log-price returns.** The data is obtained from fits of the Dow Jones minute by minute data to the distribution function of Equation (6.10) as shown in Figure 6.1. For times less than about 10 minutes the data is well described by $\beta(t) \propto t^{-1.34}$ while for larger times $\beta(t)$ varies as t^{-1} . (Data shown on double logarithmic scale.)

Initial values of $Z(t)$ are obtained from reading off $P(0, t) = 1/Z(t)$ for the various time windows. We then perform a one free parameter fit to Equation (6.10) to obtain an initial guess for $\beta(t)$, followed by a two parameter fit to obtain final values for $Z(t)$ and $\beta(t)$. The resulting curve for $\beta(t)$ is shown in Figure 6.2 in a double-logarithmic plot.

The data is best described by two power-law regimes. For small times ($t < \sim 10$ min) β varies as $t^{-1.34}$, for larger times it varies as t^{-1} . Correspondingly we obtain from Equation (6.20) that for times up to about 10 minutes $\gamma \simeq -1/4$, while for larger times we have $\gamma = 0$.

Since the exponent $\alpha = 1.84$ of the probability distribution of log-returns exceeds $3/2$, we see from Equation (6.11) that $\sigma^2(t) \sim \beta^{-1}(t)$. For small times we thus obtain $\sigma^2(t) \sim t^{1.34}$, corresponding to a *super-diffusive* regime

(as introduced in Section 3.2.2), while for larger times $\sigma^2(t) \sim t$ and normal diffusion prevails, similar to results found for S&P 500 financial data [116].

We have also computed the generalised diffusion constants $D_1(x, t)$ and $D_2(x, t)$ for our Dow Jones (1993-2012) dataset, using the functional form of Equations (6.15) and (6.16), respectively. Figure 6.3 shows, as an example, $D_1(x, 1 \text{ min})$ and $D_2(x, 1 \text{ min})$. D_1 and D_2 evaluated for larger times show the same variation with x , albeit with different prefactors. Figure 6.4 shows that the pre-factor $b(t)$ is well described by $b(t) \propto t^{-1}$ over the range from 1 to 100 minutes. For larger time lags our data proved to be too noisy to allow for a meaningful comparison of b and β .

From fits to our data for $D_2(x, t)$ to Equation (6.16), we obtained the prefactor to the quadratic in x , i.e. $D(t)\beta(t)/\alpha$. Values of this fitted prefactor as a function of time are also shown in Figure 6.4. We see that the values scale like $b(t)$ and we can indeed overlay $b(t)$ and $\kappa D(t)\beta(t)/\alpha$ for a value of $\kappa = 1$, justifying Equation (6.17).

Let us return to the time interval from one to ten minutes, where β varies as $t^{-1.34}$ and thus $\gamma \simeq -0.25$. Interestingly we see that this corresponds to $\gamma \simeq -1/2\alpha$. In this regime we may then choose

$$D(t) = D_0 Z^{1/\alpha}(t). \quad (6.21)$$

This conjecture is consistent with the Fokker-Planck equation for the fluctuations being equivalent to a non-linear equation,

$$\frac{\partial P}{\partial t} = -\frac{\partial}{\partial x} D_1(x, t) P + D_0 \frac{\partial^2}{\partial x^2} P^{1-1/\alpha}. \quad (6.22)$$

This equation has been proposed by Gell-Mann and Tsallis in the context of non-extensive statistical mechanics [140]. By varying the parameter α , the equation has been found to fit probability distribution functions for a wide range of systems from science and economics.

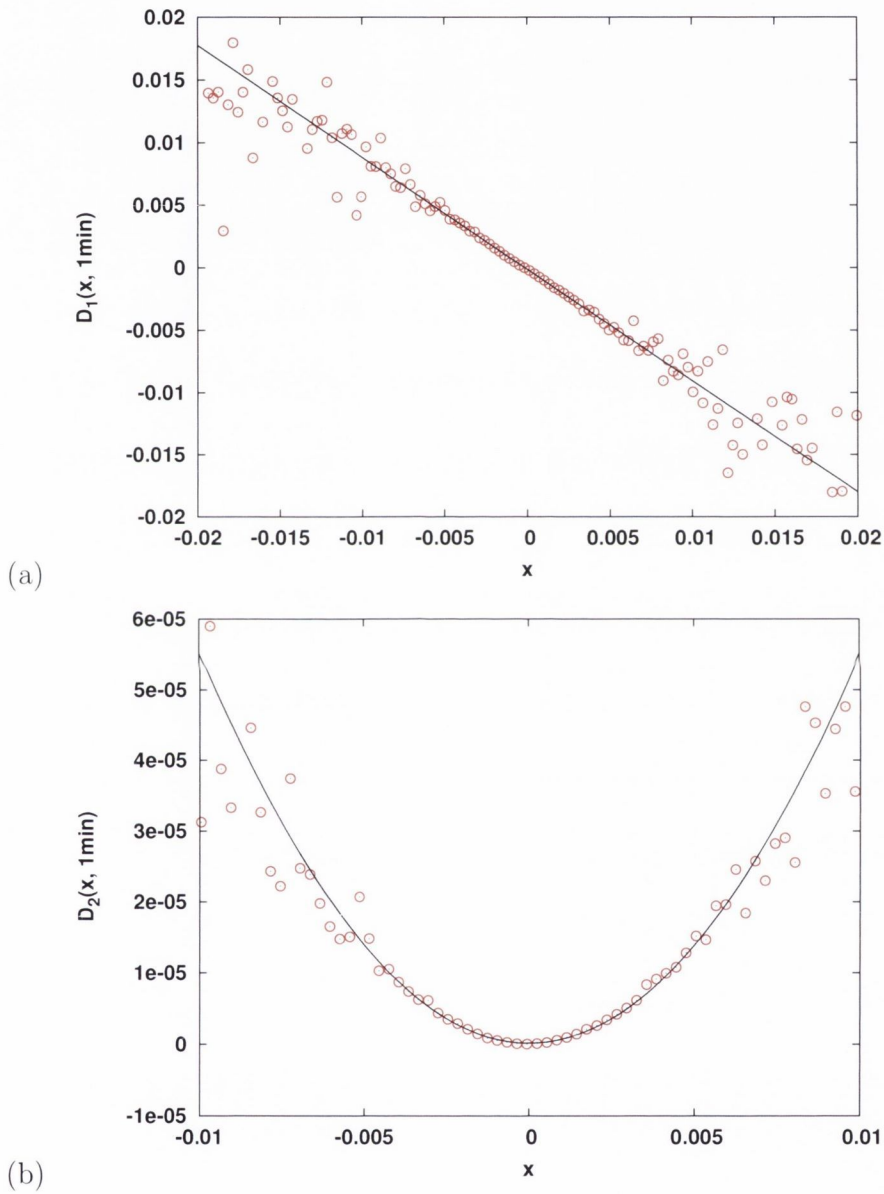


Figure 6.3: Generalized diffusion coefficients D_1 , (a), and D_2 , (b), computed from minute by minute Dow Jones data over the period 1993-2012. Lines are least-square fits to the data and suggest that D_1 is linear in the x coordinate (i.e. the log-return r) and D_2 is quadratic.

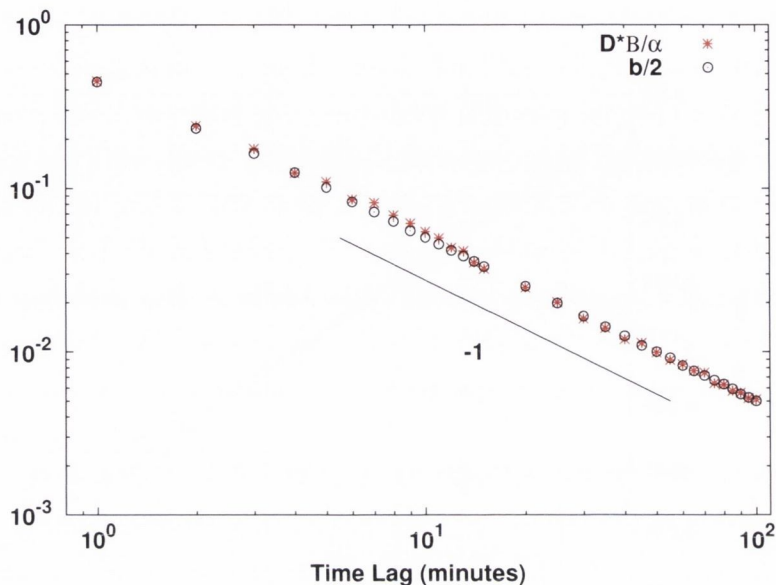


Figure 6.4: **Fit parameters for D_1 and D_2 versus time.** Empirical values for $b(t)/2$ obtained from fitting the generalised diffusion constants $D_1(x, t)$ to Equation (6.15). The data is well approximated by a power law with exponent -1. Also shown in this graph is the variation of the fitted prefactor of the quadratic in $D_2(x, t)$, i.e. $D\beta/\alpha$ at $t = 1$ minute. This graph thus justifies Equation (6.17).

Now let's return and look again at Equation (6.9) for the correlation function $\langle x^2 \rangle$ using the generalized diffusion coefficients defined by Equations (6.15) and (6.16) respectively. We have

$$\frac{d\langle x^2(t) \rangle_{x_0}}{dt} = 2D(t) \left(1 + \frac{\beta(t)}{\alpha} (1 - 2\kappa) \langle x^2(t) \rangle \right). \quad (6.23)$$

Assuming the power law expressions Equation (6.20) for $D(t)$ and $\beta(t)$ we have

$$\frac{d\langle x^2(t) \rangle_{x_0}}{dt} = 2D_0\beta(t)^\gamma \left(1 + \frac{\beta(t)}{\alpha} (1 - 2\kappa) \langle x^2(t) \rangle \right). \quad (6.24)$$

Let us first consider the regime $t > 10$ minutes, where $\gamma = 0$ and $\beta(t) = \beta_2 t^{-1}$, with $\beta_2 = \text{const.}$ This results in

$$\frac{d\langle x^2(t) \rangle_{x_0}}{dt} = 2D_0 \left(1 + \frac{\beta_2}{\alpha} (1 - 2\kappa) \langle x^2(t) \rangle t^{-1} \right). \quad (6.25)$$

The solution of this equation is given by

$$\begin{aligned} \langle x^2(t) \rangle_{x_0} &= \frac{G_{x^2}(t)}{x_0^2} = \\ &= \frac{2D_0}{1 - 2D_0 \frac{\beta_2}{\alpha} (1 - 2\kappa)} t + \text{const.} \times t^{2D_0 \frac{\beta_2}{\alpha} (1 - 2\kappa)}. \end{aligned} \quad (6.26)$$

But now we recall that the correlation function we actually require is $R_{x^2}(t)$, i.e. $R(t)$ of Equation (6.1), applied to x^2 . Noting that the non-conditional average $\langle x^2(t) \rangle^2 \simeq G_{x^2}(t)$ in the limit of $t \rightarrow \infty$, where the first term of the RHS of Equation (6.26) is the dominant term, we obtain

$$R_{x^2}(t) \simeq \text{const.} \times t^{2D_0 \frac{\beta_2}{\alpha} (1 - 2\kappa)}. \quad (6.27)$$

Recalling that $\kappa \simeq 1$, we find that $R_{x^2}(t)$ scales as $t^{-2D_0\beta_2/\alpha}$. The ratio $2D_0\beta_2/\alpha$ is obtained from our fits for $D_2(x, t)$, as it is twice the prefactor of the x^2 term at $t = 1$ minute (see Figure 6.4). We finally obtain

$$R_{x^2}(t) \propto t^{-0.9}, \quad (6.28)$$

in good agreement with our data, as shown in Figure 6.5.

We now recall our introduction of a time dependent function $D_1(x, t)$, see Equation (6.15). The time dependence of $b(t)$, $b(t) = b_1/t$, leads immediately to a power law for the autocorrelation function,

$$\langle x \rangle / x_0 = (t/t_0)^{-b_1}. \quad (6.29)$$

Figure 6.6 shows a one-parameter fit of this power law to our data for $t < 10$ minutes, using the value $b_1 = 0.89$, as obtained from our data for $b(t)$,

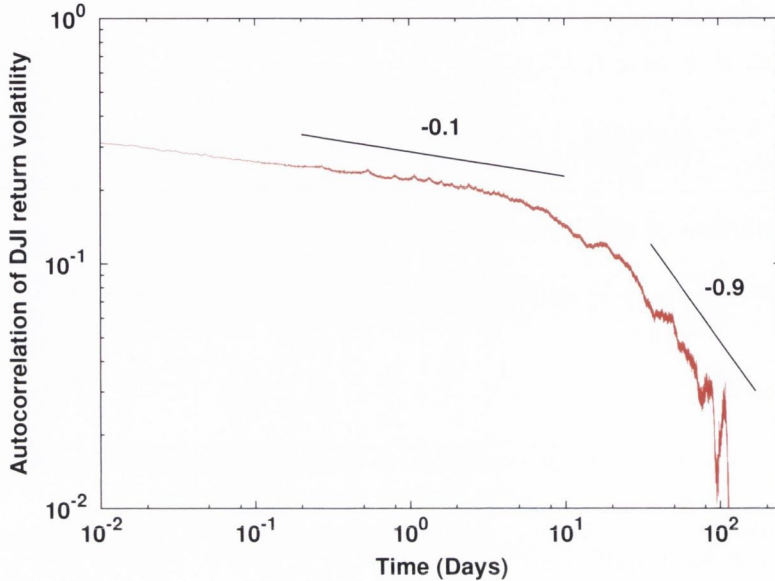


Figure 6.5: **Autocorrelation of the magnitude (volatility) of minute-by-minute DJIA log returns $|x(t, 1 \text{ min})|$ (data from 1993-2012), plotted on a log-log scale.** Power law regimes may be identified for the ranges of 0.1 to 10 days, and exceeding 30 days, with approximate exponents of -0.1 and -0.9 , respectively.

see Figure 6.4. We see that this approximation provides a not unreasonable empirical fit to the data.

6.3 Application to soft disk model simulations

In this section, we shall present some preliminary findings in applying our generalised diffusion model to our simulation results. The parameters used are identical to those outlined in Section 5.1.1.

First, we shall briefly discuss the choice of simulation parameter to analyse. Then, we shall show that our mean square displacement distributions from Chapter 3 are well described by the time-dependent functional form of Equation (6.10). From this, we calculate $\beta(t)$. Finally, we shall once again

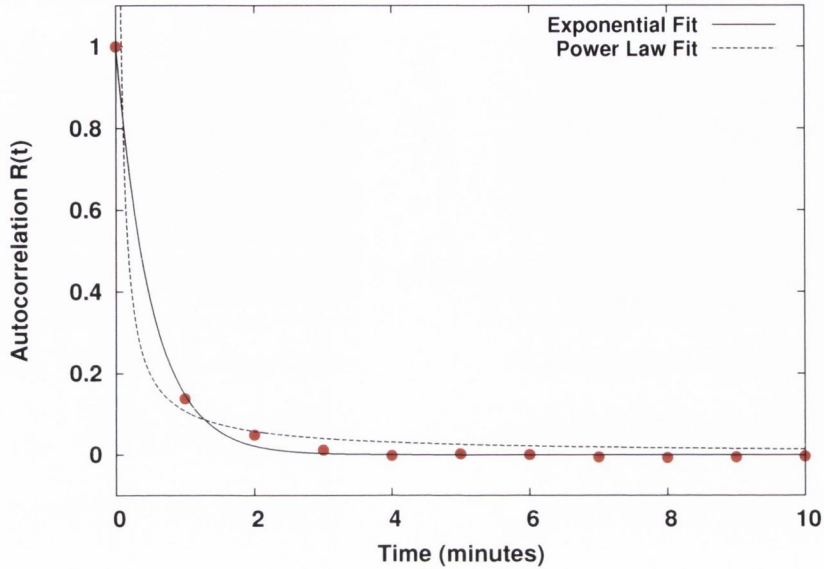


Figure 6.6: **Normalized autocorrelation function for minute-by-minute Dow Jones data over the period 1993-2012.** The solid line shows a fit to an exponential decay, with a decay constant of 31 seconds. The dashed line shows a one-parameter fit to $\langle x \rangle / x_0 = (t/t_0)^{-b_1}$ with b_1 fixed, $b_1 = 0.89$.

see long-memory in the soft disk model, this time in the bubble dynamics directly.

6.3.1 Choosing an analogy to log returns

Our initial motivation for applying a generalised diffusion model developed for financial data to our soft disk model simulations was exceedingly straightforward: we noted that log-price returns initially displayed fat tails, tending towards a Gaussian distribution at long time, and underwent diffusion. As we have seen in Chapter 3, transverse mean square displacements of disks under shear share all of these properties. We know from Chapter 5 that volatility clustering and long-range memory can be found in the model also.

This long-memory, however, was found for the stress changes. These are indeed related to this displacements, but almost certainly not trivially! In this section, we shall focus solely on displacements. The problem with this

choice, however, is in quantifying the behaviour of the displacements versus time in order to calculate the autocorrelation function. Each disk is described by its own position vector $\mathbf{r}(t')$, and thus has its own transverse displacement timeseries $\Delta s_y(t', t) = r_y(t' + t) - r_y(t')$. How do we consider the motion of all disks? Focusing on only a single disk will result in poor statistics. We cannot consider them sequentially, as this will result in spurious correlations of the order of the length of time sampled per disk, defeating the purpose.

In the correlation analysis that follows, we choose a simple average, that is we calculate the correlations for average transverse displacement $\langle \Delta s_y \rangle(t', t)$ over a time window t . This quantity is perhaps a naive choice, as it loses information when opposite motion in the system averages to zero. Nevertheless, we find it to capture enough information in the system for our initial analysis. In a sense, it is not too different from the Dow Jones Index; the index is itself a weighted average of 30 different stock fluctuations [141].

6.3.2 Mean square displacement distributions

We return now to the *mean square displacement distributions* from Section 3.2.1. Figure 6.7 shows distributions for $De = 7.6 \times 10^{-6}$, over time intervals t of (a) $2.5\tau_v$, (b) $125\tau_v$ and (c) $5000\tau_v$. The solid black lines show fits to the functional form of the distribution given by Equation (6.10). The exponent $\alpha = 1.75$ is calculated from (a), the finest resolution of data we have, and then kept constant for all t , in line with our analysis in Section 6.2.

We see that at low time lags, Equation (6.10) provides a good fit to the data. In Figure 6.7 (c), the displacements have begun to approach Gaussian distribution, as we begin to transition to the diffusive regime examined in Section 3.2.2. Equation (6.10) still provides a not-unreasonable fit to the majority of the data, considering that the logscale emphasises deviations at the tails.

From these fits to Equation (6.10), we find values for $\beta(t)$ for our soft disk simulations, shown in Figure 6.8 on a log-log scale. The solid line plots a fit to the data for power law scaling $\beta \sim t^{-\psi}$, with $\psi = 1.57$, which describes the data well over the range probed.

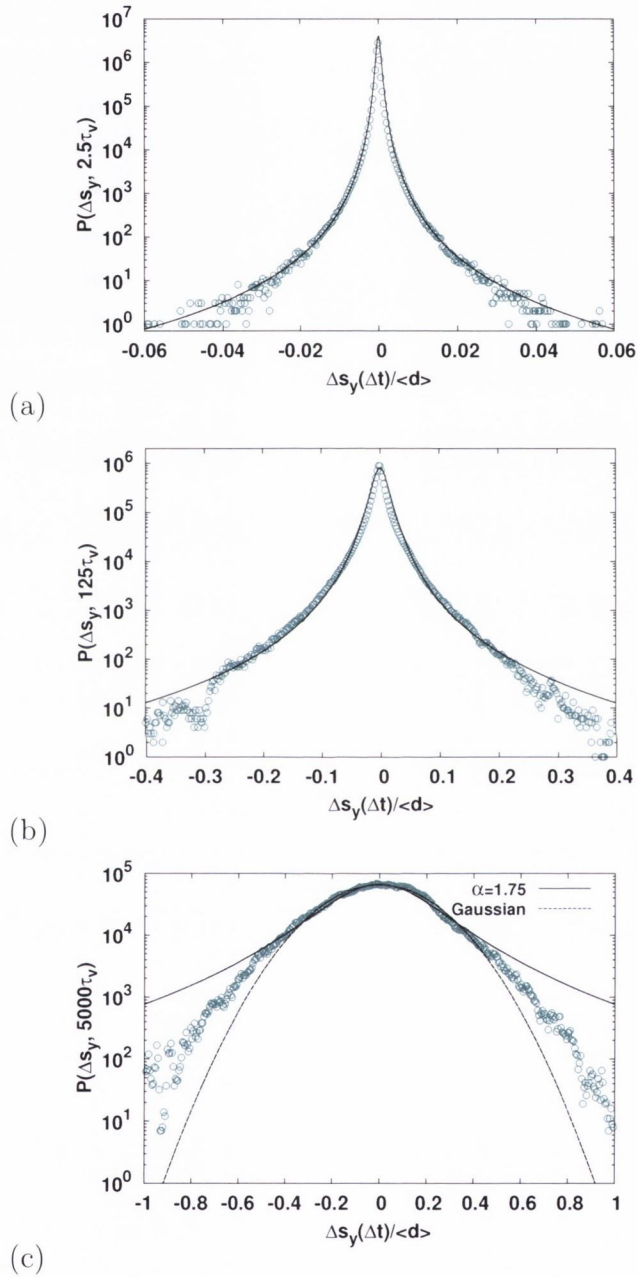


Figure 6.7: Plots of the probability density distribution for mean square displacements for $De = 7.6 \times 10^{-6}$ and time lags 2.5, 125, 5000 τ_v . The solid lines are fits to the probability function of Equation (6.10), resulting in an exponent $\alpha = 1.75 \pm 0.03$. At long time lags, the distribution tends towards a Gaussian distribution, shown by the dashed line in (c).

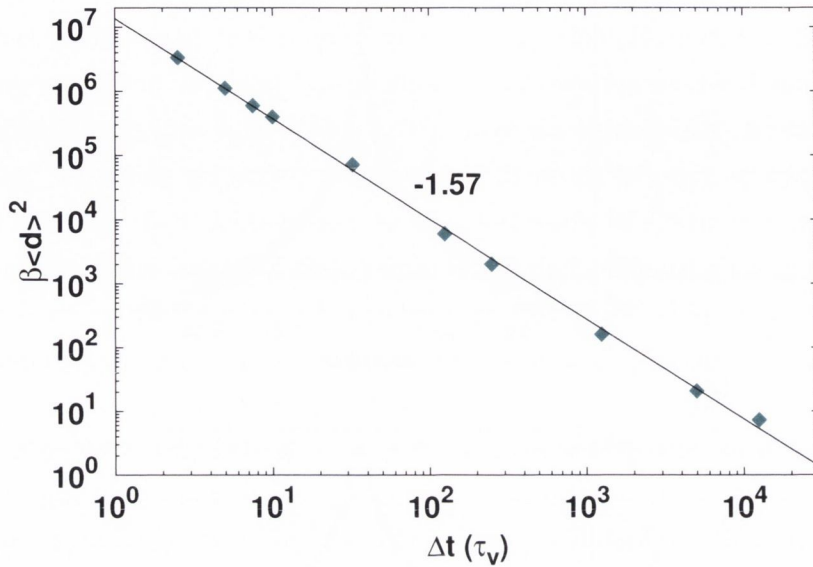


Figure 6.8: **Variation of β as a function of the time lag for mean square displacements.** The data is obtained from fits of the mean square displacements to the distribution function of Equation (6.10) as shown in Figure 6.7. We plot $\beta \langle d^2 \rangle$ in order to non-dimensionalise our results, equivalent to considering mean square displacements $\Delta s / \langle d \rangle$. The solid line plots a fit to the data for power law scaling $\beta \sim t^{-\psi}$, with $\psi = 1.57$. This corresponds to superdiffusive scaling over the entire range of the data shown. The highest time lag shown, $t = 12500\tau_v$, is approximately the point where the tails of the displacements become well-described by a Gaussian distribution.

This value of ψ corresponds to superdiffusive scaling over the entire range of the data shown. This is consistent with the superdiffusive regime we had previously observed in 3.2.1. The highest time lag shown, $t = 12500\tau_v$, is approximately the point where the tails of the displacements become well-described by a Gaussian distribution, i.e. the onset of the diffusive regime.

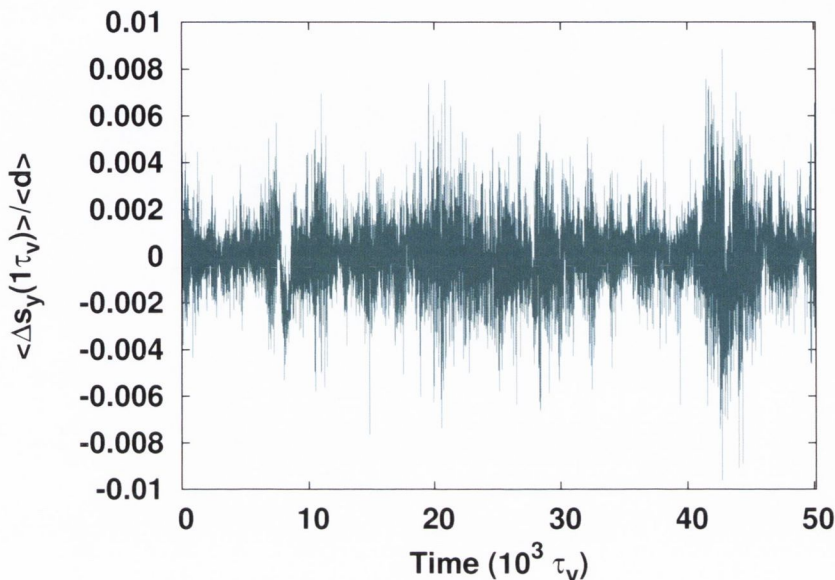


Figure 6.9: **Volatility clustering in the average transverse displacement versus time.** Average transverse displacement $\langle \Delta s_y(\Delta t) \rangle$ for $\Delta t = 1\tau_v$, versus time, for $De = 7.6 \times 10^{-6}$. Average displacements calculated, as in Chapter 3, for bubbles whose y-coordinates fall within $0.2L < y < 0.8L$, i.e. away from the boundaries. We see volatility clustering, similar to clustering seen for shear stress fluctuations in the soft disk model and log price returns in the Dow Jones Index, as shown in Figures 5.7 (b) and (d) respectively.

6.3.3 Volatility clustering and long-range memory in displacements

We now consider the *average transverse displacement* $\langle \Delta s_y \rangle(t', t)$, introduced in Section 6.3.1. Similarly to previous analysis, we wish to avoid the effects of the boundaries on the transverse displacements. Therefore, $\langle \Delta s_y \rangle$ is calculated, as in Section 3.2.1, for bubbles whose y-coordinates fall within $0.2L < y < 0.8L$, where L is the channel width.

Figure 6.9 plots $\langle \Delta s_y \rangle$ versus time t' , for a time lag $t = 2.5\tau_v$. We observe volatility clustering, similar to clustering seen for shear stress fluctuations in the soft disk model and log price returns in the Dow Jones Index, as shown in Figures 5.7 (b) and (d) respectively. As expected, the average value of $\langle \Delta s_y \rangle$

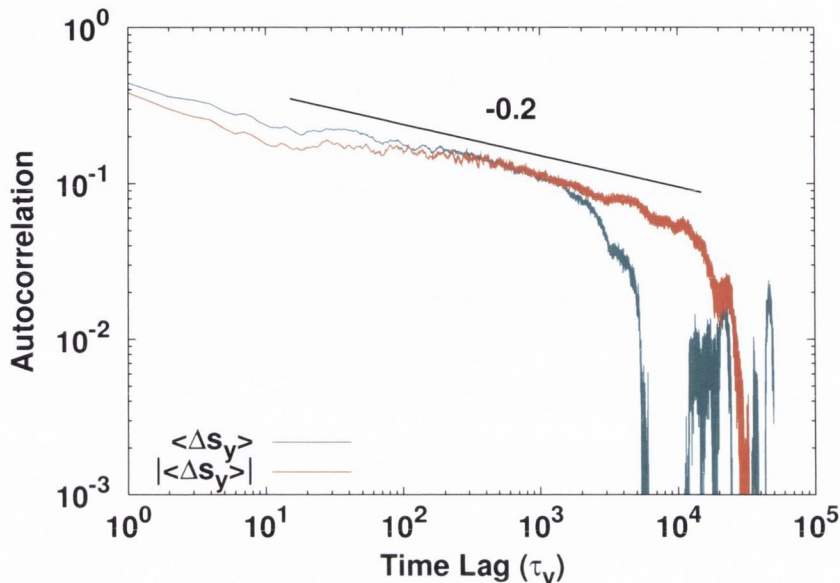


Figure 6.10: **Autocorrelations of the average transverse displacement and magnitude (volatility) of the average transverse displacement** The autocorrelation of $\langle \Delta s_y \rangle$ (teal) is observed to decay more rapidly than the autocorrelation of its magnitude, $|\langle \Delta s_y \rangle|$ (orange). The solid line provides a guide to the eye for long-memory scaling $A(t) \propto t^{-0.2}$, which is clearly seen to describe the scaling of $|\langle \Delta s_y \rangle|$ well over nearly three decades. The autocorrelation of $|\langle \Delta s_y \rangle|$ then sharply decays to zero, at a value of time $t \sim 1 \times 10^4$ consistent with the onset of Gaussian distributions and normal diffusion.

is zero, because the mean transverse flow is zero. The fluctuations at such a short time scale are small, of the order of less than one percent of a bubble diameter. We probe longer time scales using the autocorrelation function.

In Figure 6.10 we plot the normalised autocorrelation function for the average transverse displacement $\langle \Delta s_y \rangle$ (teal), and the volatility (or magnitude) of the average transverse displacement $|\langle \Delta s_y \rangle|$ (orange). We observe that, similar to the effect of considering the volatility on long-range memory that we have already seen in both stress fluctuations and log-price returns, the volatility $|\langle \Delta s_y \rangle|$ decays more slowly than $\langle \Delta s_y \rangle$. $|\langle \Delta s_y \rangle|$ is well described

by power law scaling with an exponent of -0.2 over nearly three decades, shown by the solid black line as a guide to the eye in Figure 6.10.

The Hurst exponent (see Appendix E) for $\langle \Delta s_y \rangle$ is estimated to be $H = 0.93$. For $|\langle \Delta s_y \rangle|$, we find a value of $H = 0.97$. As one might expect from Figure 6.10, both values are consistent with the long memory condition $0.5 < H < 1.0$.

The Hurst exponents highlight a key difference we have found for the average transverse displacement in comparison with the results for stress changes and log price returns. We compare these values in Table 6.1. We find that $\langle \Delta s_y \rangle$, unlike $\Delta \sigma$ and $x(t, 1\text{min})$, does not decay rapidly to zero in an exponential-like fashion, instead itself displaying long memory that is merely amplified by considering the autocorrelation of its magnitude.

What this implies is, unlike for stress or log-returns, if we know that we have a **positive** average transverse displacement at some time τ , then we know that it is probable that we shall have another **positive** displacement at $\tau + \delta\tau$, some short time $\delta\tau$ later. Naively, one could attribute this to a bias inherent in the quantity we have chosen to look at, namely the simple average transverse displacement. At short timescales, of the order of τ_v , if the average motion is in one direction, it is very likely that the average motion will continue (although it will probably slow down) in that direction for some finite time. Put another way, the average velocity is a continuous function. In contrast, both stress and log-returns can conceivably have discontinuities. In the case of the former, this can occur when bubbles lose contact with one another. In the case of the latter, price choices are discrete. A more quantitative analysis of this is necessary.

Nevertheless, we can extract some interesting information from even this preliminary analysis. The autocorrelation function of $|\langle \Delta s_y \rangle|$ no longer shows long-memory, instead decaying rapidly to zero, at a time lag of approximately $t \sim 1 \times 10^4 \tau_v$. As we have seen in Figures 6.7 and 6.8, this corresponds to the onset of shear induced diffusion, identifying perhaps another method of classifying when a system has reached the diffusive regime, in complement to our method shown in Figure 3.6.

System	Hurst exponent	Hurst exponent, volatility
Stress changes, $\Delta\sigma$	0.54	0.89
Log price returns, $x(t, 1\text{min})$	0.51	0.87
Average displacement, $\langle\Delta s_y\rangle$	0.93	0.97

Table 6.1: **Hurst exponents for stress changes, log-price returns and average transverse displacement.** Stress changes and log-returns show similar behaviour, with the $H \sim 0.5$ for $\Delta\sigma$ and $x(t, 1\text{min})$ indicating uncorrelated timeseries. When computed for their volatilities, $|\Delta\sigma|$ and $|x(t, 1\text{min})|$, long-memory emerges, with $H = 0.89$ and $H = 0.87$ respectively. For $\langle\Delta s_y\rangle$, long memory is observed for both the unmodified timeseries, and its volatility.

From our results for both log-returns and mean square displacements we see that long-memory is associated with fat-tailed distributions, a result supported by the literature [109, 116, 142]. This is potentially of relevance to understanding the origin of long-memory in the stress fluctuations shown in Figure 5.6, noting that we observed fat-tailed distributions for stress falls in Figure 5.3.

6.4 Conclusions and Outlook

We present a general model for relating the scaling of the normalised auto-correlation function for a time-dependent variable to the temporal evolution of distributions of that variable, via generalised diffusion coefficients and the Fokker-Planck equation.

We then analyse Dow Jones financial data over the period 1993-2012. Our theoretical approach is successful in describing the distributions and diffusion of the log price returns, and in delivering a power law for the volatility of log-returns for large time lags. However, the introduction of time dependence in $b(t)$, Equation (6.15), also yields a power law for the autocorrelation of log returns, which is typically described as an exponential decay [115, 116, 130]. Unlike an exponential decay, which is bounded as t tends to zero, the power law diverges for short times. For very small times, the simple model presented here may break down and $b(t)$ might no longer scale inversely with time.

Indeed some might be surprised that this model fits as well as it does over the entire time period of our data, given the limited number of parameters involved. Further generalisations to include, for example, skewness in the data might be considered for future work.

We finally present an initial application of the model to mean square displacements in soft disk simulations. We find the distributions of transverse displacements to be well-described by the same functional form as for log-returns, scaling superdiffusively up until the onset of normal diffusion and Gaussian distribution, in agreement with our analysis in Chapter 3. We once again find volatility clustering and long-range memory in the model, this time for the average transverse displacement. From here, the next challenge is to analyse the diffusion of the displacements in terms of functional forms for D_1 and D_2 , in order to solve the Fokker-Planck equation and extract an exponent for the scaling of the autocorrelation at long times.

Chapter 7

Outlook

Each chapter of this thesis has concluded with sections summarising our main findings, and suggesting future work regarding the methods and results presented in that chapter. We have extensively investigated the dynamics, fluctuations and rheology in the soft disk model for 2D foams, within the general theoretical framework of foams as a complex system. In so doing, we have successfully quantified new ways of linking the macroscopic, non-linear rheology of foams, well known from experiment, to the microscopic interactions at the bubble scale.

In this chapter, we shall give a general overview of potential future work, building on the advances presented in this thesis. We consider three general areas, which we feel are opportune for further investigation. In Section 7.1, we discuss an emergent property of foam flow which has yet to be well characterised: the swirling, vortex-like motion of bubbles at low strain rate. In Section 7.2, we consider the extension of the soft disk model to a soft sphere model, in three dimensions. Finally, in Section 7.3, we discuss the extension of the soft disk simulations to model the rheology of foams containing fibres, used in industrial applications such as the manufacture of paper.

7.1 Vorticity in the soft disk model

In considering foams as complex systems, as introduced in Section 1.5, we have discussed their emergent behaviour; that is, the non-linear properties of foams that are not simply inherent in, or derivable from, the individual bubble-bubble interactions. Instead, this emergent behaviour is observed at different hierarchical levels, due to some complex, collective aggregation or organisation of these interactions. Throughout this thesis we have focused on two hierarchies: the microscopic bubble scale, and the macroscopic rheological response. Examples of macroscopic emergent behaviour we have seen include the non-linear, Herschel-Bulkley-like scaling of the shear stress that arises despite only simple, linear local interactions (see Chapters 2 and 3), and long memory scaling of the volatility in stress fluctuations, over timescales much greater than the timescales associated with viscous and elastic interactions in the model at the bubble scale (see Chapter 5).

These are not the only hierarchies one may consider. An intermediate hierarchy, between that of the microscopic scale bubble interactions and that of the macroscopic scale rheology, is that of the swirling, non-affine, vortex-like motion of the bubbles at low strain rate, seen in Figure 7.1. These vortices emerge and dissipate continuously as the foam is sheared. This rotational flow, typically featuring radii of rotation much larger than a bubble diameter, is yet another example of emergent behaviour in the soft disk model.

By developing a quantitative description of the vortex motion in the soft disk model, one could then investigate the properties of these vortices. A good initial approach could be to relate foam flow to more general liquid flow. In fluid mechanics, the *vorticity* is a pseudovector field, $\vec{\omega}$, that describes local rotational flow. It is calculated by the curl of the fluid's velocity field \vec{v}

$$\vec{\omega} = \vec{\nabla} \times \vec{v}, \quad (7.1)$$

where $\vec{\nabla}$ is the del operator [18]. Similar to fluids, in principle one can calculate the vorticity pseudovector field for soft disk model simulations as

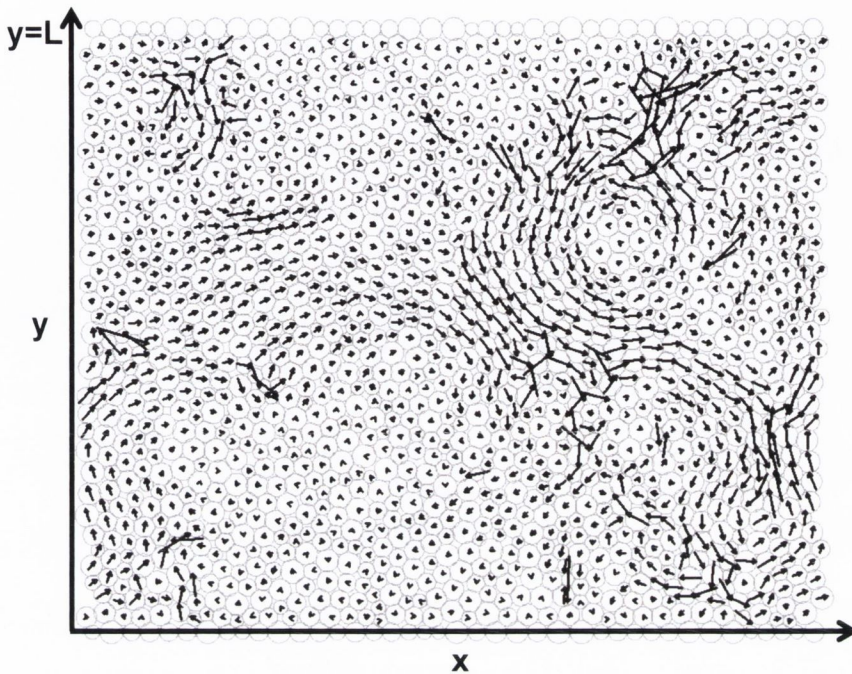


Figure 7.1: **Vortices in soft disk model flow.** Visualisation of a soft disk model simulation, with $De = 3.79 \times 10^{-5}$ and $\phi = 0.95$. The arrows show the instantaneous non-affine velocity vectors of the bubbles, that is their velocities minus the steady-state mean flow $\langle \mathbf{v}(y) \rangle$. Regions of rotational flow, or vortices, form and dissipate continuously throughout shear.

a function of time, from the velocity fields such as the example plotted in Figure 7.1.

With a qualitative measure of the vortices, it would be possible to address a range of questions. For instance, what are the distributions of their radii and angular velocities? Over what timescale do they typically form and disperse? Do their presence, size and shape depend on channel dimensions, polydispersity, packing fraction and strain rate? Ultimately, the aim would be to link properties of the vortices to fluctuations and non-linearity in the macroscopic rheology.

7.2 Towards a soft sphere model

As introduced in Section 1.2.3, 2D foams were initially introduced as a model system for numerical and theoretical studies of foams, as they present simpler systems to treat mathematically and computationally. Expansion of simulations and theory to 3D, however, remains principle goal of foams, colloids and granular media research.

In recent years, extensive work has been done on packing of disordered spheres in 3D, close to the jamming transition [17, 143, 144]. Models, such as the granocentric model [143], have been proposed to explain the distributions of contacts in such packings, and spatial correlations such as an analogy to the Aboav-Weaire law [13] in 3D (i.e. cells with many neighbours tend to be surrounded by cells with few neighbours, and *vice versa*). These simulations have been quasistatic, where the positions of the spheres have been determined by energy minimisation using conjugate gradient descent.

Advances in computing power, and the addition of parallel processing, have been such that we believe it is now feasible to overcome challenges which have previously made dynamic simulations in 3D impractical. Indeed, recently, Seth *et al.* presented results using a dynamic simulation of soft spheres [145], the first study of its kind.

With regard to the simulation of foams, there are two main challenges when it comes to extending the soft disk model to 3D. The first is connected with the nature of the interaction forces between interacting circular or spherical particles, as calculated by Lacasse *et al.* for emulsions [59], introduced in Section 1.3.2. In 2D, and as implemented in our simulations, the repulsion between interacting bubbles is well approximated by a harmonic interaction, for small compressions. However, in 3D, Lacasse *et al.* found that the repulsive force exerted by droplet i on droplet j depends non-trivially on the number of neighbours a droplet i has. One could assume, for the sake of simplification, that interactions could be modelled independent of contact number, as Seth *et al.* did [145]. However, an investigation of the effect of this simplification, still outstanding, would be interesting, as a complement to the work of Lacasse *et al.*

The second challenge in implementing a 3D foam simulation is technical, related to the increased computational intensiveness. Adding another dimension necessitates a large increase in the number of particles in the system, in order to investigate the bulk properties of that system away from the boundaries. For instance, if we wished to consider an equivalent 3D system to our 2D systems presented in Chapter 2, the number of particles N would increase by as much as a factor of 30. Furthermore, the average contact number of a sphere in 3D increases to 14, from 6 for disks in 2D [34]. As only overlapping particles interact, the average number of calculations per simulation timestep is directly proportional to the average number of contacts in the system. From the above, we can estimate that for equivalently large 3D systems, the computational intensiveness increases by approximately two orders of magnitude. Computational resources and methods, however, have now advanced to the point where this is no longer an insurmountable increase.

Consider Durian's original simulations, performed in 1995 [51]. These simulations were carried out, initially, for ~ 40 bubbles in 2D. In 2008, Langlois *et al.* presented results for system sizes of 1500 bubbles [52]. Following Moore's Law [146], which states that computer power increases by a factor of 2 every 1.5 years, today our brute-force computing power is 64 times that of Durian's in 1995, and 8 times that of Langlois' in 2008. An order of magnitude increase in capability has already been achieved through advances in processor technology alone.

Furthermore, what is achievable in simulation has been greatly enhanced by the advent of readily accessible parallel processing, as discussed in Appendix A. Using our CUDA implementation of the soft disk model code, we have achieved an order of magnitude increase in simulation speeds for a system size of 1500 bubbles in 2D, compared to serial code. The increase over serial implementation due to parallelisation becomes relatively larger as system size increases, lending itself well to the demands of 3D simulation.

We have seen a rich landscape of complex behaviour emerge from our simple 2D model. While it is straightforward to extend Newtonian interactions from 2D to 3D, non-linear emergent behaviour is not so easily translated. Extension of the soft disk model to 3D may generate new emergent behaviour

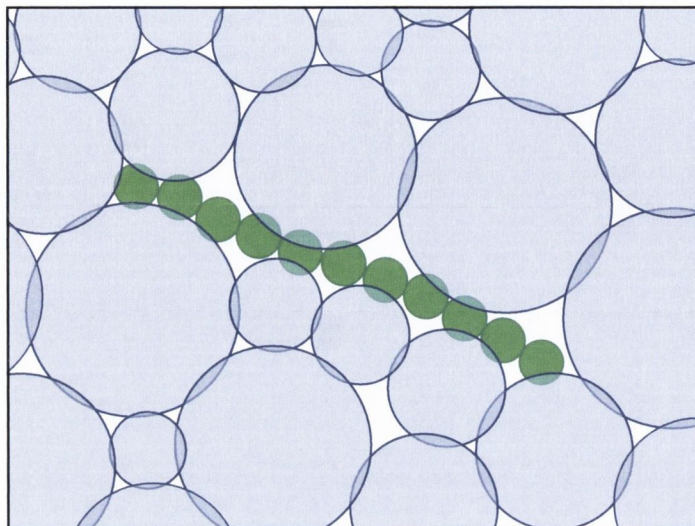


Figure 7.2: **Schematic illustration of a hypothetical model for fibres in foam.** The large blue disks represent bubbles, as simulated in our model. The smaller green disks are joined together sequentially by a Lennard-Jones-like attraction, representing a fibre. This fibre interacts via elastic and viscous forces with the bubbles and other fibres.

unseen in 2D, potentially granting yet further insight into the microscopic origins of the macroscopic rheology of foams.

7.3 The rheology of foams containing fibres

Foams containing fibres in suspension are used in the manufacture of paper [147]. Typically, paper is produced using aqueous solutions of fibres, extruded into sheets, drained and dried. The quality of the paper produced is determined, in part, by the spacial distribution of these fibres. A uniform distribution, with minimal clumping, produces higher quality paper. These fibres can be added instead to foams. It has been found that the bubbles in the foam act as spacers between the fibres, reducing clumping, and producing a more uniform distribution and thus better paper than the aqueous solutions.

As an industrial fabrication process, there is naturally a large interest in optimising this procedure. Currently, this optimisation is based on purely

empirical results. Open questions exist, such as how the distribution/dispersity of the fibres throughout the foam depends on packing fraction, strain rate during processing, and the ratio of the fibre lengths to the bubble sizes. Further questions include the effect of the stiffness of the fibres on their interaction with the foam, whether the suspensions feature shear-induced anisotropy or diffusion of the fibres and their alignments in the foam, and the effect of the fibres on the Herschel-Bulkley exponent and yield stress of the foam.

All of these questions have important practical ramifications and can, in principle, be investigated by modified soft disk model simulations. The fibres could hypothetically be modelled as chains of very small disks, added to a regular implementation of the soft disk model, see Figure 7.2. These disks are held together, sequentially, by the addition of a relatively strong attractive Lennard-Jones-like potential between neighbouring disks in a chain. These chains would then be free to move throughout the simulated foam, subject to elastic and viscous interactions with the bubbles and other fibres.

Such an implementation would be the first simulation model for what would constitute a new branch of foam physics, concerning the effect that the inclusion of fibres and amorphous polymers has on the properties of liquid foam.

Appendix A

Parallel Processing Using CUDA

Even during my four years of postgraduate studies, I have noticed a marked increase in what is achievable solely due to increases in technological capacity and computing power. We have been extremely fortunate to have access to the Lonsdale supercomputer cluster in the Trinity Centre for High Performance Computing, which has facilitated the computational hours (and storage space!) necessary for many of the results presented in this thesis.

Initially, all of the computations performed using the soft disk model used serial C code, making use of the Verlet algorithm (see Appendix C). My much-abused laptop proved insufficient to perform large scale calculations, so these were run on the Lonsdale cluster, in 4-day windows. Most of the results for $\phi = 0.95$, the first packing fraction we studied, were produced from consecutive 96 hour simulations. The longest simulation run, for the second-lowest strain rate we present first in Chapter 2, took approximately two and a half months, which was necessary to reach the steady state for such a low strain rate.

In conjunction with Steve Hardiman of the Foams and Complex Systems group, with whom I shared a mutual interest in parallel programming, we decided to attempt to implement a CUDA version of the soft disk model code. CUDA, which stands for Compute Unified Device Architecture, is an

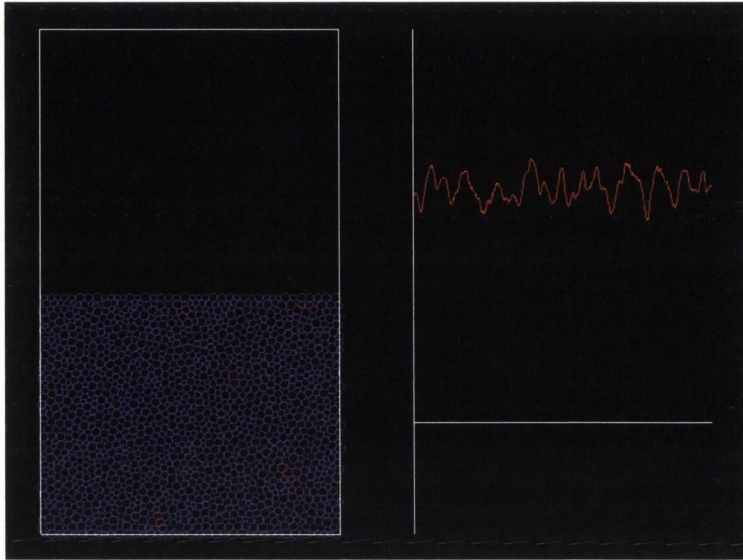


Figure A.1: **Real-time CUDA soft disk model simulation of linear shear.** The disks are coloured by their elastic energies; blue for low elastic energy, red for high. On the right, the stress is plotted as a function of strain in real time.

initiative by computer graphics card manufacturer NVIDIA designed to allow parallel processing and high performance computing without the need for the formidable computer architecture usually required.

Every modern computer comes equipped with a graphics card - a piece of hardware specifically designed to render 3D graphics. These cards can have hundreds or even thousands of “cores” - small computer processors in their own right, complete with their own virtual memory. These processors are optimised for linear algebra, and are not normally accessible by the user or the operating system. On CUDA-compatible cards, NVIDIA’s compiler *nvcc* allows modified C programs to make use of these cores with specific code syntax. More information on CUDA programming can be found on NVIDIA’s excellent website [148].

We have successfully implemented a parallelised version of the soft disk code, using CUDA-enabled C code. Below, we provide a commented example of one of the functions used in the CUDA version of our model, *cuda_upper_wall_data*. This function calculates the forces acting on the mov-

ing boundary. We distinguish between the **Host** (the central processor of the computer that the main{ } routine is executed on) and the **Device** (the CUDA enabled graphics card to which the parallel processes are sent).

```
//The function call cuda_upper_wall_data, from the
main{ } routine in the CUDA C code. The device_
variables are arrays defined on the Device.
These arrays are updated by copying from the
Host to the Device using the routine
cudaMemcpyHostToDevice.

cuda_upper_wall_data(device_forces, device_forcesv,
device_blockupforce, device_blockUPPERxforcev,
device_blockUPPERxforcee);

//The function definition cuda_upper_wall_data, from
the CUDA code kernel. From this point, we are
working on the Device, hence the arrays no
longer being distinguished as device_.
BLOCKSPERGRID and THREADSPERBLOCK are two key
parameters for parellisation. They determine how
the workload is split between CUDA cores, with
BLOCKSPERGRID groups of cores each executing
THREADSPERBLOCK threads. Optimum choices of
BLOCKSPERGRID and THREADSPERBLOCK are set by the
Device hardware. The function calls a kernel
function upper_wall_data_kernel, with the
argument <<< >>> providing instructions for the
distribution of the parallel threads.

void cuda_upper_wall_data(force *forces, force *
forcesv, float *blockupforce, float *
blockxforcev, float *blockxforcee)
{
```



```
    upper_wall_data_kernel <<< BLOCKSPERGRID,
        THREADSPERBLOCK >>> (forces, forcesv,
        blockupforce, blockxforcev, blockxforcee
        );

}

//The kernel function definition. This function is
run BLOCKSPERGRID*THREADSPERBLOCK times,
simultaneously. Each array element j,
corresponding to a different disk in the
simulation, is uniquely identified by its thread
and block number.

__global__ void upper_wall_data_kernel(force *forces,
    force *forcesv, float *blockupforce, float *
    blockxforcev, float *blockxforcee)
{
    int j = threadIdx.x + blockDim.x*blockIdx.x +
        1;

//The __shared__ variables are shared between all
threads and blocks.
    __shared__ float s_forcesz[THREADSPERBLOCK];
    __shared__ float s_forcesvx[THREADSPERBLOCK];
    __shared__ float s_forcesx[THREADSPERBLOCK];

//Calculating the forces on the upper wall. Many of
the threads for this particular function will
return zero, but if j is in the wall it will
return a value.
    if(j>=NBUBBLES+NWALL/2+1 && j<=NBUBBLES+NWALL
        ) {
```

```
        s_forcesz[threadIdx.x] = forces[j].z;
        s_forcesvx[threadIdx.x] = forcesv[j].
            x;
        s_forcesx[threadIdx.x] = forces[j].x
            - forcesv[j].x;
    } else {
        s_forcesz[threadIdx.x] = 0.0;
        s_forcesvx[threadIdx.x] = 0.0;
        s_forcesx[threadIdx.x] = 0.0;
    }

//The __syncthreads() command tells the process to
stop and wait for all threads to complete, at
this point.

    __syncthreads();

    int t;

//An efficient routine for summing all elements of
the shared arrays into the first element of the
array, over all threads on one block.

    for (t=blockDim.x/2; t>0; t/=2) {
        if (threadIdx.x < t) {
            s_forcesz[threadIdx.x] +=
                s_forcesz[t+threadIdx.x
                    ];
            s_forcesvx[threadIdx.x] +=
                s_forcesvx[t+threadIdx.x
                    ];
```

```
                s_forcesx[threadIdx.x] +=
                    s_forcesx[t+threadIdx.x
                    ];
            }
            __syncthreads();
        }

//Finally, we sum over all blocks and return the
//value of the forces on the wall. These values
//are returned to the Device array.
        if (threadIdx.x == 0) {
            blockupforce[blockIdx.x] += s_forcesz
                [0];
            blockxforcev[blockIdx.x] +=
                s_forcesvx[0];
            blockxforcee[blockIdx.x] += s_forcesx
                [0];
        }

        return;
    }

//In order for the main{} routine to access the
//Device arrays, we must call
//cudaMemcpyDeviceToHost in main{} to copy the
//memory to the Host.

ret = cudaMemcpy(blockupforce, device_blockupforce,
    BLOCKSPERGRID*sizeof(float),
    cudaMemcpyDeviceToHost);
if(ret != cudaSuccess) printf("Cuda_memory_copy_back_
    error\n");
```

The successful parallelisation of our simulation has two main benefits. Firstly, and most importantly, for a system size of 1500 disks, it increases the speed of the calculations by a factor of 10 or more. For larger systems, the relative increase in speed increased, as parallelisation lends itself well to increased system size. Using the CUDA code, a system of 12000 disks can be simulated at the same rate as a 1500 disk system using the serial code.

Secondly, the speed increase afforded by the CUDA code enables real-time visual output for the soft disk model simulation. A screenshot of this is shown in Figure A.1. This output shows the packing as it is sheared, and can, for instance, colour disks based upon their stress values or elastic energies. We can also plot, for instance, the shear stress as the system is strained.

Appendix B

Effective Packing Fraction

The packing fraction in the soft disk model is defined by Equation (2.6), that is

$$\phi = \frac{1}{A} \sum_i^N (d_i/2)^2 \pi, \quad (\text{B.1})$$

where N is the number of disks, d_i is the diameter of disk i , and A is the area of confinement. For consistency, both throughout this thesis and for the purposes of comparisons with the works of others using the soft disk model, we use this definition exclusively for all results. However, we note that this definition yields a value for ϕ which is not directly equivalent to the packing fraction calculated in experiment.

Why is this so? Consider the definition above. It is possible, given that disks are permitted to overlap, that the sum of the areas of the disks exceeds the value of A , the confining area. This would yield a value of $\phi > 1.0$, which is not possible for physical systems. This is due to the fact that the area within an overlap is double-counted, in the above definition.

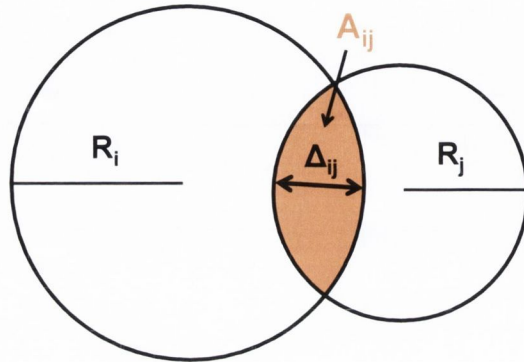


Figure B.1: **A schematic illustration of overlapping disks of different radii.** The radial overlap Δ_{ij} , shown, is given by Equation (2.3). Equation (B.3) describes the area of the shaded region, A_{ij} .

This discrepancy becomes relatively larger as packing fraction increases, due to increased overlaps. We can see this by defining an *average radial overlap*, $\langle \Delta \rangle$, as

$$\langle \Delta \rangle = \frac{1}{T} \sum_t \left[\frac{1}{C(t)} \sum_{j=i}^N \sum_{i=1}^N \Delta_{ij}(t) \right] \quad (\text{B.2})$$

where Δ_{ij} is the radial overlap between disks i and j as defined in Equation (2.3) and depicted in Figure B.1, $C(t)$ is the total number of contacts at time t , and T is the time window in the steady-state flow that the average radial overlap is calculated over. Figure B.2 plots $\langle \Delta \rangle$ as a function of strain rate and packing fraction, showing the average radial overlap to increase both with increasing strain rate, and increasing packing fraction.

In order to relate the simulation packing fraction to an equivalent experimental packing fraction, one could look at the average number of neighbours a disk has as a function of packing fraction, see Figure B.3. In the dry limit, the average contact number of a 2D foam $\langle z \rangle = 6$. For the soft disk model, this limit is not reached until $\phi \approx 1.3$ [144].

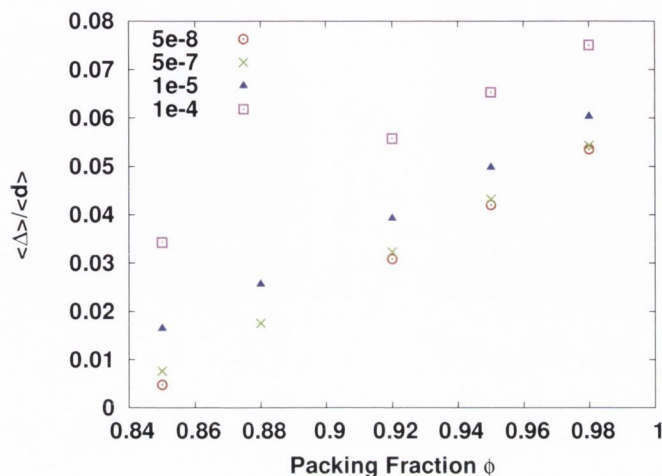


Figure B.2: **The variation of average overlap with strain rate and packing fraction.** Average radial overlap $\langle \Delta \rangle$, normalised by the average disk diameter $\langle d \rangle$, versus packing fraction ϕ . Data shown for Deborah numbers: $De = 5 \times 10^{-8}$, \circ ; $De = 5 \times 10^{-7}$, \times ; $De = 1 \times 10^{-5}$, \blacktriangle ; and $De = 1 \times 10^{-4}$, \square . The average overlap is seen to increase both with Deborah number, and with packing fraction.

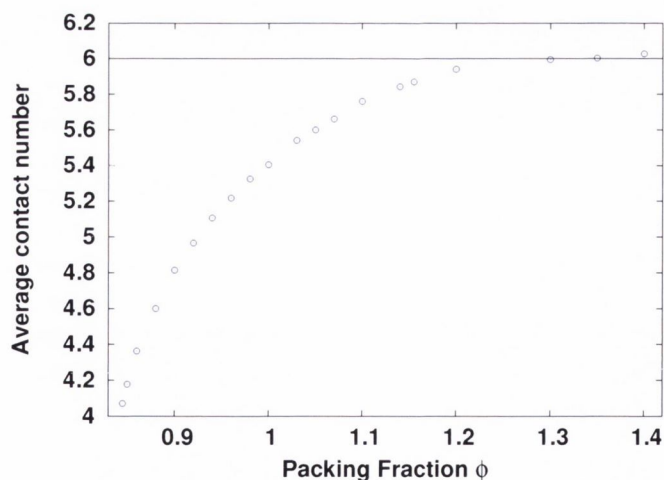


Figure B.3: **Average contact number versus packing fraction.** Data courtesy of C. O'Donovan, from [144]. In the dry limit, the average contact number $\langle z \rangle = 6$. This limit is not reached until packing fraction $\phi = 1.30$, for the soft disk model definition of packing fraction.

In principle, another approach is to correct for the double-counting of the overlaps computationally by explicitly calculating the excess areas. The area of the overlap, A_{ij} , between two disks, of radii R_i and R_j , whose centres are separated by a distance d (see Figure B.1), is given by [149]:

$$A_{ij} = R_i^2 \sin^{-1} \left(\frac{a}{2R_i} \right) - \sqrt{s_i(s_i - a)(s_i - R_i)^2} \\ + R_j^2 \sin^{-1} \left(\frac{a}{2R_j} \right) - \sqrt{s_j(s_j - a)(s_j - R_j)^2} \quad (\text{B.3})$$

with

$$s_i = \frac{a + 2R_i}{2} \quad s_j = \frac{a + 2R_j}{2} \quad (\text{B.4})$$

and

$$a = \frac{1}{d} \sqrt{(-d + R_i + R_j)(d - R_i + R_j)(d + R_i - R_j)(d + R_i + R_j)}. \quad (\text{B.5})$$

Simple!

We now define an *effective packing fraction*, ϕ^* , as

$$\phi^* = \phi - \frac{1}{AT} \sum_t \frac{1}{C(t)} \sum_{j=i}^N \sum_i^N A_{ij}(t). \quad (\text{B.6})$$

This expression is somewhat unwieldy, but conceptually simple: the effective packing fraction is total area of the disks minus the time-averaged sum of the double-counted overlaps, divided by the confining area A . We neglect contributions from three-bubble intersections, i.e. areas that are triple-counted, which are assumed to be small. This seems likely, as from Figure B.2 we see that the radial overlap for two bubbles in contact is of the order of only a few percent of a bubble diameter. The effective packing fraction is plotted versus packing fraction in Figure B.4.

We see that as ϕ increases, ϕ^* deviates from ϕ more widely, as expected. In the limit $\phi \rightarrow \infty$, the effective packing fraction $\phi^* \rightarrow 1$. This arises from

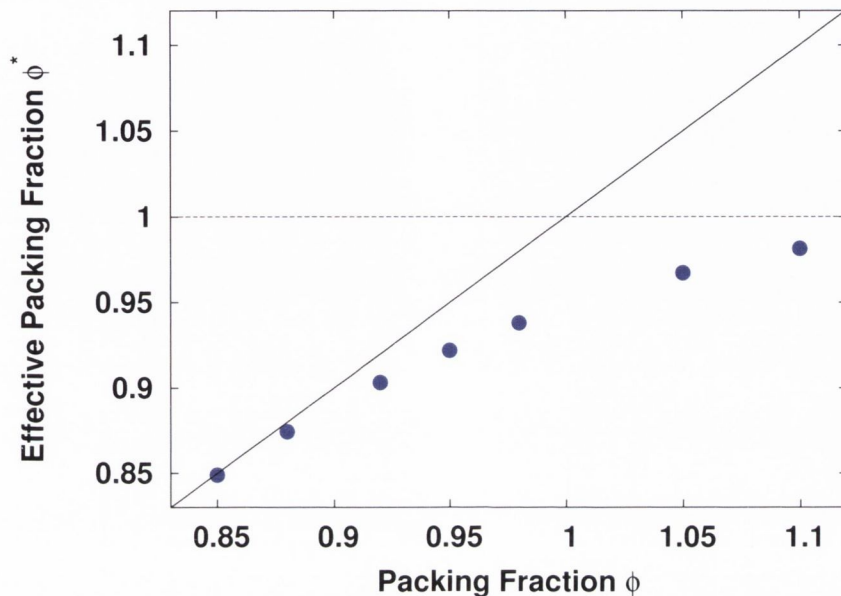


Figure B.4: **Effective packing fraction.** As packing fraction increases, the relative error between the defined packing fraction (shown by the solid black line of slope 1) and effective packing fraction increases. The effective packing fraction tends towards a value of $\phi^* = 1$, illustrated by the horizontal dashed line. Note that at $\phi_c \approx 0.84$, random close packing, the disks are just touching and the overlaps, on average, equal zero. Thus, here, $\phi = \phi^* = \phi_c$.

the definition of ϕ^* : it is not possible for the sum of the areas of the disks confined in an area A , minus the sum of the overlaps between those disks, to exceed A . At $\phi_c \approx 0.84$, random close packing, the disks are just touching and the overlaps, on average, equal zero. Thus, here, $\phi = \phi^* = \phi_c$.

Taking this correction into account, the highest packing fraction we present in this thesis, $\phi = 0.98$, has an effective packing fraction of approximately $\phi^* = 0.94$, which (unlike 0.98) is still well within the wet limit for 2D foams.

We note, however, unlike the packing fraction ϕ , which is well-defined as a constant for a given system configuration, ϕ^* contains time dependent terms which must be time-averaged, and is therefore poorly defined over short times.

Appendix C

Verlet Integration

Verlet integration is a numerical method used to integrate Newton's equation of motion [150]. Our implementation of the soft disk model uses second-order Verlet integration to update the positions $\mathbf{x}(t)$ and velocities $\mathbf{v}(t)$ of bubbles at each simulation timestep, as follows.

Let us denote the position and velocity at timestep n as x_n and v_n respectively. The acceleration a_n is given by the second derivative of the position with respect to time,

$$a_n = \frac{d^2 x_n}{dt^2}. \quad (\text{C.1})$$

The Verlet algorithm uses the central difference approximation applied to this second derivative

$$\begin{aligned} a_n &\approx \frac{\frac{x_{n+1} - x_n}{\Delta t} - \frac{x_n - x_{n-1}}{\Delta t}}{\Delta t} \\ &= \frac{x_{n+1} - 2x_n + x_{n-1}}{\Delta t^2}. \end{aligned} \quad (\text{C.2})$$

Thus the updated position x_{n+1} is given by

$$x_{n+1} = 2x_n - x_{n-1} + a_n \Delta t^2. \quad (\text{C.3})$$

Here, Δt is the simulation timestep, and a_n is calculated from the forces acting on the bubble at time n , F_n , via Newton's second law $F_n = ma_n$. The velocity v_n at each step n is given by

$$v_n = \frac{x_{n+1} - x_{n-1}}{2\Delta t}. \quad (\text{C.4})$$

For the second order Verlet algorithm, one needs two prior positions, x_n and x_{n-1} , to calculate the updated position x_{n+1} . For this reason, the **first** integration step must be performed using the simple Euler method, where (for initial conditions x_1, v_1)

$$\begin{aligned} x_2 &= x_1 + v_1 \Delta t \\ v_2 &= v_1 + a_1 \Delta t, \end{aligned} \quad (\text{C.5})$$

with a_1 determined by the initial forces, again via Newton's second law.

Appendix D

Time Resolutions and Limits of the Soft Disk Model

In this appendix we discuss briefly the computational considerations necessary to ensure that our system correctly captures the motion of the disks under shear. We also examine the effect on the model at very high strain rates, where the model “breaks down”.

D.1 Choosing an appropriate time resolution

As mentioned in Section 2.1.3, it is important, when realising a simulation, to ensure that the rate at which the calculations are performed is sufficient to capture the behaviour of the system. That is, if the shortest timescale in the simulation (e.g. the fastest oscillation in the system) is, say, one second, positions and velocities should be updated much more frequently than every second in order to fully resolve the motion.

In the soft disk model, we use the Verlet algorithm (Appendix C). This assumes, over some simulation timestep, τ_s , that each disk’s motion is well approximated by linear motion. The first check we impose, when running a simulation, is that the overlap between the disks never becomes too large

Deborah number	$1/\dot{\gamma}$	τ_s
$De < 0.015$	$> 66.67\tau_v$	$0.0027\tau_v$
$0.015 < De < 0.2$	$> 5\tau_v$	$0.000225\tau_v$
$0.2 < De < 0.5$	$> 2\tau_v$	$0.000021\tau_v$

Table D.1: Simulation time resolutions, compared to the characteristic time of deformation, as a function of Deborah number range.

(\sim the average disk radius). Consider the case where τ_s is chosen to be too large, such that a disk can sometimes travel distances larger than a radius in τ_s . In this situation, using the Verlet algorithm, it is possible for disks to pass through one another entirely! This is allowed by the parameterisation of the model (because τ_s was chosen to be too large), but it does not capture the behaviour of the physical system we are trying to model.

For increasingly high Deborah number simulations, where $De = \dot{\gamma}c_d/\kappa$ from Equation (2.9), the characteristic timescale of deformation $1/\dot{\gamma}$ decreases. This necessitates a reduction of τ_s for high Deborah number. Table D.1 lists the simulation timesteps we use, and the characteristic timescales of deformation, as functions of the Deborah number range presented in this thesis. The timescales are expressed in terms of the viscous timescale, $\tau_v = c_d/\kappa$ (Equation (2.8)).

D.2 Model behaviour at very high strain rate

In this thesis, we present results over a large range of strain rates, up to the limit $De < 0.5$. At very high strain rates, voids begin to appear in the foam, see Figure D.1, and the model is no longer suited to describing the flow of foams observed in experiment. This is a known limitation of the soft disk model: it is ascribed to the simplification of the model that non-overlapping disks do not experience viscous interactions [90]. Essentially, with only repulsive forces, at very high strain rates there are no attractive forces present to pull these voids closed. In a real foam, at this strain rate

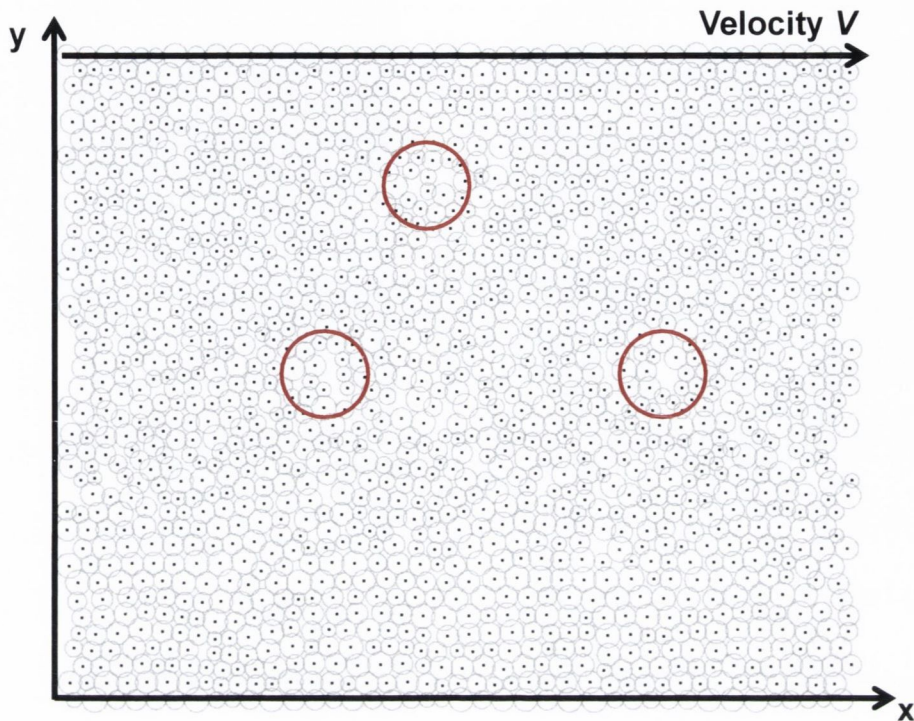


Figure D.1: **Voids in the soft disk model.** A visualisation of a soft disk model simulation for $De = 0.756$. The black dots show the bubble centre positions. At such very high strain rates, voids appear in the foam, some of which are highlighted by the red circles. At this point, the model is no longer a good representation of a flowing foam.

the bubbles would deform and elongate [21], which is not accounted for by the soft disk model. Above $De = 0.5$, we find the soft disk model to enter into a new regime that does not seem to have an equivalence in foams.

Appendix E

Long Memory Processes

In this Appendix, we define some of the mathematical terms we use in the discussion of long-range correlations throughout the thesis, and introduce the Hurst exponent as a quantitative measure of long memory in a timeseries.

E.1 Autocorrelation

In simple terms, the autocorrelation function measures the similarity of a time-dependent signal with itself some time later. It is a widely used mathematical tool to identify repeating patterns and persistent (or anti-persistent) correlations within a timeseries. Typically referred to as simply “the autocorrelation function”, the *normalised autocorrelation function* $A(\tau)$ for some time dependent process $x(t)$, over some *time lag* τ , is defined as

$$A(\tau) = \frac{\langle (x(t) - \mu)(x(t + \tau) - \mu) \rangle}{\Sigma^2}, \quad (\text{E.1})$$

with the mean $\mu = \langle x(t) \rangle$ and variance $\Sigma^2 = \langle (x(t) - \mu)^2 \rangle$. We use angled braces $\langle \rangle$ to denote a time average. For ergodic systems, this is interchangeable with an ensemble average for long times [99]. $A(\tau)$ is defined such that when $A = 1$, the signal is said to be perfectly correlated, when $A = -1$ perfectly anticorrelated, and $A = 0$ statistically uncorrelated.

The normalised autocorrelation assumes that $x(t)$ is *covariance stationary*. In simple terms, this is an assumption that μ and σ are independent of time for $x(t)$. In the systems studied in this thesis (mean-subtracted stress fluctuations, log-price returns and average transverse displacements), $\mu \approx 0$, and σ is constant. A more in-depth discussion of stationarity can be found in [99], but is not necessary for our analysis presented and thus omitted here.

E.2 Volatility clustering and long memory

Volatility clustering is a property of timeseries data, which was described by Mandelbrot succinctly as “large changes tend to follow large changes, and small changes tend to follow small changes” [151]. Such a property is visually distinctive, with fluctuations observed to cluster into slowly varying envelopes.

Volatility clustering is a characteristic property of so-called *long memory processes*. Simply speaking, a timeseries exhibits long memory if values from the distant past have a significant effect on the present. In a long memory process, the autocorrelation function $A(\tau)$ is found to vary as

$$A(\tau) \sim \tau^{-\beta} \quad \text{for } \tau \rightarrow \infty, \quad 0 < \beta < 1, \quad (\text{E.2})$$

where τ is the time lag. This power law scaling can imply correlations that persist well past the timescales of individual actions within a complex system. In the case of financial systems, for instance, and minute-by-minute price data whose correlations decay exponentially in under a minute, the volatility (or magnitude) of the prices have been found to show correlations lasting days or even months [108, 116].

The exact causes of long memory are not understood and its origin is the topic of much debate in the literature. It has been postulated that heterogeneity in timescales in a system could be one such origin. Granger [125] suggested that the aggregation of timeseries with different persistence levels (that is, with correlations decaying on different timescales) could result in long range memory. This hypothesis was supported by Anderson and

Bollerslev [152] as a possible explanation for volatility clustering in the aggregation of information flows, with the arrival rate of information governing the heterogeneity.

Another argument put forward is related to behaviour switching. It has been shown that the switching of traders in financial markets between two different strategies causes large aggregate fluctuations [153]. Liu *et al.* point out that the presence of switching alone can generate clustering, but is not sufficient for long-memory. They argue that if the time spent in each strategy is drawn from a heavy-tailed distribution, then long memory can arise [142].

Numerous further theories and variations on the above have been put forward. In the context of this thesis, we shall simply note two things. First, that long-range memory scaling arises non-trivially in systems with complex interactions between timescales, which prominently feature heavy-tailed distributions. Second, that these traits are inherent in soft disk model fluctuations, and that the soft disk model reproduces this scaling despite being unlike any other model currently under investigation in the econophysics literature.

E.3 The Hurst exponent

A quantitative measure of long range dependence can be obtained via the Hurst exponent. In a long memory process $x(t)$, the variance $\langle X(n)^2 \rangle$ of a running sum of n mean-subtracted values, $X(n)$, of such a process scales non-linearly as a function of n , via

$$\langle X(n)^2 \rangle \sim n^{2H}, \quad (\text{E.3})$$

where

$$X(n) = (x(1) - \mu) + (x(2) - \mu) + \dots + (x(n) - \mu). \quad (\text{E.4})$$

H is called the Hurst exponent. For long memory, or *persistent* processes, $0.5 < H < 1.0$. For normal diffusion, e.g. an uncorrelated random walk, $H = 0.5$. For *anti-persistent* processes, such as Kolmogorov's energy spectrum for

turbulence [99], $0.0 < H < 0.5$. The Hurst exponent of white noise is $H = 0$, and $H = 1$ for a linearly increasing function of time.

E.3.1 From Nile flooding to fractal geometry

The Hurst exponent was originally developed in hydrology, in order to predict the optimal dam size needed for the Nile river's volatile rain and drought conditions. An indication of just how vital the Nile was to the lives of those in the region, the Nile's annual water level has been measured at Roda Island, near Cairo, for over 5000 years. It has been recorded in writing for 1300 years between 622AD and 1922AD, just prior to the construction of the Nile dams [154], making it likely the earliest example of a statistical dataset. Remarkably, the first missing annual observation occurs in 1285. Hurst first calculated his exponent for the longest contiguous sample of data, spanning 662 years (622AD-1284AD), finding $N = 0.74$ [155].

Mandelbrot later generalised Hurst's analysis to a *generalised Hurst exponent*, as a measure for fractal geometry [156]. Hurst's initial approach to solving a practical problem of how high one must build a dam has since developed into its own field of mathematics.

E.3.2 Rescaled range (R/S) analysis

We estimate the Hurst exponent using a method known as the *rescaled range (R/S) analysis*, originally used by Hurst and still the conventional choice in the literature. The rescaled range $Q(n) = R(n)/S(n)$ can be viewed as a statistical measure of the variability of a timeseries x_i over some sample size n , as a function of n . It is given by the range $R(n)$ (that is, $R(n) = x_{\max} - x_{\min}$, over the sample size n), divided by the standard deviation of the sample $S(n)$. $Q(n)$ scales with n via the Hurst exponent,

$$Q(n) \sim n^H. \tag{E.5}$$

We outline the steps by which we implement this calculation as follows, in line with the method proposed by Weron [121]. Consider a timeseries x_1, x_2, \dots, x_N of N measured values. First, we calculate the sample mean

$$\mu = \frac{1}{N} \sum_{i=1}^N x_i. \quad (\text{E.6})$$

Next, we create a new mean adjusted sequence $y_i = x_i - \mu$. Then, we calculate the cumulative sum of n values of the series as a function of n :

$$z_n = \sum_{i=1}^n y_i. \quad (\text{E.7})$$

The range is the difference between the maximum and minimum values of the cumulative sum

$$R(n) = \max(z_1, z_2 \dots z_n) - \min(z_1, z_2 \dots z_n). \quad (\text{E.8})$$

The standard deviation series $S(n)$ is given by

$$S(n) = \sqrt{\frac{1}{n} \sum_{i=1}^n y_i^2} \quad (\text{E.9})$$

Finally, the rescaled range $Q(n)$ is given by

$$Q(n) = \frac{R(n)}{S(n)} \propto n^H \quad (\text{E.10})$$

and H can be obtained from linear regression fits to $\log Q$ vs $\log n$. Anis and Lloyd [157] and Peters [158] have shown that small corrections for finite sample size effects give a better estimate of the Hurst exponent. We implement their corrections, detailed fully in [121], in our estimation.

References

- [1] D. Rind, “Complexity and climate,” *Science*, vol. 284, no. 5411, pp. 105–107, 1999.
- [2] G. Nicolis and C. Nicolis, *Foundations of complex systems: emergence, information and prediction*. World Scientific Publishing Company, 2012.
- [3] P. Stevenson, *Foam engineering: fundamentals and applications*. Wiley.com, 2012.
- [4] J. Cilliers, “Foams, froth and flotation...or how bubbles buoy the world economy,” 2008. www.imperial.ac.uk/pls/portallive/docs/1/37065696.PDF.
- [5] Central Intelligence Agency, *CIA World Factbook*. 2013. <https://www.cia.gov/library/publications/the-world-factbook/>.
- [6] R. Steger, H. Dajani, K. Davidson, C. Garbowski, and P. Rios, “KPMG Global Semiconductor Survey,” 2013. <http://www.kpmg.com/US/en/IssuesAndInsights/ArticlesPublications/Documents/kpmg-global-semiconductor-survey-optimistic-2013.pdf>.
- [7] L. Bragg and J. F. Nye, “A dynamical model of a crystal structure,” *Proceedings of the Royal Society A: Mathematical, Physical and Engineering Sciences*, vol. 190, pp. 474–481, 1947.
- [8] L. Lerman, “Potential role of bubbles and droplets in primordial and planetary chemistry: exploration of the liquid-gas interface as a reaction zone for condensation process,” *Origins of Life and Evolution of Biospheres*, vol. 16, no. 3, pp. 201–202, 1986.

-
- [9] C. Darwin and W. F. Bynum, *The origin of species by means of natural selection: or, the preservation of favored races in the struggle for life*. 1859.
- [10] T. Aste and D. Weaire, *The pursuit of perfect packing*. Bristol and Philadelphia: Institute of Physics Publishing, 2000.
- [11] W. Thomson, “On the Division of Space with Minimum Partition Area,” *Philosophical Magazine*, vol. 24, p. 503, 1887.
- [12] D. Weaire, “Kelvin’s foam structure: a commentary,” *Philosophical Magazine Letters*, vol. 88, no. 2, pp. 91–102, 2008.
- [13] D. Weaire and S. Hutzler, *The physics of foams*. Oxford: Clarendon press, 1999.
- [14] R. J. Hunter, *Introduction to modern colloid science*, vol. 7. Oxford University Press Oxford, 1993.
- [15] D. Weaire, V. Langlois, M. Saadatfar, and S. Hutzler, “Foam as granular matter,” in *Granular and Complex Materials, World Scientific Lecture Notes in Complex Systems, volume 8* (D. M. T. A. T and T. A, eds.), (New Jersey), pp. 1–26, World Scientific Publishing, 2007.
- [16] J. Plateau, *Statique Expérimentale et Théorique des Liquides soumis aux seules Forces Moléculaires*. Paris: Gauthier-Villars, 1873.
- [17] C. S. O’Hern, L. E. Silbert, A. J. Liu, and S. R. Nagel, “Jamming at zero temperature and zero applied stress: The epitome of disorder,” *Physical Review E*, vol. 68, p. 011306, Jul 2003.
- [18] Landau and Lifschitz, *Fluid Mechanics*. Pergamon Press, 1987.
- [19] J. F. H. H. A. Barnes and K. Walters, *An introduction to rheology*. Amsterdam: Elsevier, 1989.
- [20] W. H. Herschel and R. Bulkley, “Konsistenzmessungen von gummi-benzollösungen,” *Kolloid-Zeitschrift*, vol. 39, no. 4, pp. 291–300, 1926.
- [21] N. D. Denkov, S. Tcholakova, K. Golemanov, K. P. Ananthapadmanabhan, and A. Lips, “The role of surfactant type and bubble surface mobility in foam rheology,” *Soft Matter*, vol. 5, pp. 3389–3408, 2009.

-
- [22] N. D. Denkov, S. Tcholakova, K. Golemanov, K. P. Ananthapadmanabhan, and A. Lips, “Viscous friction in foams and concentrated emulsions under steady shear,” *Physical Review Letters*, vol. 100, p. 138301, 2008.
- [23] J. Lauridsen, M. Twardos, and M. Dennin, “Shear-induced stress relaxation in a two-dimensional wet foam,” *Physical Review Letters*, vol. 89, p. 098303, 2002.
- [24] N. D. Denkov, V. Subramanian, D. Gurovich, and A. Lips, “Wall slip and viscous dissipation in sheared foams: Effect of surface mobility,” *Colloids Surf. A*, vol. 263, pp. 129–145, 2005.
- [25] C. Gilbreth, S. Sullivan, and M. Dennin, “Flow transitions in two-dimensional foams,” *Physical Review E*, vol. 74, p. 051406, 2006.
- [26] G. Katgert, M. E. Möbius, and M. van Hecke, “Rate dependence and role of disorder in linearly sheared two-dimensional foams,” *Physical Review Letters*, vol. 101, p. 058301, 2008.
- [27] H. Princen and A. Kiss, “Rheology of foams and highly concentrated emulsions IV: An experimental-study of the shear viscosity and yield stress of concentrated emulsions,” *Journal of Colloid and Interface Science*, vol. 128, no. 1, pp. 176–187, 1989.
- [28] S. A. Khan, C. A. Schnepper, and R. C. Armstrong, “Foam rheology: III. measurement of shear flow properties,” *Journal of Rheology*, vol. 32, pp. 69–92, 1988.
- [29] M. E. Möbius, G. Katgert, and M. van Hecke, “Relaxation and flow in linearly sheared two-dimensional foams,” *Europhysics Letters*, vol. 90, p. 44003, 2010.
- [30] R. Lespiat, S. Cohen-Addad, and R. Höhler, “Jamming and flow of random-close-packed spherical bubbles: an analogy with granular materials,” *Physical Review Letters*, vol. 106, no. 14, pp. 148302–148302, 2011.
- [31] J. Goyon, A. Colin, G. Ovarlez, A. Ajdari, and L. Bocquet, “Spatial cooperativity in soft glassy flows,” *Nature*, vol. 454, pp. 84–87, 2008.

-
- [32] P. Jop, Y. Forterre, and O. Pouliquen, “A constitutive law for dense granular flows,” *Nature*, vol. 441, no. 7094, pp. 727–730, 2006.
- [33] T. G. Mason, J. Bibette, and D. A. Weitz, “Yielding and flow of monodisperse emulsions,” *Journal of Colloid and Interface Science*, vol. 179, pp. 439–448, 1996.
- [34] A. M. Kraynik, “Foam flows,” *Annual Review of Fluid Mechanics*, vol. 20, pp. 325–357, 1988.
- [35] F. Bolton and D. Weaire, “Rigidity loss transition in a disordered 2D froth,” *Physical Review Letters*, vol. 65, p. 3449, 1990.
- [36] D. J. Durian, “Bubble-scale model of foam mechanics: Melting, nonlinear behavior, and avalanches,” *Physical Review E*, vol. 55, pp. 1739–1751, 1997.
- [37] A. Saint-Jalmes and D. Durian, “Vanishing elasticity for wet foams: Equivalence with emulsions and role of polydispersity,” *Journal of Rheology*, vol. 43, p. 1411, 1999.
- [38] S. Hutzler, D. Weaire, and F. Bolton, “The effects of Plateau borders in the two-dimensional soap froth, III. Further results,” *Philosophical Magazine B*, vol. 71, p. 277, 1995.
- [39] F. P. Bretherton, “The motion of long bubbles in tubes,” *Journal of Fluid Mechanics*, vol. 10, pp. 166–188, 1961.
- [40] A. Saugey, W. Drenckhan, and D. Weaire, “Wall slip of bubbles in foams,” *Phys. Fluids*, vol. 18, p. 053101, 2006.
- [41] M. Saadatfar, F. Garcia-Moreno, S. Hutzler, A. Sheppard, M. Knackstedt, J. Banhart, and D. Weaire, “Imaging of metallic foams using x-ray micro-ct,” *Colloids and Surfaces A: Physicochemical and Engineering Aspects*, vol. 344, no. 1-3, pp. 107 – 112, 2009.
- [42] J. Brujic, S. F. Edwards, I. Hopkinson, and H. A. Makse, “Measuring the distribution of interdroplet forces in a compressed emulsion system,” *Physica A: Statistical Mechanics and its Applications*, vol. 327, no. 3-4, pp. 201 – 212, 2003.

-
- [43] A. M. Kraynik, D. A. Reinelt, and F. van Swol, “Structure of random monodisperse foam,” *Physical Review E*, vol. 67, p. 031403, Mar. 2003.
- [44] R. J. Clancy, E. Janiaud, D. Weaire and S. Hutzler, “The response of 2d foams to continuous applied shear in a Couette rheometer,” *Eur. Phys. J. E*, vol. 21, pp. 123–132, 2006.
- [45] E. Janiaud, D. Weaire, and S. Hutzler, “A simple continuum model for the dynamics of a quasi-two dimensional foam,” *Colloids and Surfaces A: Physicochemical and Engineering Aspects*, vol. 309, pp. 125–131, 2007.
- [46] A. Kabla and G. Debrégeas, “Local stress relaxation and shear banding in dry foam under shear,” *Physical Review Letters*, vol. 90, p. 258303, 2003.
- [47] D. Weaire, S. Hutzler, V. J. Langlois, and R. J. Clancy, “Velocity dependence of shear localisation in a 2D foam,” *Philosophical Magazine Letters*, vol. 88, pp. 387–396, 2008.
- [48] G. Katgert, A. Latka, M. E. Möbius, and M. van Hecke, “Flow in linearly sheared two-dimensional foams: From bubble to bulk scale,” *Physical Review E*, vol. 79, p. 066318 (15 pages), 2009.
- [49] J. Lauridsen, G. Chanan, and M. Dennin, “Velocity profiles in slowly sheared bubble rafts,” *Physical Review Letters*, vol. 93, p. 018303, 2004.
- [50] Y. H. Wang, K. Krishan, and M. Dennin, “Impact of boundaries on velocity profiles in bubble rafts,” *Physical Review E*, vol. 73, p. 031401, 2006.
- [51] D. J. Durian, “Foam mechanics at the bubble scale,” *Physical Review Letters*, vol. 75, pp. 4780–4783, 1995.
- [52] V. J. Langlois, S. Hutzler, and D. Weaire, “Rheological properties of the soft disk model of 2D foams,” *Physical Review E*, vol. 78, p. 021401, 2008.
- [53] H. Princen, “Rheology of foams and highly concentrated emulsions I: Elastic properties and yield stress of a cylindrical model system,” *Journal of Colloid and Interface Science*, vol. 91, pp. 160–175, 1983.
- [54] H. Princen, “Rheology of foams and highly concentrated emulsions II: Experimental study of the yield stress and wall effects for concentrated oil-in-

- water emulsions,” *Journal of Colloid and Interface Science*, vol. 105, no. 1, pp. 150–171, 1985.
- [55] H. Princen and A. Kiss, “Rheology of foams and highly concentrated emulsions III: Static shear modulus,” *Journal of Colloid and Interface Science*, vol. 112, no. 2, pp. 427–437, 1986.
- [56] L. Schwartz and H. Princen, “A theory of extensional viscosity for flowing foams and concentrated emulsions,” *Journal of Colloid and Interface Science*, vol. 118, no. 1, pp. 201 – 211, 1987.
- [57] D. Weaire and N. Rivier, “Soap, cells and statistics: Random patterns in two dimensions,” *Contemp. Phys.*, vol. 25, p. 59, 1984.
- [58] D. Reinelt and A. Kraynik, “Viscous effects in the rheology of foams and concentrated emulsions,” *Journal of Colloid and Interface Science*, vol. 132, no. 2, pp. 491 – 503, 1989.
- [59] M. D. Lacasse, G. S. Grest, and D. Levine, “Deformation of small compressed droplets,” *Physical Review E*, vol. 54, no. 5, pp. 5436–5446, 1996.
- [60] K. Brakke, “<http://www.susqu.edu/brakke/evolver/evolver.html>.”
- [61] S. Tcholakova, N. D. Denkov, K. Golemanov, K. P. Ananthapadmanabhan, and A. Lips, “Theoretical model of viscous friction inside steadily sheared foams and concentrated emulsions,” *Physical Review E*, vol. 78, p. 011405, 2008.
- [62] Y. H. Wang, K. Krishan, and M. Dennin, “Bubble kinematics in a sheared foam,” *Physical Review E*, vol. 74, no. 4, p. 041405, 2006.
- [63] M. Dennin, “Statistics of bubble rearrangements in a slowly sheared two-dimensional foam,” *Physical Review E*, vol. 70, p. 041406, Oct 2004.
- [64] M. Lundberg, K. Krishan, N. Xu, C. S. O’Hern, and M. Dennin, “Comparison of low-amplitude oscillatory shear in experimental and computational studies of model foams,” *Physical Review E*, vol. 79, no. 4, p. 041405, 2009.
- [65] Y. H. Wang, K. Krishan, and M. Dennin, “Limits of the equivalence of time and ensemble averages in shear flows,” *Physical Review Letters*, vol. 98, no. 22, p. 220602, 2007.

-
- [66] C. Ancey, P. Coussot, and P. Evesque, “A theoretical framework for granular suspensions in a steady simple shear flow,” *Journal of Rheology*, vol. 43, p. 1673, 1999.
- [67] J. Duran, *Sands, powders, and grains: an introduction to the physics of granular media*. Springer New York, 2000.
- [68] D. Weaire, R. J. Clancy, and S. Hutzler, “A simple analytical theory of localisation in 2d foam rheology,” *Philosophical Magazine Letters*, vol. 89, pp. 294–299, 2009.
- [69] J. Barry, D. Weaire, and S. Hutzler, “Nonlocal effects in the continuum theory of shear localisation in 2d foams,” *Philosophical Magazine Letters*, vol. 91, no. 6, pp. 432–440, 2011.
- [70] D. Weaire and J. P. Kermode, “Computer simulation of a two-dimensional soap froth. I. Method and motivation,” *Philosophical Magazine B*, vol. 48, pp. 245–259, 1983.
- [71] D. Weaire and J. P. Kermode, “Computer simulation of a two-dimensional soap froth. II. Analysis of results,” *Philosophical Magazine B*, vol. 50, pp. 379–395, 1984.
- [72] D. Weaire and J. P. Kermode, “The evolution of the structure of a two-dimensional soap froth,” *Philosophical Magazine B*, vol. 47, pp. L29–L31, 1983.
- [73] F. Bolton, “Software PLAT: A computer code for simulating two-dimensional liquid foams,” <http://www.tcd.ie/Physics/Foams/plat.php>, 1996.
- [74] F. Bolton and D. Weaire, “The effects of Plateau borders in the two-dimensional soap froth. I. Decoration lemma and diffusion theorem,” *Philosophical Magazine B*, vol. 63, pp. 795–809, 1991.
- [75] F. Bolton and D. Weaire, “The effects of Plateau borders in the two-dimensional soap froth. II. General simulation and analysis of rigidity loss transition,” *Philosophical Magazine B*, vol. 65, pp. 473–487, 1992.
- [76] N. Xu and C. S. O’Hern, “Measurements of the yield stress in frictionless granular systems,” *Physical Review E*, vol. 73, p. 061303, 2006.

-
- [77] P. Olsson and S. Teitel, “Critical scaling of shear viscosity at the jamming transition,” *Physical Review Letters*, vol. 99, no. 17, p. 178001, 2007.
- [78] T. Hatano, “Growing length and time scales in a suspension of athermal particles,” *Physical Review E*, vol. 79, p. 050301, 2009.
- [79] B. P. Tighe, E. Woldhuis, J. J. C. Remmers, W. van Saarloos, and M. van Hecke, “Model for the scaling of stresses and fluctuations in flows near jamming,” *Physical Review Letters*, vol. 105, no. 8, p. 088303, 2010.
- [80] K. N. Nordstrom, E. Verneuil, P. E. Arratia, A. Basu, Z. Zhang, A. G. Yodh, J. P. Gollub, and D. J. Durian, “Microfluidic rheology of soft colloids above and below jamming,” *Physical Review Letters*, vol. 105, p. 175701, 2010.
- [81] I. K. Ono, S. Tewari, S. A. Langer, and A. J. Liu, “Velocity fluctuations in a steadily sheared model foam,” *Physical Review E*, vol. 67, no. 6, p. 061503, 2003.
- [82] M. B. Sexton, M. E. Möbius, and S. Hutzler, “Bubble dynamics and rheology in sheared two-dimensional foams,” *Soft Matter*, vol. 7, pp. 11252–11258, 2011.
- [83] L. Pietronero, “Complexity ideas from condensed matter and statistical physics,” *Europhysics news*, vol. 39/6, pp. 26–29, 2008.
- [84] P. W. Anderson, “More is different,” *Science*, vol. 177, no. 4047, pp. 393–396, 1972.
- [85] J. Von Neumann, *The computer and the brain*. Yale University Press, 1958.
- [86] D. Weaire and S. Hutzler, “Foam as a complex system,” *Journal of Physics: Condensed Matter*, vol. 21, p. 4227, 2009.
- [87] A. Randall, *Risk and precaution*. Cambridge University Press, 2011.
- [88] S. V. Buldyrev, R. Parshani, G. Paul, H. E. Stanley, and S. Havlin, “Catastrophic cascade of failures in interdependent networks,” *Nature*, vol. 464, no. 7291, pp. 1025–1028, 2010.
- [89] A. van der Net, G. W. Delaney, W. Drenckhan, D. Weaire, and S. Hutzler, “Crystalline arrangements of microbubbles in monodisperse foams,” *Colloids*

- and Surfaces A: Physicochemical and Engineering Aspects*, vol. 309, pp. 117–124, 2007.
- [90] S. Tewari, D. Schiemann, D. Durian, C. Knobler, S. Langer, and A. Liu, “Statistics of shear-induced rearrangements in a two-dimensional model foam,” *Physical Review E*, vol. 60, pp. 4385–4396, 1999.
- [91] K. Pye and H. Tsoar, *Aeolian sand and sand dunes*. Springer, 2009.
- [92] P.-E. Peyneau and J.-N. Roux, “Frictionless bead packs have macroscopic friction, but no dilatancy,” *Physical Review E*, vol. 78, p. 011307, 2008.
- [93] Private communication with M.E. Möbius.
- [94] T. Witten and P. Pincus, *Structured Fluids: Polymers, Colloids, Surfactants*. Oxford University Press, 2004.
- [95] L. Bocquet, A. Colin, and A. Ajdari, “Kinetic theory of plastic flow in soft glassy materials,” *Physical Review Letters*, vol. 103, p. 036001, 2009.
- [96] J. Goyon, A. Colin, and L. Bocquet, “How does a soft glassy material flow: finite size effects, non local rheology, and flow cooperativity,” *Soft Matter*, vol. 6, pp. 2668–2678, 2010.
- [97] A. D. Gopal and D. J. Durian, “Shear-induced ”melting” of an aqueous foam,” *Journal of Colloid and Interface Science*, vol. 213, no. 1, pp. 169–178, 1999.
- [98] D. Ben-Avraham and S. Havlin, *Diffusion and reactions in fractals and disordered systems*. Cambridge University Press, 2000.
- [99] J. Beran, *Statistics for long-memory processes*, vol. 61. CRC Press, 1994.
- [100] A. W. Lau, B. D. Hoffman, A. Davies, J. C. Crocker, and T. C. Lubensky, “Microrheology, stress fluctuations, and active behavior of living cells,” *Physical Review Letters*, vol. 91, no. 19, p. 198101, 2003.
- [101] R. Besseling, E. R. Weeks, A. B. Schofield, and W. C. K. Poon, “Three-dimensional imaging of colloidal glasses under steady shear,” *Physical Review Letters*, vol. 99, no. 2, p. 028301, 2007.

-
- [102] F. Varnik and O. Henrich, “Yield stress discontinuity in a simple glass,” *Physical Review B*, vol. 73, no. 17, p. 174209, 2006.
- [103] K. Martens, L. Bocquet, and J. Barrat, “Connecting diffusion and dynamical heterogeneities in actively deformed amorphous systems,” *Physical Review Letters*, vol. 106, p. 156001, 2011.
- [104] F. A. Lindemann, “Ueber die berechnung molekularer eigenfrequenzen,” *Phys. Z.*, vol. 11, pp. 609–612, 1910.
- [105] G. Katgert, B. Tighe, M. E. Möbius, and M. van Hecke, “Couette flow of two-dimensional foams,” *Europhysics Letters*, vol. 90, p. 54002, 2010.
- [106] A. Lees and S. Edwards, “The computer study of transport processes under extreme conditions,” *Journal of Physics C: Solid State Physics*, vol. 5, no. 15, p. 1921, 1972.
- [107] A. J. Meagher, M. Mukherjee, D. Weaire, S. Hutzler, J. Banhart, and F. Garcia-Moreno, “Analysis of the internal structure of monodisperse liquid foams by x-ray tomography,” *Soft Matter*, vol. 7, pp. 9881–9885, 2011.
- [108] F. Lillo and J. D. Farmer, “The long memory of the efficient market,” *Studies in Nonlinear Dynamics and Econometrics*, vol. 8, pp. 1558–3708, 2004.
- [109] P. Richmond, J. Mimkes, and S. Hutzler, *Econophysics and Physical Economics*. Oxford University Press, 2013.
- [110] S. J. Hardiman, P. Richmond, and S. Hutzler, “Long-range correlations in an online betting exchange for a football tournament,” *New Journal of Physics*, vol. 12, no. 10, p. 105001, 2010.
- [111] Y. Y. Kagan and D. D. Jackson, “Long-term earthquake clustering,” *Geophysical Journal International*, vol. 104, no. 1, pp. 117–133, 1991.
- [112] T. Karagiannis, M. Molle, and M. Faloutsos, “Long-range dependence ten years of internet traffic modeling,” *Internet Computing, IEEE*, vol. 8, no. 5, pp. 57–64, 2004.
- [113] T. Preis and H. Stanley, “Switching phenomena in a system with no switches,” *Journal of Statistical Physics*, vol. 138, pp. 431–446, 2010.

- [114] I. N. Lobato and C. Velasco, “Long memory in stock-market trading volume,” *Journal of Business & Economic Statistics*, vol. 18, no. 4, pp. 410–427, 2000.
- [115] Y. Liu, P. Gopikrishnan, Cizeau, Meyer, Peng, and H. E. Stanley, “Statistical properties of the volatility of price fluctuations,” *Physical Review E*, vol. 60, pp. 1390–1400, 1999.
- [116] R. N. Mantegna and H. E. Stanley, *Introduction to econophysics: correlations and complexity in finance*. Cambridge University Press, 1999.
- [117] K. Park, G. Kim, and M. Crovella, “On the relationship between file sizes, transport protocols, and self-similar network traffic,” in *Network Protocols, 1996. Proceedings., 1996 International Conference on*, pp. 171–180, IEEE, 1996.
- [118] B. G. Malkiel and E. F. Fama, “Efficient capital markets: A review of theory and empirical work*,” *The Journal of Finance*, vol. 25, no. 2, pp. 383–417, 1970.
- [119] Tick Data, *Tickwrite Database*. 2012. <http://www.tickdata.com>.
- [120] J. Alvarez-Ramirez, J. Alvarez, E. Rodriguez, and G. Fernandez-Anaya, “Time-varying Hurst exponent for us stock markets,” *Physica A: Statistical Mechanics and its Applications*, vol. 387, no. 24, pp. 6159–6169, 2008.
- [121] R. Weron, “Estimating long-range dependence: finite sample properties and confidence intervals,” *Physica A: Statistical Mechanics and its Applications*, vol. 312, no. 1, pp. 285–299, 2002.
- [122] P. Grau-Carles, “Empirical evidence of long-range correlations in stock returns,” *Physica A: Statistical Mechanics and its Applications*, vol. 287, no. 3, pp. 396–404, 2000.
- [123] R. Cont, “Long range dependence in financial markets,” in *Fractals in Engineering*, pp. 159–179, Springer, 2005.
- [124] D. M. Guillaume, M. M. Dacorogna, R. R. Davé, U. A. Müller, R. B. Olsen, and O. V. Pictet, “From the bird’s eye to the microscope: A survey of new stylized facts of the intra-daily foreign exchange markets,” *Finance and Stochastics*, vol. 1, no. 2, pp. 95–129, 1997.

-
- [125] C. W. Granger, “Long memory relationships and the aggregation of dynamic models,” *Journal of Econometrics*, vol. 14, no. 2, pp. 227–238, 1980.
- [126] J. J. Stickel and R. L. Powell, “Fluid mechanics and rheology of dense suspensions,” *Annual Review of Fluid Mechanics*, vol. 37, pp. 129–149, 2005.
- [127] D. E. Wolf, *Modelling and Computer Simulation of Granular Media*. Springer Berlin Heidelberg, 1996.
- [128] W.-F. Chen and E. Mizuno, *Nonlinear analysis in soil mechanics: theory and implementation*. Elsevier Amsterdam, 1990.
- [129] X. Gabaix, P. Gopikrishnan, V. Plerou, and H. E. Stanley, “Understanding the cubic and half-cubic laws of financial fluctuations,” *Physica A: Statistical Mechanics and its Applications*, vol. 324, no. 1, pp. 1–5, 2003.
- [130] J. L. McCauley, *Dynamics of markets: econophysics and finance*, vol. 31. Cambridge University Press Cambridge, 2004.
- [131] M. M. Dacorogna, U. A. Müller, R. J. Nagler, R. B. Olsen, and O. V. Pictet, “A geographical model for the daily and weekly seasonal volatility in the foreign exchange market,” *Journal of International Money and Finance*, vol. 12, no. 4, pp. 413–438, 1993.
- [132] H. Roman, M. Porto, and C. Dose, “Skewness, long-time memory, and non-stationarity: Application to leverage effect in financial time series,” *Europhysics Letters*, vol. 84, no. 2, p. 28001, 2008.
- [133] J. Shen and B. Zheng, “On return-volatility correlation in financial dynamics,” *Europhysics Letters*, vol. 88, no. 2, p. 28003, 2009.
- [134] R. N. Mantegna and H. E. Stanley, “Scaling behaviour in the dynamics of an economic index,” *Nature*, vol. 376, no. 6535, pp. 46–49, 1995.
- [135] P. Gopikrishnan, V. Plerou, L. A. N. Amaral, M. Meyer, and H. E. Stanley, “Scaling of the distribution of fluctuations of financial market indices,” *Physical Review E*, vol. 60, no. 5, p. 5305, 1999.
- [136] S. M. Queirós, L. G. Moyano, J. de Souza, and C. Tsallis, “A nonextensive approach to the dynamics of financial observables,” *The European Physical Journal B*, vol. 55, no. 2, pp. 161–167, 2007.

- [137] L. Borland, “Microscopic dynamics of the nonlinear fokker-planck equation: A phenomenological model,” *Physical Review E*, vol. 57, pp. 6634–6642, Jun 1998.
- [138] A. Plastino and A. Plastino, “Non-extensive statistical mechanics and generalized Fokker-Planck equation,” *Physica A: Statistical Mechanics and its Applications*, vol. 222, no. 14, pp. 347 – 354, 1995.
- [139] M. Lax, W. Cai, and M. Xu, *Random Processes in Physics and Finance*. USA: Oxford University Press, 2006.
- [140] M. Gell-Mann and C. Tsallis, *Nonextensive Entropy: Interdisciplinary Applications: Interdisciplinary Applications*. Oxford University Press, USA, 2004.
- [141] Bloomberg. <http://www.bloomberg.com/quote/INDU:IND>.
- [142] M. Liu, “Modeling long memory in stock market volatility,” *Journal of Econometrics*, vol. 99, no. 1, pp. 139–171, 2000.
- [143] M. Clusel, E. I. Corwin, A. O. Siemens, and J. Bruijicacute, “A granocentricmodel for random packing of jammed emulsions,” *Nature*, vol. 460, no. 7255, pp. 611–615, 2009.
- [144] C. O’Donovan and M. Möbius, “Spatial correlations in polydisperse, frictionless, two-dimensional packings,” *Physical Review E*, vol. 84, no. 2, p. 020302, 2011.
- [145] J. R. Seth, L. Mohan, C. Locatelli-Champagne, M. Cloitre, and R. T. Bonnecaze, “A micromechanical model to predict the flow of soft particle glasses,” *Nature Materials*, vol. 10, no. 11, pp. 838–843, 2011.
- [146] G. E. Moore *et al.*, “Cramming more components onto integrated circuits,” 1965.
- [147] J. P. Hanson, “Whats going on in non-wovens,” *Pulp & Paper*, p. 97 102, 1977.
- [148] NVIDIA Corporation, *Online CUDA resource*. http://www.nvidia.com/object/cuda_home_new.html.

-
- [149] B. Breech, "Intersection of two circles of different radii." <http://www.eecis.udel.edu/~breech/contest/problems/intersection-2circles.pdf>.
- [150] L. Verlet, "Computer "experiments" on classical fluids. I. Thermodynamical properties of Lennard-Jones molecules," *Physical Review*, vol. 159, no. 1, p. 98, 1967.
- [151] B. B. Mandelbrot, *The variation of certain speculative prices*. Springer, 1997.
- [152] T. G. Andersen and T. Bollerslev, "Heterogeneous information arrivals and return volatility dynamics: Uncovering the long-run in high frequency returns," *The Journal of Finance*, vol. 52, no. 3, pp. 975–1005, 1997.
- [153] A. Kirman, "Ants, rationality, and recruitment," *The Quarterly Journal of Economics*, vol. 108, no. 1, pp. 137–156, 1993.
- [154] O. Toussoun, *Mémoire sur l'histoire du Nil*. Inst. for the History of Arabic-Islamic Science at the Johann Wolfgang Goethe Univ., 1925.
- [155] H. E. Hurst, "Long-term storage capacity of reservoirs," *Transactions of the American Society of Civil Engineers*, vol. 116, pp. 770–808, 1951.
- [156] B. B. Mandelbrot and J. R. Wallis, "Noah, Joseph, and operational hydrology," *Water Resources Research*, vol. 4, no. 5, pp. 909–918, 1968.
- [157] A. Annis and E. Lloyd, "The expected value of the adjusted rescaled Hurst range of independent normal summands," *Biometrika*, vol. 63, no. 1, pp. 111–116, 1976.
- [158] E. E. Peters *et al.*, *Fractal market analysis: applying chaos theory to investment and economics*, vol. 24. Wiley New York, 1994.

- [125] C. W. Granger, “Long memory relationships and the aggregation of dynamic models,” *Journal of Econometrics*, vol. 14, no. 2, pp. 227–238, 1980.
- [126] J. J. Stickel and R. L. Powell, “Fluid mechanics and rheology of dense suspensions,” *Annual Review of Fluid Mechanics*, vol. 37, pp. 129–149, 2005.
- [127] D. E. Wolf, *Modelling and Computer Simulation of Granular Media*. Springer Berlin Heidelberg, 1996.
- [128] W.-F. Chen and E. Mizuno, *Nonlinear analysis in soil mechanics: theory and implementation*. Elsevier Amsterdam, 1990.
- [129] X. Gabaix, P. Gopikrishnan, V. Plerou, and H. E. Stanley, “Understanding the cubic and half-cubic laws of financial fluctuations,” *Physica A: Statistical Mechanics and its Applications*, vol. 324, no. 1, pp. 1–5, 2003.
- [130] J. L. McCauley, *Dynamics of markets: econophysics and finance*, vol. 31. Cambridge University Press Cambridge, 2004.
- [131] M. M. Dacorogna, U. A. Müller, R. J. Nagler, R. B. Olsen, and O. V. Pictet, “A geographical model for the daily and weekly seasonal volatility in the foreign exchange market,” *Journal of International Money and Finance*, vol. 12, no. 4, pp. 413–438, 1993.
- [132] H. Roman, M. Porto, and C. Dose, “Skewness, long-time memory, and non-stationarity: Application to leverage effect in financial time series,” *Europhysics Letters*, vol. 84, no. 2, p. 28001, 2008.
- [133] J. Shen and B. Zheng, “On return-volatility correlation in financial dynamics,” *Europhysics Letters*, vol. 88, no. 2, p. 28003, 2009.
- [134] R. N. Mantegna and H. E. Stanley, “Scaling behaviour in the dynamics of an economic index,” *Nature*, vol. 376, no. 6535, pp. 46–49, 1995.
- [135] P. Gopikrishnan, V. Plerou, L. A. N. Amaral, M. Meyer, and H. E. Stanley, “Scaling of the distribution of fluctuations of financial market indices,” *Physical Review E*, vol. 60, no. 5, p. 5305, 1999.
- [136] S. M. Queirós, L. G. Moyano, J. de Souza, and C. Tsallis, “A nonextensive approach to the dynamics of financial observables,” *The European Physical Journal B*, vol. 55, no. 2, pp. 161–167, 2007.

- [137] L. Borland, “Microscopic dynamics of the nonlinear fokker-planck equation: A phenomenological model,” *Physical Review E*, vol. 57, pp. 6634–6642, Jun 1998.
- [138] A. Plastino and A. Plastino, “Non-extensive statistical mechanics and generalized Fokker-Planck equation,” *Physica A: Statistical Mechanics and its Applications*, vol. 222, no. 14, pp. 347 – 354, 1995.
- [139] M. Lax, W. Cai, and M. Xu, *Random Processes in Physics and Finance*. USA: Oxford University Press, 2006.
- [140] M. Gell-Mann and C. Tsallis, *Nonextensive Entropy: Interdisciplinary Applications: Interdisciplinary Applications*. Oxford University Press, USA, 2004.
- [141] Bloomberg. <http://www.bloomberg.com/quote/INDU:IND>.
- [142] M. Liu, “Modeling long memory in stock market volatility,” *Journal of Econometrics*, vol. 99, no. 1, pp. 139–171, 2000.
- [143] M. Clusel, E. I. Corwin, A. O. Siemens, and J. Bruijicacute, “A granocentricmodel for random packing of jammed emulsions,” *Nature*, vol. 460, no. 7255, pp. 611–615, 2009.
- [144] C. O’Donovan and M. Möbius, “Spatial correlations in polydisperse, frictionless, two-dimensional packings,” *Physical Review E*, vol. 84, no. 2, p. 020302, 2011.
- [145] J. R. Seth, L. Mohan, C. Locatelli-Champagne, M. Cloitre, and R. T. Bonnecaze, “A micromechanical model to predict the flow of soft particle glasses,” *Nature Materials*, vol. 10, no. 11, pp. 838–843, 2011.
- [146] G. E. Moore *et al.*, “Cramming more components onto integrated circuits,” 1965.
- [147] J. P. Hanson, “Whats going on in non-wovens,” *Pulp & Paper*, p. 97 102, 1977.
- [148] NVIDIA Corporation, *Online CUDA resource*. http://www.nvidia.com/object/cuda_home_new.html.